2022

# Development of a Dual-Mode CMOS Microelectrode Array for the Simultaneous Study of Electrochemical and Electrophysiological Activities of the Brain

Geoffrey Mulberry
*University of Central Florida*

# DEVELOPMENT OF A DUAL-MODE CMOS MICROELECTRODE ARRAY FOR THE SIMULTANEOUS STUDY OF ELECTROCHEMICAL AND ELECTROPHYSIOLOGICAL ACTIVITIES IN THE BRAIN

by

GEOFFREY MULBERRY
B.S. in Electrical Engineering, University of Central Florida, 2017
M.S. in Electrical Engineering, University of Central Florida, 2019

A dissertation submitted in partial fulfillment of the requirements
for the degree of Doctor of Philosophy
in the Department of Electrical and Computer Engineering
in the College of Engineering and Computer Science
at the University of Central Florida
Orlando, Florida

Summer Term
2022

Major Professor: Brian N. Kim

# ABSTRACT

Medical diagnostic devices are in high demand due to increasing cases of neurodegenerative diseases in the aging population and pandemic outbreaks in our increasingly connected global community. Devices capable of detecting the presence of a disease in its early stages can have dramatic impacts on how it can be treated or eliminated. High cost and limited accessibility to diagnostic tools are the main barriers preventing potential patients from receiving a timely disease diagnosis. This dissertation presents several devices that are aimed at providing higher quality medical diagnostics at a low cost. Brain function is commonly studied with systems detecting the action potentials that are formed when neurons fire. CMOS technology enables extremely high-density electrode arrays to be produced with integrated amplifiers for high-throughput action potential measurement systems while greatly reducing the cost per measurement compared to traditional tools. Recently, CMOS technology has also been used to develop high-throughput electrochemical measurement systems. While action potentials are important, communication between neurons occurs by the flow of neurotransmitters at the synapses, so measurement of action potentials alone is incapable of fully studying neurotransmission. In many neurodegenerative diseases the breakdown in neurotransmission begins well before the disease manifests itself. The development of a dual-mode CMOS device that is capable of simultaneous high-throughput measurement of both action potentials and neurotransmitter flow via an on-chip electrode array is presented in this dissertation. This dual-mode technology is useful to those studying the dynamic decay of the neurotransmission process seen in many neurodegenerative diseases using a low-cost CMOS chip. This dissertation also discusses the development of more traditional diagnostic devices relying on PCR, a method commonly used only in centralized

laboratories and not readily available at the point-of-care. These technologies will enable faster, cheaper, more accurate, and more accessible diagnostics to be performed closer to the patient.

For my parents.

# ACKNOWLEDGMENTS

Many incredible people helped support me to complete this work. I would like to briefly thank them for their aid: my advisor, Brian Kim, for his guidance throughout my graduate studies; Ray Lugo and Ricardo Zaurin for their recommendations; my colleagues, especially Kevin White, Danny Nichols, and Nick Ross for their camaraderie; medical students, Matthew Moench and Alex McClanahan, for their perspective from the medical field; my aunt Karen, uncle Mike, and cousin Genie for the inspiration to pursue higher education; and finally my parents, Brenda and Gerry, and sisters, Janet and Jenna, for the encouragement they have given throughout my life and education.

Finally, without funding from the National Science Foundation (NSF) under grant numbers #1745364 and #2133225, the United States Air Force Office of Scientific Research (AFOSR) under grant #FA9550-21-1-0117, and the National Institute of Allergy and Infectious Diseases (NIH/NIAID) under 1R21AI142330-01, this work would not have been possible.

# TABLE OF CONTENTS

# LIST OF FIGURES

# LIST OF TABLES

# CHAPTER 1: INTRODUCTION

The human body is ordinarily an extremely resilient mechanism, yet it is susceptible to myriad ailments and diseases. Of particular interest in research are neurodegenerative diseases and infectious diseases. Some examples of neurodegenerative diseases are Parkinson's Disease and Alzheimer's Disease, while some examples of infectious diseases are ZIKA, COVID-19, and HIV/AIDS. Developments in engineering have enabled the creation of tools to aid healthcare professionals and medical researchers to effectively diagnose as well as study the mechanisms of the human body and the diseases which impair it. The fields of engineering and medicine are closely intertwined, and medicine owes a great debt to engineering advancements. As an example, consider the explosion in understanding and technology originating from Watson and Crick's discovery of the structure of DNA that was published in 1953 [1]. This discovery inspired a large scientific interest in the study of DNA, because of the importance of the discovery, Watson and Crick were awarded the Nobel Prize in 1962 [2]. A technique was developed for producing copies of DNA called polymerase chain reaction (PCR) in 1986 [3]. The inventor, Mullis, was similarly awarded a Nobel Prize for his development of PCR [4]. Around the same time, a technique was developed for the automated sequencing the order of the order of DNA nucleobases that resulted in the first commercial machine capable of automatic DNA sequencing [5], [6]. The rapid pace of genetic technology was so great, that it even spread into popular culture, inspiring Crichton's Jurassic Park, where a fictional company uses PCR and genome sequencing technology to create clones of extinct dinosaurs from ancient DNA sources [7]. In reality, these new technologies caused rapid growth in science and allowed for the international effort known as the Human Genome Project to sequence the entire human genome, with initial results published in 2001 [8] and the final chromosome being completed in 2006 [9]. Further evolution building on this

genomic technology resulted in CRISPR [10], which can be used to individually edit particular sections of genetic code along DNA [11], enabling the genetic engineering that was only fiction two decades prior. The creation of CRISPR also earned a Nobel Prize for Charpentier and Doudna [12].

With the potential for such rapid growth of scientific understanding and new techniques for diagnostics and tools, this dissertation presents some of the devices developed throughout my graduate studies to enable future progress in these areas. This research focuses on two multidisciplinary areas both related to electronics and the field of medical diagnostics. The first is brain computer interfacing, or BCI, where a silicon chip containing on-chip electrode arrays is used to monitor signals from the brain with data being sent to a computer for analysis and study. The second is the area of medical diagnostics, based largely on PCR and devices to aid researchers in both performing PCR as well as in preparing samples so they are suitable for use with PCR. With the increasing burden of neurodegenerative diseases on our aging population and the potential for future viral pandemic outbreaks such as COVID-19, the need for powerful, effective research and diagnostic tools is stronger than ever [13], [14].

### 1.1 Neurodegenerative Diseases and Brain Computer Interfacing

The brain is the most complex organ in the body and is of particular interest since it is responsible for man's achievements over all other animals. The brain still outcompetes some of the most advanced computing technology that has been devised to date ($10^{18}$-$10^{22}$ FLOPS for the human brain vs. $10^{18}$ for current supercomputers) [15], [16]. Because of the complexities in its operation, the mechanisms that enable its function and ailments are relatively less well understood when compared to other human organs. This is due in large part to the lacking tools available to neuroscientists and other researchers for high throughput measurements of the brain. For a more complete understanding

of the brain, it is necessary to develop tools which can be used to study the brain in much more detail than the current state of the art, enabling researchers to make the next breakthrough discovery.

### 1.1.1 Neurotransmission

The active cell type in the brain is the neuron. Through complex interconnections and communication between the billons of neurons, cognitive function is enabled. Neurotransmission is the process by which neurons communicate with one another. Figure 1.1a demonstrates how neurotransmission typically works in a healthy brain. The area shown is known as a synapse, which is the area where two neurons meet, and is where communication occurs. The neuron on the left is known as the presynaptic neuron, since it is where the communication is originating from, while the neuron on the right is known as the postsynaptic neuron since it will be receiving the signals. In healthy neurotransmission, an action potential comes from the soma of the presynaptic neuron and travels along an axon until it reaches the end, where the vesicles are located. The vesicles contain neurotransmitters such as dopamine, serotonin, or glutamate. When stimulated, the vesicles release neurotransmitters in a process known as exocytosis. Receptors are located on a dendrite of the postsynaptic neuron, when they receive neurotransmitters from the presynaptic neuron's exocytosis, they can produce a signal that travels to the cell's soma. If there is sufficient stimulation, the postsynaptic neuron may produce its own action potentials to communicate with other downstream neurons. A common mechanism causing unhealthy neurotransmission is the buildup of plaque at the synapses (Figure 1.1b). When this buildup occurs, neurotransmitters can become blocked from reaching the receptors of the postsynaptic neuron, causing a breakdown in communication between neurons. This leads to many of the common neurodegenerative diseases as well as neuronal loss [17]–[21].

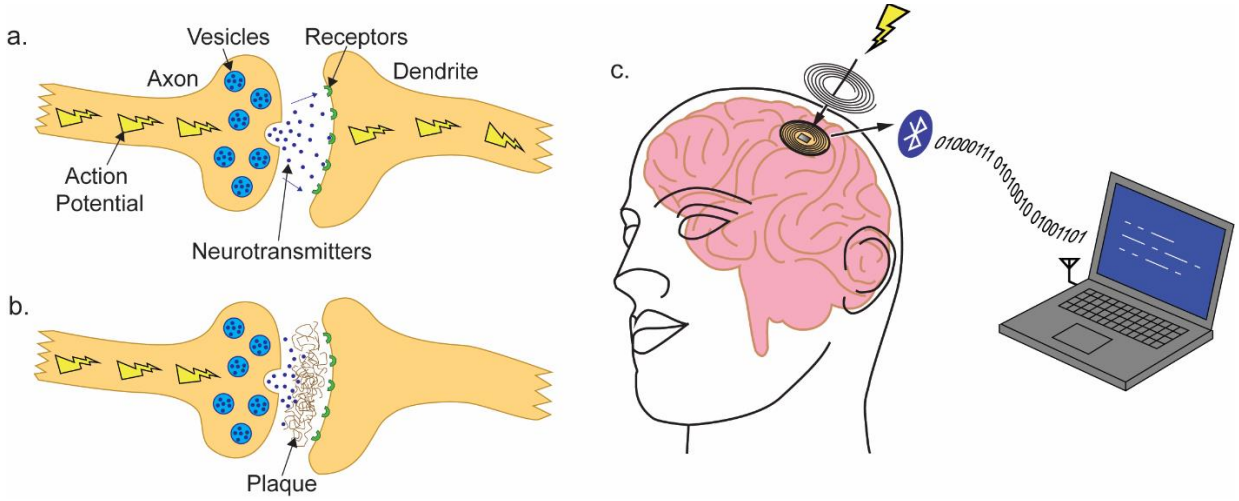


Figure 1.1. Neurotransmission and the BCI concept. (a.) Healthy neurotransmission: neurotransmitters from axon travel to receptors on dendrite and AP is produced. (b.) Unhealthy neurotransmission: plaque buildup blocks neurotransmitter flow; dendrite does not receive neurotransmitters. (c.) BCI concept: a CMOS chip placed in the brain measures neurotransmission and sends signals to computer for analysis.

### 1.1.2 BCI concept

The goal of BCI is ultimately to produce a device that can be implanted in a subject's brain allowing for the continuous monitoring of brain activity from a computer. This has practical applications in medicine, especially in enabling handicapped individuals to control devices such as artificial limbs or a computer when they cannot use traditional human interface devices like a keyboard and mouse. It could also be useful in monitoring a patient susceptible to neurodegenerative diseases. In Figure 1.1c an example of a BCI is presented. Using CMOS technology, high-performance and high electrode count multielectrode arrays with integrated amplifiers can be integrated onto a single compact chip that is implantable directly on the brain. Because of its small size and thin cross section, this implant could even be permanently installed below the skull. With additional technologies such as wireless power transmission and integrated wireless communication, a complete BCI could be produced that does not impose any inconvenience for the patient while enabling a continuous study of their brain function.

When examining the method of neurotransmission, there are two distinct modalities. The first are action potentials, that is, the volage spikes that travel along neurons. The second is the flow of neurotransmitters. Commonly used BCIs measure only action potentials, since they are voltage measurements for which amplifiers are heavily studied. However, because of the huge importance of neurotransmitters in the complete neurotransmission process, the neurotransmitter flow would ideally also be measured as well. This is especially true for medical purposes, where the monitoring of the decay of neurotransmission is desired. To perform this measurement a BCI chip must contain not only the common voltage amplifier, but also neurochemical amplifiers. The dual-mode CMOS device presented in Chapter 4 provides a new technology for neuroscientists to study the mechanisms of neuronal communication and degradation on a scale and density that has not been previously reported.

## 1.2 Medical Diagnostics for Infectious Diseases

With the prevalence of outbreaks of infectious diseases across the world such as Dengue virus, Zika virus, and SARS-CoV-2, comes the need for diagnostic procedures that are not only accurate, but are capable of determining the stage of infection in an acute-care setting. Quantitative polymerase chain reaction (qPCR) is such a method and is used to diagnose infectious diseases with a high degree of accuracy [22]. qPCR utilizes specially designed primers to amplify target viral nucleic acid sequences. This is especially helpful in acute-care diagnostic settings, as viral nucleic acid sequences are present in low levels in patient samples (such as blood). Unfortunately, qPCR is often not the first diagnostic technique used in an acute care setting due to its time consuming, labor-intensive sample preparation process and need for expensive equipment. The procedure must be carried out at a specialized laboratory, which may take days due to the transportation of the patient sample and the required skilled labor. Since the development of lab-on-a-chip systems, microfluidic systems, and point-of-care (POC) systems for diagnostics, there has been a significant effort to produce microfluidic devices that

can be used for medical diagnostics in acute-care settings [23]. Similarly, the development of 3D-printed, low-cost, portable qPCR and sample preparation devices may significantly increase accessibility to accurate infectious disease diagnosis, especially in areas of the world where current expensive qPCR equipment is not readily available [24].

### 1.2.1 Polymerase Chain Reaction

The polymerase chain reaction is a process that is used to produce copies of DNA. The process works by exploiting an enzyme that is responsible for the production of DNA copies called polymerase. A specific type of polymerase called *Taq* polymerase is stable at high temperatures that are used in PCR [25]. Figure 1.2 shows a simplified explanation of how the process of PCR functions. Several agents are required in PCR as shown in Figure 1.2a. The T-shaped objects are individual free nucleotides that will be assembled into DNA strands (Figure 1.2a1). The pink oval represents the *Taq* polymerase (Figure 1.2a2). Finally, the primers, which are used to establish the specific sequence to be amplified are presented in Figure 1.2a3. The PCR process starts with a single strand of double-stranded DNA (Figure 1.2b). When heat is applied to double-stranded DNA, Figure 1.2c, the strands separate into two complementary strands in a process known as denaturing. A typical temperature for the denaturing stage is 95 °C. Once the strands are separated, the temperature is lowered to approximately 60 °C and the primers are able to bind to the strands in a step known as annealing. On the top strand in Figure 1.2d, a primer is seen approaching a strand and the polymerase is also approaching. On the bottom strand, the extension process is in progress. In this step, the polymerase travels along the DNA strand starting at the primer and assembles the complementary side of the DNA strand using free nucleotides. When extension is complete on both strands, the result is two identical copies of the original DNA molecule (Figure 1.2e). By cycling the temperature between denaturing and annealing/extension temperatures the quantity of DNA copies increases twofold for each cycle. This

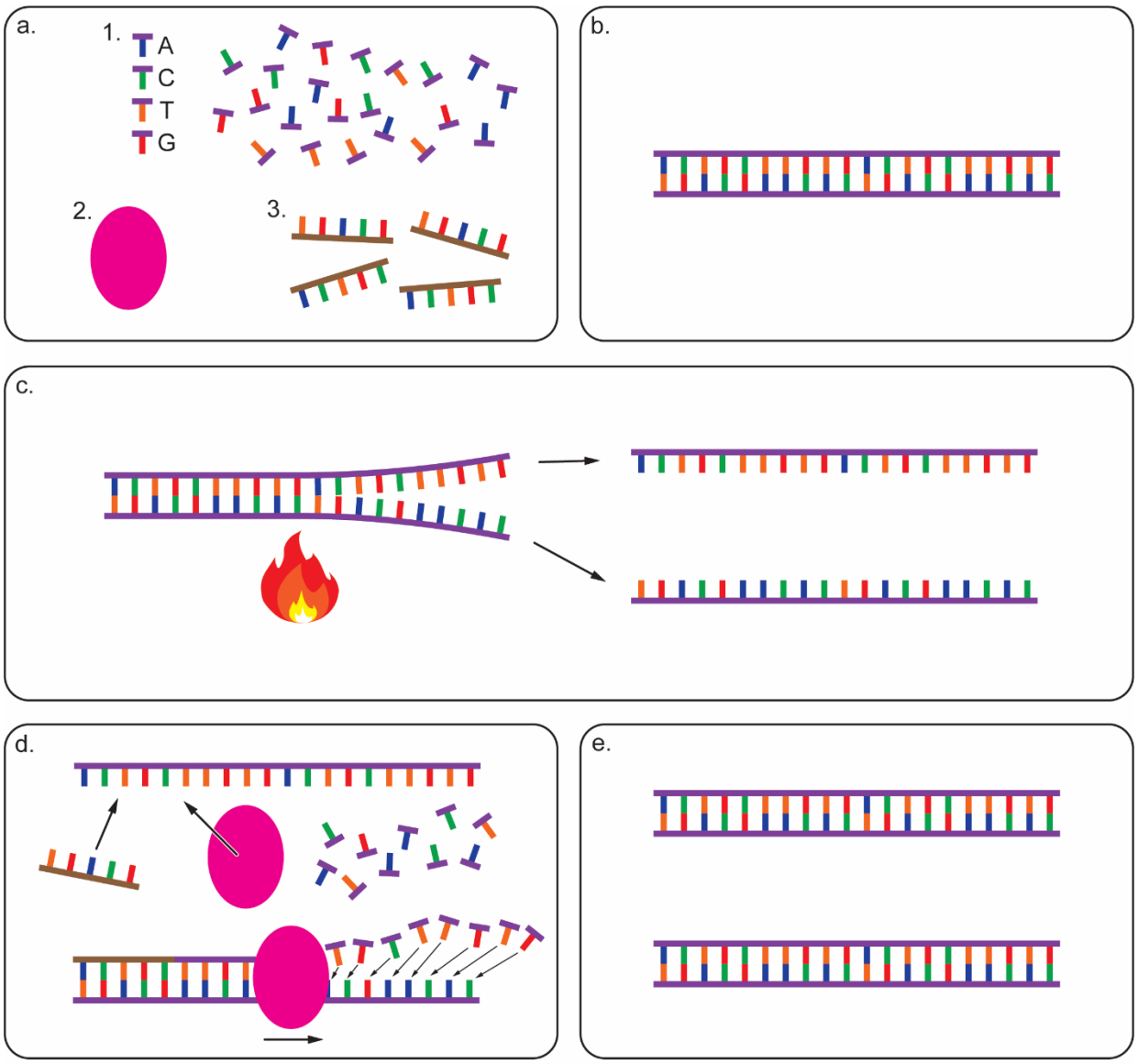


Figure 1.2. Details of the Polymerase Chain Reaction. (a.) Reagents needed for PCR. (b.) A strand of DNA. (c.) Denaturing: heat separates the DNA strands into two complementary single strands. (d.) Annealing and Extension: Primers bind to single strands; Polymerase extends primers creating new strands. (e.) Resulting two copies of double-stranded DNA.

process can theoretically extend for an arbitrary number of cycles and produce an unlimited number of DNA copies (hence the term chain reaction). In practical applications however, there is not an unlimited supply of primers and free nucleotides, so the number of cycles is typically limited to 30 to

40 cycles. This theoretically results in $2^{30}$ to $2^{40}$ copies which is billions to hundreds of billions of copies. Having a large number of copies compared to the extremely small concentration that is present in actual clinical settings greatly simplifies the detection and quantification of DNA. When combined with fluorescent dyes that fluoresce when bound to DNA molecules, it becomes possible to quantify the amplification process as it is occurring, this technique is known as real-time or quantitative PCR (qPCR.)

### 1.2.2 Sample preparation

PCR is sensitive to many contaminants that can reduce the amplification yield. Some contaminants, known as PCR inhibitors, are commonly found in common sample types ranging from hemoglobin in blood to salts and common proteins [26]. In addition to PCR inhibitors, the nucleic acid source must be removed from the cells or virions that contain them. Care needs to be taken that the buffers used to perform lysis are not themselves PCR inhibitors [27]. It is sample preparation that achieves the task of extracting the nucleic acids from the sample and removes any potential PCR inhibitors so that when PCR is performed, the reaction can successfully amplify and detect the target nucleic acid sequence. Most protocols for sample preparation require a skilled laboratory technician using equipment like pipettes and centrifuges to prepare a sample for PCR. This dramatically reduces the accessibility to PCR as a diagnostic tool. In addition to the RT-qPCR machine developed in my research, I also present two devices for automating and simplifying the sample preparation process. One performs the multiple sample washing steps automatically, removing the need for operator skill. The other is a complete integrated sample preparation device which automates all of the sample preparation steps, from drawing blood, performing lysis, washing, and elusion of the purified sample ready to use for PCR.

## 1.3 Organization of Contents

This dissertation is organized as a collection of several papers. In Chapter 2, a detailed analysis of a CMOS transimpedance amplifier design is presented. This design utilizes the half-shared topology that is instrumental in conservation of die area on-chip for high-density amplifier arrays. The design is incorporated into the following two papers. Chapter 3 presents a complete system for making electrochemical measurements, from the on-chip electrode array to the data acquisition system for interfacing with a PC. The focus of this device is the measurement of neurotransmitter secretion from living cells, so that the effects of various drugs can be studied. The design from Chapter 3 is further developed into the dual-mode chip that is presented in Chapter 4. The dual-mode chip combines the current-sensing transimpedance amplifier design with a voltage-sensing transconductance amplifier for a true dual-mode measurement device with 512 parallel channels. It is capable of the simultaneous measurement of action potential spikes and neurotransmitter release from the high-density on chip microelectrode array. The dual-mode chip enables for a complete study of the interactive process of neurotransmission by measuring both the secretion of neurotransmitters and the action potentials that propagate through a neuronal network. Beginning with Chapter 5, the focus shifts to area of traditional medical diagnostic devices relying on PCR. In this paper, a compact, battery-operated device that is fully capable of performing real-time quantitative PCR is presented. In addition to the compact size, the device is also completely open source, with all the design files made publicly available to achieve the goal of bringing down the cost of PCR and increasing the access of high-quality PCR diagnostics for more people. Next, two devices to prepare samples for a PCR test are presented. Chapter 6 details a device that is based on a typical benchtop method which utilizes magnetic beads to separate out purified nucleic acids from blood. The device is similar in its low-cost construction to the qPCR machine, and its performance is confirmed by using the device with the qPCR machine to detect the

presence of virus from real human blood. Another device is developed in Chapter 7 to perform the same task of sample purification from whole blood for use with a qPCR device, this time based on a syringe. The integration of a complex microfluidic system directly into the body of a syringe enables sample purification to be performed immediately upon drawing blood from a patient. Finally, Chapter 8 summarizes the contents of the dissertation and presents some future studies to be performed and goals based on the work presented here.

# CHAPTER 2: ANALYSIS OF SIMPLE HALF-SHARED TRANSIMPEDANCE AMPLIFIER FOR PICOAMPERE BIOSENSOR MEASUREMENTS

## 2.1 Chapter Notes

In biosensors, there is a large interest in producing large microelectrode arrays for obtaining high-throughput measurements. Using CMOS technology allows for the integration of low-noise and high-performance amplifiers directly on the same silicon chip as the microelectrode array. This benefit allows for extremely high-throughput systems to be designed that perform better than traditional systems that typically require complex wiring, entire racks of amplifiers, and data acquisition systems. However, one cannot simply place an arbitrary number of amplifiers onto a chip without careful circuit design considerations. This paper discusses focuses on the half-shared structure that is a key concept in enabling the high electrode count of 1024 fully parallel channels. The half-shared structure reduces required die area by nearly 50% when sharing 4 branches and does so without a noticeable reduction in the noise performance of the TIA. The design, schematic, theory, and measured performance are included in the paper. Concepts presented in this paper were further developed and used in the dual-mode chip that is presented later in this dissertation in Chapter 4. I am the primary author of this paper that was co-authored by Kevin A. White and Brian N. Kim.[*]

[*] This chapter uses previously published material.  from Geoffrey Mulberry, Kevin A. White, Brian N. Kim, Analysis of Simple Half-Shared Transimpedance Amplifier for Picoampere Biosensor Measurements, IEEE Transactions on Biomedical Circuits and Systems, April 2019 [90]

## 2.2 Introduction

A transimpedance amplifier (TIA) is used in bioelectronic systems to measure currents in biological applications, including *in vivo* and *ex vivo* dopamine measurements [28]–[30], single-cell amperometry [31]–[35], photoplethysmography (PPG) [36]–[38], pulse oximetry [39], and nanopore recordings [40], [41]. They traditionally consist of a circuit to transform the current into the electrode into a voltage measurement. To implement a TIA, most low-noise measurements use an operational amplifier (OPA) to hold an electrode or a photodiode at a reference voltage while converting the current at the electrode or photodiode into voltage, thus forming a transimpedance amplifier. As such, TIAs on integrated CMOS devices usually contain OPAs within them. For high-throughput (large-scale) measurements from an array of detectors, a larger number of amplifiers is required. Thus, it is crucial to minimize the size requirements of each TIA if a larger scale recording is desired. One approach for minimization of TIAs is the half-shared structure of the OPA, which is explored and analyzed in this paper. The approach is powerful, as it enables the doubling of amplifiers on a single chip, increasing throughput for demanding applications. However, few in the field have been using the technique for their designs, possibly due to a lack of awareness and analysis of the concept which will be addressed by this paper. The half-shared design has been successfully adapted in previous studies to yield large-scale recordings, ranging from tens to thousands of amplifiers [31], [34], [35], [42]–[44]. The design principle of a half-shared OPA is to allow for the non-inverting half to be shared between multiple OPAs, reducing the required die area for multiple OPAs by nearly a factor of two. In an effort to have high bandwidth and a wide dynamic range, a folded-cascode architecture was used for the early half-shared amplifiers [31]. This folded-cascode architecture achieves wide dynamic range and bandwidth at the cost of high power (nearly double) and area consumption. However, if used for most electrophysiology or photodiode applications, the required bandwidth is small (< 20 kHz).

Additionally, many CMOS detector arrays for biomedical applications operate below 20 kHz, usually in the 10 kHz region [42], [45]. This low bandwidth can be easily obtained with a traditional five transistor (5T) OPA, further eliminating significant benefits to the folded-cascode architecture. Thus, the 5T OPA design is adapted in this work to minimize the power and area consumption. The half-shared structure has been analyzed in the past for a limited amount of scalability, usually, two OPAs sharing one non-inverting half [31], [46]. In this paper, we will expand the analysis for an unspecified number of sharing branches to evaluate the effect and implications for larger scale recordings (Section 2.3). Using the half-shared design, an integration-based TIA is designed and tested. The noise analysis of non-stationary circuits, such as an integration amplifier, is a challenging task. This is because most noise simulations assume a steady-state in the time-domain for the frequency-domain analysis. In order to evaluate the noise characteristics of non-stationary TIAs, we produced a simple approach to convert the integration amplifier to a stationary circuit for the noise analysis and applied post-signal-processing to simulate the non-stationary effect (Section 2.4). To study the 5T half-shared OPA structure, a CMOS chip [34] was designed and fabricated using a 0.35 μm 4M2P process. Since the techniques described in this paper are valid for all process nodes, a 0.35 μm process was chosen as a cost-effective means to fabricate this proof-of-concept work. These techniques can be implemented on any modern analog CMOS process to further reduce die area required for large arrays. In biological applications, the voltage required to monitor or stimulate the electrophysiological processes is often larger than few volts and the larger dynamic range of large process nodes, such as 0.18 and 0.35 μm, is useful. Section 2.3 discusses the design of the TIAs, OPAs, and array in detail. In short, the CMOS chip consists of a total of 1024 array elements arranged into a 32 × 32 grid. The TIAs within each array element are based on OPAs utilizing the half-shared design and have additional circuitry allowing

for reconfiguration for testing and different modes of operation. Although each TIA relies on the half-shared OPA architecture, they are effectively independent from the others, allowing 1024 parallel measurements. The fabricated circuit is used to characterize the performance of the half-shared design, including gain, linearity, noise, mismatch, bandwidth, and crosstalk (Section 2.5)

## 2.3 Transimpedance Amplifier Array Design

The half-shared OPA design is described within this section along with how they are used within the TIAs and array elements and the overall structure of the array. The TIAs used rely on a rather simple design of OPA. Although rudimentary, the 5T OPA's lend themselves well to half-sharing, use low power, require little die area, and their performance within the presented TIA design is sufficient as will be demonstrated in sections 2.4 and 2.5.

### 2.3.1 Half-Shared Amplifier Design

The enabling feature of this array's high density is the half-shared architecture used for the OPAs within the TIAs. The basis of the half-shared design exploits redundancies that occur when traditional 5T OPAs in the negative feedback configuration are used in parallel, and their non-inverting inputs share the same voltage. A half-shared OPA schematic is presented in Figure 2.1. Here, $M_0$ and $M_1$ form a differential pair, where $M_{bias}$ provides a bias current, and $M_{L0}$ and $M_{L1}$ form a current mirror load for the differential pair. The non-inverting and inverting inputs are the gates of $M_0$ and $M_1$, respectively. The output is taken at the drains of $M_{L1}$ and $M_1$.

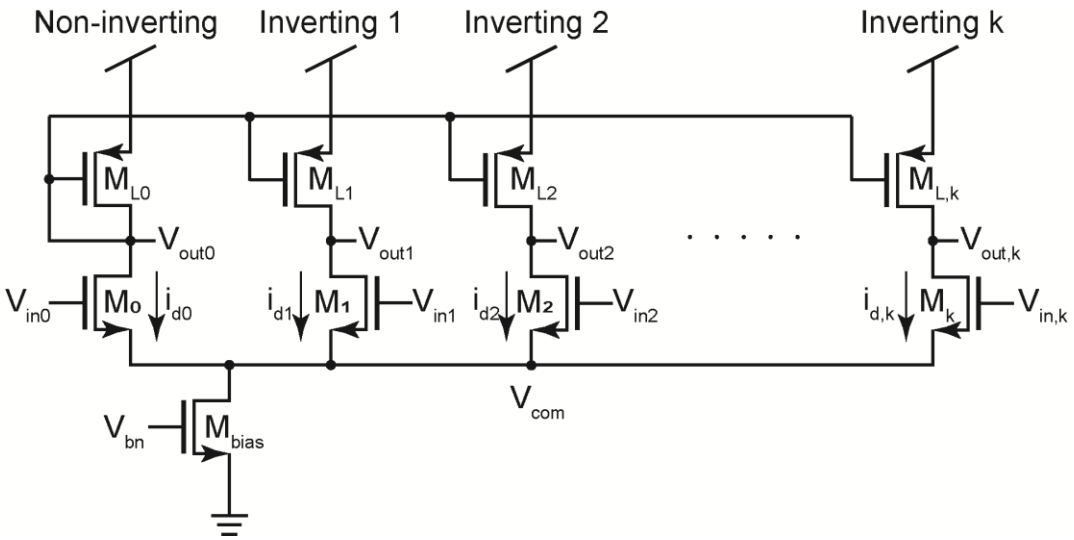


Figure 2.1. A half-shared design with k-counts of inverting amplifier shared a single non-inverting half. Transistors $M_0$ and $M_{L0}$ form the non-inverting half and $M_1$-$M_k$, $M_{L1}$-$M_{L,k}$ form inverting halves of additional OPAs. All NMOS and PMOS bulk connections are to ground and $V_{DD}$ respectively. © 2019 IEEE

Usually, if a second 5T OPA is added, five additional transistors would be required. However, if the bias current and the non-inverting input voltage are the same for the two OPAs, the only two additional transistors are required. This is due to the redundancy within the non-inverting half. Thus $M_{L0}$ and $M_0$ can be shared between the two OPAs. In this example, $M_{L2}$ and $M_2$ are all that is required to add a second OPA. For the second OPA, $M_2$ and $M_0$ form the differential pair where $M_2$'s gate is the second inverting input. Conceptually, this method can be extended to any amount of additional OPAs.

### 2.3.2 Analysis of Half-Shared Structure

The circuit in Figure 2.2 shows multiple inverting half amplifiers sharing a single non-inverting half. To examine the tradeoff of multiple inverting halves sharing a single non-inverting half, the small signal gain of each branch is analyzed. The purpose of this analysis is to evaluate the performance of the half-shared structures before it is placed and used as a part of our TIA. The current in the non-inverting half can be expressed:

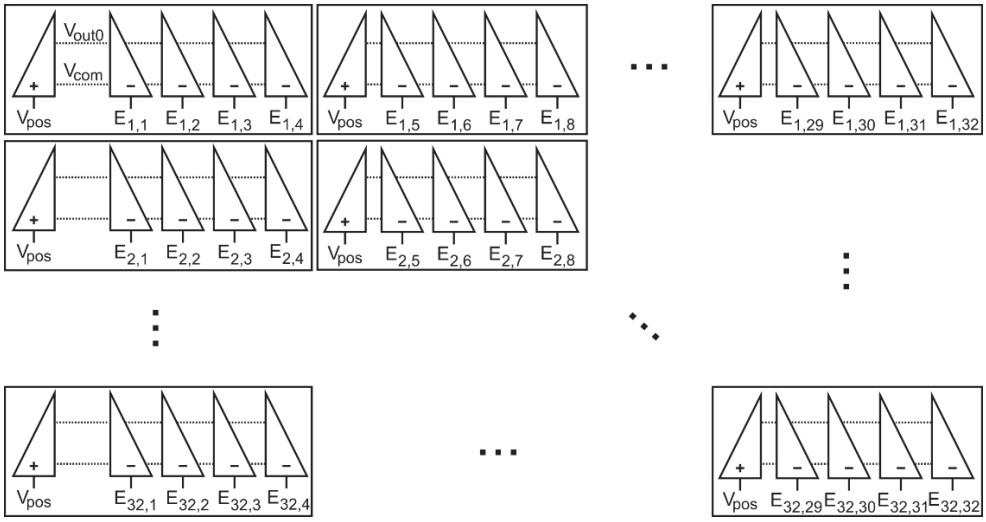


Figure 2.2. Block diagram of the CMOS design containing 1024 half-shared amplifier array elements. Each block consists of a group of four amplifiers using the half-shared architecture to save silicon area while increasing the number of on-chip amplifiers. Each OPA is represented as cut in half, with the right half being the inverting side located within a corresponding TIA, and the left half being the non-inverting half common to each block of four amplifiers. The array is eight groups of four amplifiers wide and 32 rows tall to create a total of 1024 amplifiers. Each inverting inputs are labeled with its *row-* and *column-* coordinate position as their indices. © 2019 IEEE

$$i_{d0} = g_{m0}(v_{in0} - v_{com}) \tag{2.1}$$

where $gm_0$ is the transconductance of $M_0$.

Assuming the transconductances of $M_0$, $M_1$, $M_2$, and $M_k$ are equal, currents in inverting halves can be generally expressed:

$$i_{d,k} = g_m(v_{in,k} - v_{com}) \tag{2.2}$$

where $k$ is the $k^{th}$ inverting half amplifier sharing the common non-inverting half. Because $M_{bias}$ supplies constant current for biasing, it is removed from the small signal circuit, thus

$$i_{d0} + i_{d1} + i_{d2} + \cdots + i_{d,k} = \sum_{n=0}^{k} i_{d,n} = 0 \tag{2.3}$$

From Eqs. (2.1), (2.2) and (2.3), we can establish $V_{com}$:

$$V_{com} = \frac{\sum_{n=0}^{k} v_{in,n}}{k+1}. \tag{2.4}$$

Load transistors, $M_{L0}$, $M_{L1}$, $M_{L2}$, and $M_{L,k}$, form a current mirror and thus currents through these transistors are equal.

$$i_{L0} = i_{L1} = i_{L2} = i_{L,k} = i_{d0} \tag{2.5}$$

The current entering the node $V_{out,1}$ is

$$i_{out,1} = i_{L0} - i_{d1} = i_{d0} - i_{d1}, \tag{2.6}$$

and this current used to generalize other halves' output current,

$$i_{out,k} = i_{d0} - i_{d,k} \tag{2.7}$$

Because $v_{out,k}$ is loaded by the output resistance of $M_{L,k}$ and $M_k$, $r_{L,k}$ and $r_k$, $v_{out,k}$ can expressed:

$$v_{out,k} = (r_{L,k} // r_k) \cdot i_{out,k} \tag{2.8}$$

Using Eqs. (2.2), (2.3), (2.4), and (2.7),

$$\begin{aligned} v_{out,k} &= -(r_{L,k} // r_k) \cdot (\textstyle\sum_{n=1}^{k} i_{d,n} + i_{d,k}), \\ &= -g_m \cdot (r_{L,k} // r_k) \cdot [(\sum_{n=1}^{k} v_{in,n}) + v_{in,k} - (k+1) \cdot v_{com}] \\ &= -g_m \cdot (r_{L,k} // r_k) \cdot [(\sum_{n=1}^{k} v_{in,n}) + v_{in,k} - (\sum_{n=0}^{k} v_{in,n})] \\ &= -g_m \cdot (r_{L,k} // r_k) \cdot (v_{in,k} - v_{in0}). \end{aligned} \tag{2.9}$$

In Eq. (2.9), we can see that the output ($v_{out,k}$) of a particular inverting half is only dependent on $v_{in,k}$ and $v_{in0}$, not related to other inverting halves' inputs. Thus, multiple inverting halves can

operate independently without suffering crosstalk. This analysis also reveals that there is no obvious limit on how many inverting halves can be attached to share a single noninverting half.

In the half-shared design, the bias current of each amplifier is provided from $M_{bias}$. Therefore, if the number of inverting half amplifiers increases to share the single non-inverting half, the current level through $M_{bias}$ should linearly increase to supply consistent levels of bias to individual amplifiers. This requires $V_{bn}$ to be elevated. To operate $M_{bias}$ in saturation, $V_{com}$ needs to be increased with $V_{bn}$, which will limit $V_{bn}$–$V_{com}$ to be less than the threshold voltage. Thus, one apparent tradeoff of increasing the number of sharing amplifiers is the reduced dynamic range of $V_{in,k}$ and $V_{out,k}$. This effect could be reduced by increasing the width of $M_{bias}$, however, since the objective of half-sharing is to reduce die area, $M_{bias}$ must be sized as a compromise between size and number of shared branches.

### 2.3.3 Large Array Design Using Half-Shared Structure

The large array of densely packed TIAs consisting of 1024 amplifiers on a single CMOS chip uses the half-shared structure to its advantage. In this case, we chose to have four inverting amplifiers to share one non-inverting half considering the required dynamic range for biomedical applications. For the large array, an important design requirement is that, for this architecture to work properly, transistors $M_0$, $M_1$, $M_2$, $M_3$, and $M_4$ must all be matched sizes, as well as load transistors $M_{L0}$, $M_{L1}$, $M_{L2}$, $M_{L3}$, and $M_{L4}$. If the sizes are not matched, then the individual half currents will be unequal and Eqs. (2.5), (2.6), (2.7), and ultimately (2.9) will be invalid. The consequence of poor matching is that the inverting halves will no longer be independent. The arrangement of the TIAs for the large array is shown in Figure 2.2. A 32 × 32 grid is used to arrange the 1024 amplifiers as densely as possible. Along any given row, eight half-shared blocks are used where every group of four amplifiers along the row are part of a half-shared block. Using this arrangement of eight half-shared blocks allows 32 TIAs to fit in the same die area that could fit only 17 TIAs using traditional 5T OPAs. This increase in

packing density provides an effective method for increasing the throughput of parallel measurements. The $V_{pos}$ terminals of the eight half-shared blocks in each row are connected together and are additionally connected to all 32 rows. This enables a global $V_{pos}$ for setting all 1024 electrode potentials when performing current measurements in electrolytic solutions. Such measurements are the basis for single-cell electrophysiology and amperometry experiments. Each column has its own analog output enabling entire rows of 32 TIAs to be read out simultaneously row after row. While one row is being read out, the other 31 in the same column are performing integration of their electrode currents, enabling a true 1024 simultaneous measurements without deadtime. The detail of the staggered time-division multiplexing is previously described by the authors [35], [43].

### 2.3.4 Programmable TIA

Figure 2.3 shows the schematic for one of the 1024 TIAs using the half-shared amplifier. Each TIA contains 11 MOSFETs, a half-shared OPA, an SRAM and two capacitors. The TIA design is based on a regulated cascode amplifier (RCA). The current at the electrode is integrated at the drain node of $M_9$ which is then measured as a voltage by $M_{10}$ and $M_{11}$, periodically ($t_{int}$). Normally, an integrating capacitor ($C_{int}$) should be placed at the drain node of $M_9$ which sets the transimpedance gain ($G_Z$) of the RCA. The gain can be expressed:

$$G_Z = \frac{t_{int}}{C_{int}} \ (V/I) \tag{2.10}$$

To maximize the transimpedance gain, the parasitic capacitance (<10 fF) which exists at the drain node of $M_9$ is used. The integrating TIA design achieves similar or better noise performance compared to a resistive TIA, but with a high area efficiency due to the lack of the resistor. $M_1$ forms half of a current mirror used to set a calibration current through the TIA via $I_{cal}$, mainly for testing the

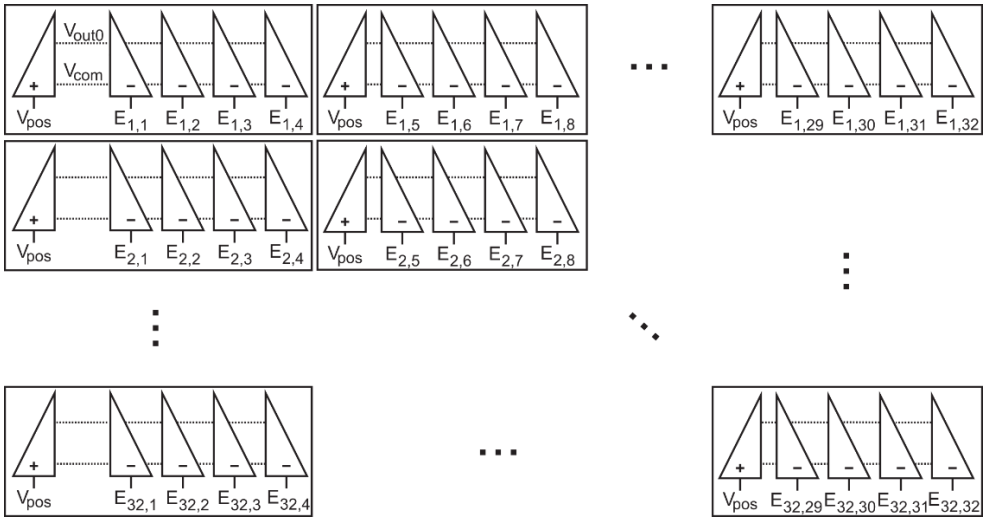


Figure 2.3. Schematic of an individual transimpedance amplifier element. The circuit is a reconfigurable and programmable using the embedded SRAM. The design includes the inverting half of an OPA and shares the non-inverting half which is separated so it can be shared with three other amplifiers. Similar to Figure 2.1 and Figure 2.2, the shared nodes $V_{out0}$ and $V_{com}$ are represented as dashed lines, showing the connections of the half-shared OPA blocks. $V_{out,k}$ is the output of the non-inverting OPA half for this TIA element. © 2019 IEEE

half of a current mirror used to set a calibration current through the TIA via $I_{cal}$, mainly for testing the transimpedance gain but also to allow the measurement of negative currents. Because we intended to operate the OPA with extremely low power, the phase margin of the RCA can be low with poles from the OPA and $M_9$ source, closely overlapping. Optional phase compensation can be enabled when PC (phase compensation switch enable) is high by turning on switches, $M_2$ and $M_3$ and inserting $C_{PC}$ into the feedback loop, thus increasing the phase margin. The integration capacitance is reset by switch $M_4$ every integration period ($t_{int}$). The TIA has two programmable gain settings enabled by $C_{LoG}$. $C_{LoG}$ can be added to the parasitic integration capacitance by turning on switch $M_8$ to decrease the gain in low-gain mode by setting LoG low. Thus, in the low-gain mode, the integration capacitance is a summation of $C_{LoG}$ and the parasitic capacitance. The TIA can be connected to an external electrode pad, ExConE, by turning on switch $M_7$ when the SRAM is set high. An additional function of the SRAM

is to use the OPA to be in the unity-gain mode when SepHold and the SRAM are both high. When both $M_5$ and $M_6$ are on, the inverting input of the OPA and the output are shorted, enabling unity-gain. Every TIA has a dedicated SRAM within the 900 $\mu m^2$ for the fully-addressable programmable array. Switch $M_{11}$ allows for connection to the column's output buffer, where $M_{10}$ is one of the output buffer transistors when RowSelect is high. The minimum dimension is used for all switch transistors. For best matching characteristics, analog transistors $M_9$ and $M_{10}$ are square.

For this array design, each array element is set to be 30 $\mu m \times 30$ $\mu m$. This is to integrate the entire 1024 amplifier array in less than a 1-$mm^2$ area. Transistors for the OPAs, $M_{bias}$, $M_k$, and $M_{L,k}$, are sized at 10 $\mu m \times 10$ $\mu m$ to minimize mismatch. Without the half-shared architecture, the gates of the transistors alone for a single OPA require 500 $\mu m^2$ or 55.8% of the 900 $\mu m^2$ available for each array element. This would leave insufficient area for the remaining circuitry shown in Figure 2.3. However, with the half-shared structure, only 2 OPA transistors must fit into each array element, requiring 200 $\mu m^2$ or 22.2% of the array element area, allowing for the addition of the extra circuitry.

## 2.4 Noise Analysis of Non-stationary Circuit

The integration TIA has an integrating node where voltage can swing up to 2 volts within the integration period, which then resets after each integration cycle. Thus, this circuit is non-stationary in the time-domain and the simulation in the frequency-domain is difficult to implement. Thus, in this section, we are exploring a conversion method to estimate the noise performance for a non-stationary circuit using a typical simulation tool.

### 2.4.1 Non-Stationary Circuit

The integrating circuit is only functional if the integration capacitor is periodically reset. Without the periodical reset, the charge in the integration node discharges completely which disables the TIA. Thus, the circuit in Figure 2.3 cannot be used for a typical AC/noise analysis. This non-

stationary circuit can be converted to a stationary circuit by replacing the integration capacitor to a resistor. The value of the resistor should be:

$$R = G_Z = \frac{t_{int}}{C_{int}} \ (V/I) \tag{2.11}$$

where the resistance is identical to the transimpedance gain set by the integration period and integration capacitance. The resistor-based circuit is then used for the noise analysis with the noise model provided by the semiconductor manufacturer. The noise measured at the integration node consists of various noise sources from the OPA, cascode transistor ($M_9$), and the resistor. This analysis does offer some insight into the characteristics of the TIA's noise but fails to capture the effect of the current integration. The current integration for the set duration in a time domain creates a convolution of a rectangular pulse (Figure 2.4a).

$$i_{TIA}\,(t) = i_{int}(t) * rect(t) \tag{2.12}$$

where the *rect(t)* is the rectangular function (1 for arguments within a window of period $t_{int}$, and 0 for all arguments outside of the window) and $i_{int}$ is the current measured at the integration node. This expression can be transformed to the following equation:

$$I_{TIA}\,(f) = I_{int}(f)Y(f) \tag{2.13}$$

where Y(f) is the Fourier transform of the rectangular function. The unitary Fourier transform of *rect(t)* is:

$$Y(f) = \int_{-\infty}^{\infty} rect(t) \cdot e^{-i2\pi ft} dt \tag{2.14}$$

Thus, the frequency response can be expressed as a *sinc()* function.

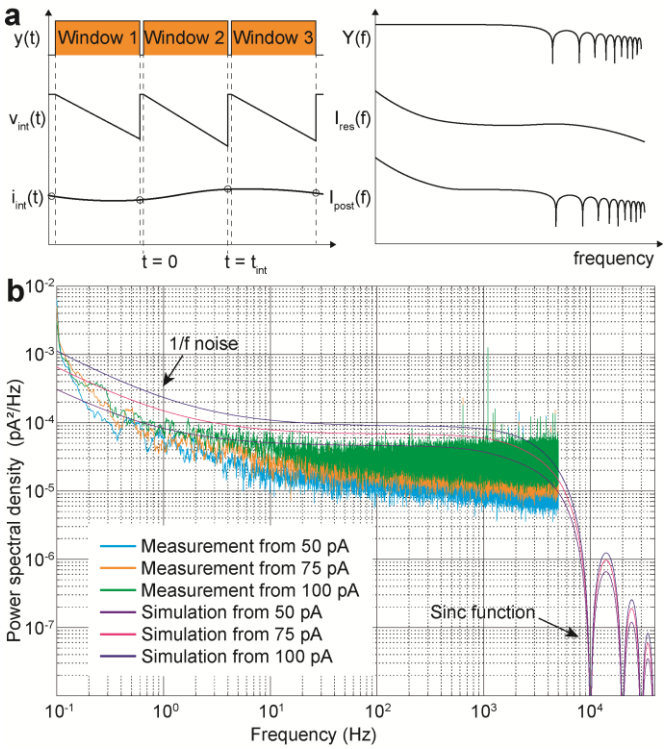


Figure 2.4. Characterization of noise using simulation and chip measurement. (a) The current integration creates windows for each integration period and reports the current level at the end of each integration cycle. The window in time-domain generates a *sinc()* function in the frequency domain which can be used to estimate the noise performance in the non-stationary circuit. (b) Noise analysis from the simulation is compared with the chip measurements for various input current levels, 50 pA, 75 pA and 100pA. © 2019 IEEE

$$Y(f) = \frac{\sin(f \cdot \pi \cdot t_{int})}{f \cdot \pi \cdot t_{int}} = sinc(f \cdot \pi \cdot t_{int}). \tag{2.15}$$

The multiplier, $\pi \cdot t_{int}$, is to adjust the *sinc()* filter for the specific rectangular function which has the $t_{int}$ window. Any input passing Y(f) with $1/t_{int}$ interval frequencies should have zero output. To generate the equivalent noise analysis from the stationary circuit to the non-stationary circuit, a post-signal-processing can be applied by multiplying the noise measurement from the simulation with Eq. (2.15).

$$I_{post}(f) = I_{res}(f)Y(f) \tag{2.16}$$

Therefore, $I_{post}(f)$ closely estimates $I_{TIA}(f)$ in Eq. (2.13). One difference is the thermal noise added by the resistor in the simulation. This effect can be extracted from Eq. (2.16) if relevant. Since the gain we are simulating is 7.00 mV/pA, the resistor we use is 7 GΩ. The thermal noise of the 7 GΩ resistor is only $\sim 2 \times 10^{-6}$ pA$^2$/Hz and is significantly smaller than the typical noise in the TIA, so we have ignored it in the analysis. The simulated noise is shown in Figure 2.4b with the measured noise from the CMOS chip at various input current levels, 50 pA, 75 pA, and 100 pA. All noise measurements show $1/f$ noise at low frequencies. At high frequency, the effect of post-signal-processing of adding *sinc()* response is observed as expected. For all three input current levels, the noise levels between the measurement and the simulation are within a factor of 5, which reveal the discrepancy of the noise characteristic in deep weak inversion. The input current below nano-ampere is considered deep weak inversion and the noise model provided by the manufacturer are generally optimized for strong inversion transistors. Therefore, for any amplifiers operating with pico-ampere current levels, the noise characteristic can be better evaluated by measurements, rather than modeling and simulation. Nonetheless, the simulation method presented here does provide a viable method to estimate the noise level and the frequency characteristics within a factor of 5 before the CMOS fabrication.

## 2.5 Characterization and Measurement

To demonstrate the effectiveness of the half-shared architecture, the fabricated CMOS array was used for several experiments using the test setup shown in Figure 2.5. This section contains measurements of a representative column's output, transimpedance linearity, amplifier mismatch of the 1024 TIAs, and frequency response.

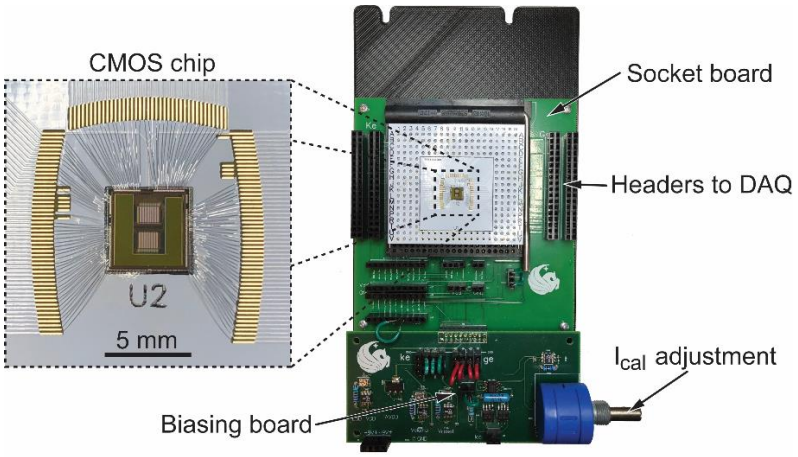


Figure 2.5. Overview of the measurement system. The CMOS chip is bonded to a PCB which is inserted into a socket on the socket board. The socket board allows for connections to the National Instruments DAQ unit and to the biasing board. The biasing board converts battery or power supply voltage into $V_{DD}$, $V_{reset}$, $V_{pos}$, and $I_{cal}$. $I_{cal}$ is easily adjustable via the 10-turn potentiometer. © 2019 IEEE

### 2.5.1 Transimpedance Measurement

The half-shared TIA's transimpedance conversion performance is studied by first configuring the amplifiers to low gain mode, applying a known DC $I_{cal}$ input (from 0 to 1000 pA), and measuring the output waveforms. The array is equipped with multiplexers as previously described in [34], [43] to reduce the number of outputs. 32 TIAs in a column share a 32-to-1 time-division multiplexer. The waveforms resulting from this multiplexed transimpedance measurement are shown in Figure 2.6. The separate traces represent the voltage output versus time of a single column's output at a specific $I_{cal}$ level. The square shape of the pulses resulting from the correlated double sampling (CDS) output stage are clearly shown. CDS allows for the removal of the offset produced by $V_{reset}$ by sampling at both the reset and output values and performing a subtraction. The left plot shows the output from a single column measurement (the pulses are the 32 TIAs in that column). The inset plot shows only four rows of the same output, which more clearly shows the linearity of the output voltages for the

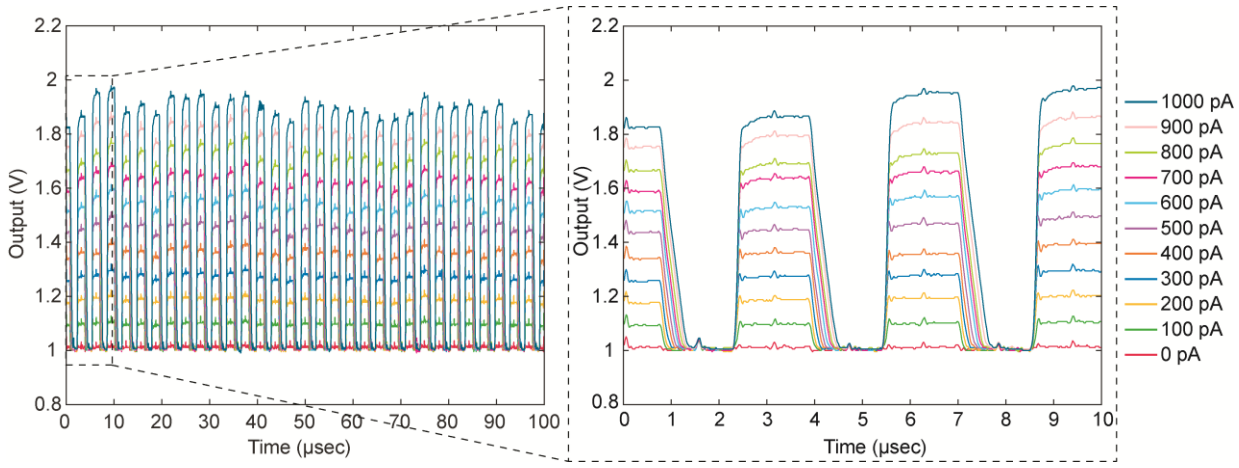


Figure 2.6. Chip's output waveforms show a multiplexed output of 32 TIAs for various input current levels into $I_{cal}$ from 0 pA to 1000 pA. Each pulse represents the output of a single TIA. © 2019 IEEE

first four TIAs in the column. The different heights of the pulses indicates a difference in gain of each of the amplifiers. The difference in gain between the amplifiers is likely caused by process variations such as the dimensions of the transistors, causing mismatch of the OPA inputs, and the dimensions of the integrating capacitors. Parasitic capacitance variation across the array could also affect the gain, so care must be taken in the layout to ensure that the array elements are identical. It is important to note however, that these variations may vary between array elements but should be consistent within any given array element. As a result, the variations can be calibrated out by applying known signals via $I_{cal}$ and recording the gain of each amplifier before taking measurements.

### 2.5.2 Transimpedance Gain Linearity

The TIA's linearity performance is evaluated by using the data from the transimpedance recording shown in Figure 2.6 and creating the voltage versus current plot shown in Figure 2.7a. The results from all 32 TIAs' outputs are used to create a least-squares linear fit of $V_{out}$ against $I_{cal}$. Based on the fit, the transimpedance gain of the low-gain mode is 0.86 mV/pA. The resulting fit has an $R^2$

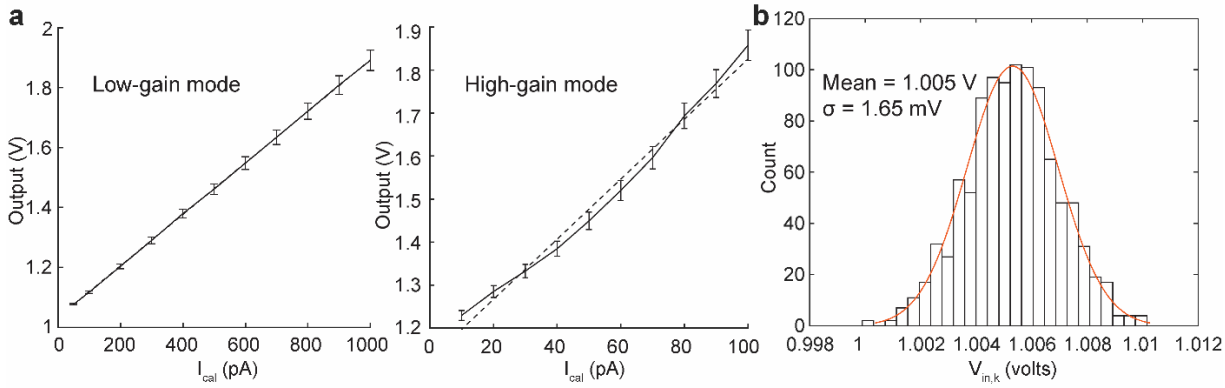


Figure 2.7. The current-to-voltage and mismatch characteristics of TIAs. (a) For each input current between 0 pA – 1000 pA, TIAs' outputs are plotted for both high-gain mode and low-gain mode. Based on the linear fittings, the transimpedance gains of each mode are 0.86 mV/pA and 7.00 mV/pA, for low-gain and high-gain modes, respectively. Linearity fittings indicate a high-quality linearity. The error bars are used to show the standard deviation of 32 TIAs. The dashed line shows the linear fits. The line's equation is $V_{out} = a + b \cdot I_{cal}$, where a = 1.03 V, b = 0.86 mV/pA for the low-gain mode, and a = 1.13 V, b = 7.00 mV/pA for the high-gain mode. (b) The voltage mismatch of each TIA for the entire array is 1.65 mV, which is a small variation due to the closely-matching transistor size (input transistor and load transistor). © 2019 IEEE

value of 0.999, indicating a high-quality linear performance of the TIAs. We have performed the same measurement for the high-gain mode. The transimpedance gain of the high-gain mode is 7.00 mV/pA, and the $R^2$ value is 0.988. The relatively low coefficient of determination in the linear fitting for the high-gain mode is apparent in Figure 2.7a which has a small curvature around 50–60 pA. This is likely due to the nature of parasitic capacitance which is mainly composed of junction and gate capacitors at the integration node. To study the linearity of the entire array, $I_{cal}$ is also measured from all 1024 amplifiers at 700 pA and 200 pA and the gain of each amplifier is calculated. For this measurement, the gain is 0.862 mV/pA with a standard deviation of 0.034 mV/pA.

### 2.5.3 Mismatch

Small differences in transistors' sizes within the OPA can cause a voltage mismatch between the inverting and noninverting inputs. The mismatch is due to the fabrication process variation.

Depending on the application, the inverting inputs control the electrode voltage and accuracy of this voltage can be important. Because the CMOS chip designed in this work features 1024 OPAs, the matching performance is worth evaluating. To test this, the array elements are programmed to unity gain mode and individually connected to the external electrode so that a simple mismatch measurement could be performed. As discussed in Section 2.3.4 and shown in Figure 2.3, unity gain mode connects the OPA's output directly to the inverting input. The non-inverting input is held at $V_{pos}$, and the output voltage is measured at the ExConE. If the OPAs have no mismatch, every OPA will produce exactly $V_{pos}$ at its output. A custom-made LabVIEW program is used to control a National Instruments data acquisition system automating the SRAM programming and measurement of each individual array element's output as quickly as possible to reduce deviation due to environmental variables such as temperature. Each measurement is used to plot a histogram of output voltage measured at the ExConE (Figure 2.7b). The measurement results in a mean output voltage of 1.005 V and a mismatch standard deviation of 1.65 mV for the entire 1024 TIAs. Mainly, the large area investment to $M_{L,k}$ and $M_k$ in each OPA (Figure 2.1) contributes to the small deviation.

### 2.5.4 Bandwidth

In operating the TIA design, it is ideal to have the dominant pole of the transimpedance measurement to be determined by the *sinc()* function created by the current integration (discussed in Section 2.4.1) This can only be achieved if the other poles from the OPA and $M_9$ (in Figure 2.3) are higher than the pole from the *sinc()* function. The pole from the *sinc()* function is a function of the integration window size based on Eq. (2.15),

$$sinc^2(f_{BW} \cdot \pi \cdot t_{int}) = \frac{1}{2}. \tag{2.17}$$

Thus, the pole can be determined based on the following expression,

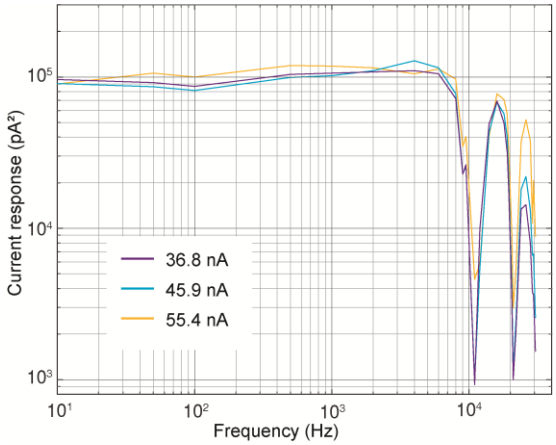


Figure 2.8. Frequency response showing the bandwidth of the TIA at different subthreshold biasing levels, 36.8 nA, 45.9 nA, and 55.4 nA. All recordings show near 4.4 kHz bandwidth which is caused by the dominant pole generated by the current integration performed at 10 kHz. This measurement indicates at any given biasing levels, the dominant pole is produced by the *sinc()* function, instead of the pole from the OPA. © 2019 IEEE

$$sin(f_{BW} \cdot \pi \cdot t_{int}) - \frac{1}{2} \cdot f_{BW} \cdot \pi \cdot t_{int} = 0 \tag{2.18}$$

In the case when tint is 100 µs, $f_{BW}$ is ~4.43 kHz. So long as the other poles do not fall below 4.43 kHz, the dominant pole of this TIA design is the pole from the *sinc()* function. The bandwidth of the half-shared TIA is measured using three different bias currents, 36.8 nA, 45.9 nA, and 55.4 nA, for each TIA. Phase compensation is also enabled. $V_{pos}$ is set to 1 V. A TIA is set to connect to ExConE, and the ExConE terminal is connected through a 1 MΩ resistor to an analog output of a National Instruments data acquisition unit, allowing for the generation of an AC sinusoid current to be applied to the amplifier. Various frequencies are input while the TIA outputs are measured and plotted as shown in Figure 2.8. When $t_{int}$ is set to 100 µs, the TIA produces the expected ~4.4 kHz bandwidth as well as the expected $sinc^2()$ aliasing sidelobes caused by the integration period. For all three measurements, no observable difference is shown indicating that for any tested biasing levels, the OPA's pole remains higher than 4.4 kHz.

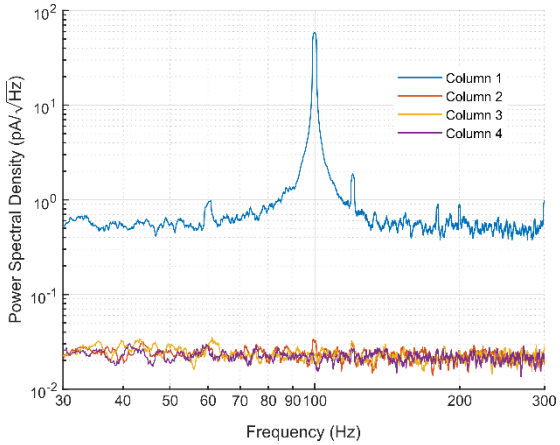


Figure 2.9. Measurement of a half-shared block's crosstalk performance. A 100 Hz signal is injected into column 1 via ExConE, the three shared amplifiers show a heavily attenuated signal present at 100 Hz. The rise in noise floor between column 1 and the others is due to the extra capacitance noise caused by connection to ExConE and the wire to the signal generator. © 2019 IEEE

### 2.5.5 Crosstalk

A major concern for the half-sharing concept is crosstalk between shared channels. Although the small signal analysis from section 2.3.2 shows that the design should not suffer from crosstalk, a measurement is presented in Figure 2.9. For this measurement, row one columns one through four are measured. A 100 Hz sine wave of 400 µV peak-to-peak is injected into the chip's ExConE through a 1 MΩ resistor to produce a 400 pA peak-to-peak current signal. The row one column one TIA is configured to connect to ExConE so the TIA received this current input. Columns two, three, and four exhibit little to no crosstalk from the 100 Hz signal as demonstrated by Figure 2.9. The noise floor discrepancy between the four channels is caused by parasitic capacitance being added to the input of the amplifier for column one due to its connection to ExConE and the wire leading to the signal generator.

## 2.6 Conclusion

In this paper, we are presenting a simple half-shared amplifier structure which can be used for large-scale recordings. Analytical evaluation as well as simulation, and measurement of the fabricated circuit are discussed in detail to show the efficacy of the half-shared design and how it can scale into a large array without a significant trade-off. Many similar arrays require more die area for their amplifiers [31], [33], [42], [43], [47], [48]. Several arrays have increased throughput and reduced die area by using the half-shared architecture [31], [43]. Others have high electrode count, but a low amplifier count, disabling simultaneous full-array measurement [33], [42], [47]. This work builds on previous work and has a high electrode count, with simultaneous full-array measurement, enabled by the half-shared architecture. The performance of the array is compared with other similar arrays in Table 2.1. As discussed in Section 2.3.2, the measurement of each TIA does not suffer from crosstalk because the gain is completely independent (Eq. (2.9)). One notable tradeoff is the reduced dynamic range on each inverting inputs, due to the elevated $V_{com}$. A simulation method is presented which can closely estimate the noise performance of a non-stationary circuit, which has been traditionally difficult to analyze in the frequency domain. The transimpedance gain, mismatch performance, bandwidth, and crosstalk performance are measured from the fabricated circuit to validate the performance. This minimal deviation in mismatch will allow this CMOS device to be useful for most biosensor applications, including single-cell amperometry and nanopore-based nucleic acid measurements. It is interesting to note that, the common-mode rejection ratio (CMRR) of current-measurement amplifiers is not often discussed because the current signal source does not typically carry common-mode signals, in contrast to the voltage sources which almost always have a common-mode signal. However, the implication of the sharing structure to CMRR is worth studying and we are planning on conducting a future research project to investigate the CMRR of a TIA and how it can be quantified in both

Table 2.1: Comparison to Similar Amplifier Arrays © 2019 IEEE

| Reference | [31] | [33] | [42] | [43] | [47] | [48] | This Work [35] |
|---|---|---|---|---|---|---|---|
| **Technology Node** | 0.5 μm | 0.18 μm | 0.5 μm | 0.5 μm | 0.13 μm | 0.18 μm | **0.35 μm** |
| **Die Size** | - | 12 mm × 8.9 mm | 2.5 mm × 2.5 mm | 3 mm × 3 mm | 3 mm × 2 mm | 5 mm × 2.65 mm | **5 mm × 5 mm** |
| **Number of Electrodes** | 25 | 59760 | 100 | 100 | 1024 | 200 | **1024** |
| **Amplifier Size** | 525 $\mu m^2$ | ≥0.04 $mm^2$ | 0.06 $mm^2$ | 900 $\mu m^2$ | 8000 $\mu m^2$ | 0.03 $mm^2$ | **90 $\mu m^2$** |
| **Simultaneous Channels** | 25 | 28 | 25 (4 to 1 multiplex) | 100 | 4 | 200 | **1024** |
| **Noise performance** | ~ 110 $fA_{RMS}$ | 120 $pA_{RMS}$ | 7.2 $pA_{RMS}$ | ~ 100 $fA_{RMS}$ | 56 $pA_{RMS}$ | 480 $fA_{RMS}$ at 110 Hz filtered | **415 $fA_{RMS}$** |
| **Bandwidth** | 2 kHz | 16 kHz | 11.5 kHz | ~1 kHz | 700 Hz | 110 Hz - 10 kHz | **4.4 kHz** |
| **Total Power** | - | 86 mW | 2.1 mW | - | - | 3.21 mW | **12.5 mW** |

analytical and experimental settings. The presented method for reducing die area required for OPAs in TIAs by half sharing is an effective technique as demonstrated by measurements taken from the fabricated 0.35 μm CMOS chip. A four-way half-shared OPA scheme has proven to enable the miniaturization of 32 TIAs into the same space that would traditionally only be able to fit 17 TIAs, which is nearly 50% area reduction while retaining the similar performance. This enables future chips to be designed with an even higher number of electrodes and amplifiers for high-throughput biomedical measurements.

# CHAPTER 3: RAPID 1024-PIXEL ELECTROCHEMICAL IMAGING AT 10,000 FRAMES PER SECOND USING MONOLITHIC CMOS SENSOR AND MULTIFUNCTIONAL DATA ACQUISITION SYSTEM

## 3.1 Chapter Notes

To show the effectiveness and some potential applications of the electrochemical chip I am including this paper which uses the chip based on the half-shared architecture discussed in the previous chapter. This paper demonstrates the electrochemical chip's ability to produce "images" of dopamine diffusion across the surface of the chip's electrode array at 10,000 frames per second. This technology is later incorporated into the dual-mode chip presented in Chapter 4 where the ability to measure the flow of neurotransmitters across a large network of neurons is one of the two primary goals of the design. Another focus of this paper is the discussion of the multifunctional data acquisition system that was developed to operate and produce recordings from CMOS MEAs. Because of the multifunctionality, this data acquisition system is again used for the operation of the dual-mode chip, with a modification using an FPGA rather than the USB 3.0 controller presented here to allow for operation at 40,000 Hz from the dual-mode chip. This paper also describes the post-CMOS processing that is performed to enable the MEA to measure neurotransmitter release which again will be vital for the operation of the dual-mode chip. This paper was primarily authored by Kevin A. White and co-authored by myself and Brian N. Kim[*].

[*] This chapter uses previously published material. © 2018 IEEE. Reprinted, with permission, from Kevin A. White, Geoffrey Mulberry, and Brian N. Kim, Rapid 1024-Pixel Electrochemical Imaging at 10,000 Frames Per Second Using Monolithic CMOS Sensor and Multifunctional Data Acquisition System, IEEE Sensors Journal, July 2018 [34].

## 3.2 Introduction

Electrochemical sensor arrays offer a high spatiotemporal resolution in the study of redox molecule diffusion dynamics, including amperometric recordings of neurotransmitter release at the single-cell level [43], electrochemical imaging of dopamine in brain slices to map the $H_2O_2$ level that associates with neurological diseases [49] and dopamine level which can help study Parkinson's Disease [50], and electrochemical imaging of biofilms [51], [52], glucose [53], and acetylcholine [54]. In electrochemical recordings, the redox molecules can either oxidize, releasing electrons into the electrode that can be measured as negative electrical current, or can induce reduction by taking electrons from the electrode to cause positive current into the electrode. The measurement of electron transfer by electrochemical reaction can be fast, milliseconds to microseconds in temporal resolution, and thus has a unique advantage in capturing the fast dynamics of redox molecule diffusion. Also, the electrochemical recordings can be highly sensitive and specific to electroactive molecules. With high temporal resolution and sensitivity, recent developments have focused on parallelization and miniaturization of sensors and electronics [55]. An array of sensors can be developed to offer simultaneous detection from many electrodes in parallel. In such parallel recordings, the geometric arrangement of the sensor array can be used to construct a spatial resolution from the set of recordings. These measurements require the aforementioned array of electrodes as well as an array of readout circuits to amplify and process the signal originating from each electrode. Large parallel recordings of electrochemical signals impose challenges in developing such instrumentation. For an array with a channel count beyond 1000, the use of commercially-available amplifiers is costly and the direct connection of individual electrodes to their respective amplifier using wiring is impractical. Recently, using microtechnology to manufacture complementary metal-oxide-semiconductor (CMOS) chips has been investigated as an option to scale up the number of parallel recordings to develop a

programmable CMOS 5 × 10 electrochemical sensor array [55], an array of 59,760 electrodes to provide up to 2048 concurrent recordings [56], [57], a monolithic CMOS sensor with 100 on-chip electrodes and 100 parallel recordings[43], a 16 × 16 pixel array on an integrated CMOS device with a frame rate of up to 333 frames per second to study time-varying mixing and diffusion rates of ions [58], and an electrochemical imaging sensor with a 32 × 32 sensor array that produces 90 frames per second [59]. By directly integrating the electrode array on the CMOS chip, the bulk of interconnects can be eliminated and the large-scale integration (LSI) of circuits can be used to integrate a large array of amplifiers and readout circuits in a small silicon chip.

Using an integrated monolithic CMOS sensor still requires an external data acquisition system to enable the complicated functions of the sensor device as well as to record and transfer data into a computer for further analysis. High-performance data acquisition systems add a substantial amount of cost and size to the instrumentation and limits portable applications. The presence of integrated analog-to-digital converters (ADC) in the CMOS sensor can simplify the external acquisition system. However, because monolithic CMOS sensors make direct contact with the biological and/or chemical substance being interrogated, such sensors are generally disposable and intended for single-use. Thus, the use of external ADCs is often more cost effective than integrating ADCs, which occupy a large area in the in the CMOS device, driving up the cost of the disposable devices. With high-throughput applications such as electrochemical imaging, the data acquisition needs to support fast digitization and large data transfer. For example, supporting the operation of a 1,000-pixel electrochemical imager with 10,000 frames per second requires a 10 MHz ADC sampling rate which results in 20 Mbytes/s (MB/s), assuming 2 bytes per sample for 16-bit ADCs. This transfer rate can easily multiply by a factor of two or more depending on redundant sampling for accuracy and noise [43]. Commercially-available

high-performance data acquisition systems are costly with limited options and are unavailable for applications requiring fast sample rates over 100 MS/s and high accuracy 16-bit resolution. Previously, other data acquisition systems have been presented as an alternative to the costly commercially-available acquisition systems [60]–[64] improving sampling capabilities and cost effectiveness. Previous studies have proven the low-cost and portable capabilities of data acquisition systems using Arduino [60], custom-designed PCBs [61], and FPGAs [63], [64], but they are insufficient for many high-throughput applications that require high temporal resolution. For high-throughput applications, the data transfer rate is limited by the selected interface. Common interfaces for fast data transfer are peripheral component interconnect (PCI), PCI Express (PCIe), and universal serial bus (USB). Among those interfaces, USB connection is easy to use and is widely available in almost all computers and laptops. For the ubiquitous USB interface, the transfer rate for USB 3.0 is 5 Gbits/s. Using USB connectivity for such data acquisition systems widens the usability of the system which would have been limited to sophisticated research laboratories. The high-power delivery of USB interfaces from 4.5 W (USB 3.0) to 15 W (type-C) can be used for portable applications by designing a data acquisition system to rely exclusively on USB power. As high-throughput data acquisition is becoming more vital in biotechnology to enable multichannel brain-machine interfacing [65], high-throughput screening (HTS) for drug studies [66], [67], high-throughput electrophysiology recordings[43], and next-generation sequencing [68], USB connectivity introduces a low-cost, simple, and portable option.

In this paper, the comprehensive design of a 1024-pixel electrochemical imaging sensor and multifunctional data acquisition system is presented. In Section 3.3, we describe the design of the monolithic CMOS-based electrochemical sensor. In Section 3.4, we discuss the design and characterization of the multifunctional data acquisition system with 32 parallel ADCs to support the measurements from the CMOS-based sensor. In Section 3.5, we analyze and characterize the high-

performance data acquisition system in conjunction with the CMOS sensor. In Section 3.6, we describe a dopamine diffusion mapping experiment using the comprehensive electrochemical imager, consisting of the monolithic CMOS device and the multifunctional data acquisition system.

## 3.3 Monolithic CMOS Electrochemical Sensor

Neurotransmitters, such as dopamine, can be oxidized at an electrochemical electrode and the released electrons can be directly measured (Figure 3.1). A CMOS device is designed with on-chip electrodes to measure the electrochemical signal directly on the chip (Figure 3.1a). Two-dimensional electrochemical imaging of dopamine diffusion can be performed by using a CMOS device with an array of on-chip electrodes which can probe the electrochemical signal at multiple locations simultaneously (Figure 3.1b). The electrochemical current can be recorded using a transimpedance amplifier (TIA). The recording of a small current and the processing of the signal are performed on the CMOS device. For this purpose, we used an integration capacitor-based TIA design. The current signals, ranging from pA to nA, injected into the electrodes are measured by the TIAs integrating capacitor. The voltage change in the capacitor is read out at a certain interval using correlated double sampling (CDS). The voltage readout is followed by a reset phase to recharge the capacitor using a parallel switch (Figure 3.1c). Each TIA consists of an operational amplifier (OPA), an integrating capacitor (51 fF), a compensation capacitor (20 fF), a 1-bit SRAM, and additional transistors for testing and readout functionality within a 30 × 30 μm area (Figure 3.1c). The transimpedance gain of each TIA is set to 0.54 mV/pA. The noise level for the TIA is measured to be 470 $fA_{RMS}$ at 10 kHz sampling rate with a ~4.4 kHz bandwidth. A time-division multiplexing technique, which staggers the integration period of each amplifier to remove any dead time in recordings due to readout, is adapted and results in the parallel recordings of 1024 electrodes [43]. The array of 1024 TIAs is arranged with 32 columns

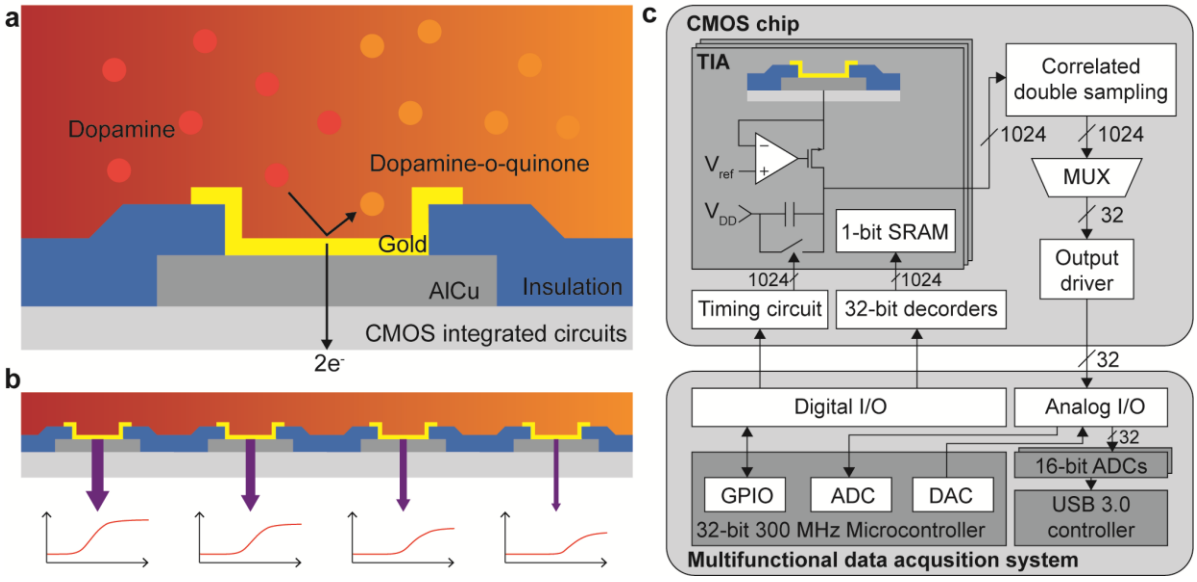


Figure 3.1. Monolithic CMOS electrochemical imaging sensor. (a) Monolithic integration of gold electrodes on a CMOS device can be used to directly oxidize dopamine to dopamine-o-quinone, which results in electrons transferred into the integrated circuits. (b) Using the scalability of the circuits and on-chip electrodes, multiple electrode-amplifier pairs can record electrochemical signals simultaneously. Individual recordings can be used to study the dynamics and diffusion of electroactive molecules. (c) System design of the monolithic electrochemical imaging sensor using a CMOS chip and external data acquisition system. © 2018 IEEE

× 32 rows (Figure 3.2a). In a column with 32 electrode-amplifier pairs, all of the current integrated voltages are time-division multiplexed into a single output, thus providing all 1024 electrode recordings through 32 parallel outputs. This output is fed to an output driver which consists of a unity-gain OPA followed by an nMOS source follower, which drives the output pins of the CMOS device and a load (the input impedance of the external ADC). The timing circuity relies on external clock sources to generate all the clocks required to operate the TIAs and multiplex the 1024 outputs. The timing circuits are designed primarily using traditional transmission gate D flip-flops. The analog outputs and digital inputs for the chip are interfaced with the external multifunctional data acquisition system (Figure 3.1c), which will be described in Section 3.4. The CMOS device is designed and

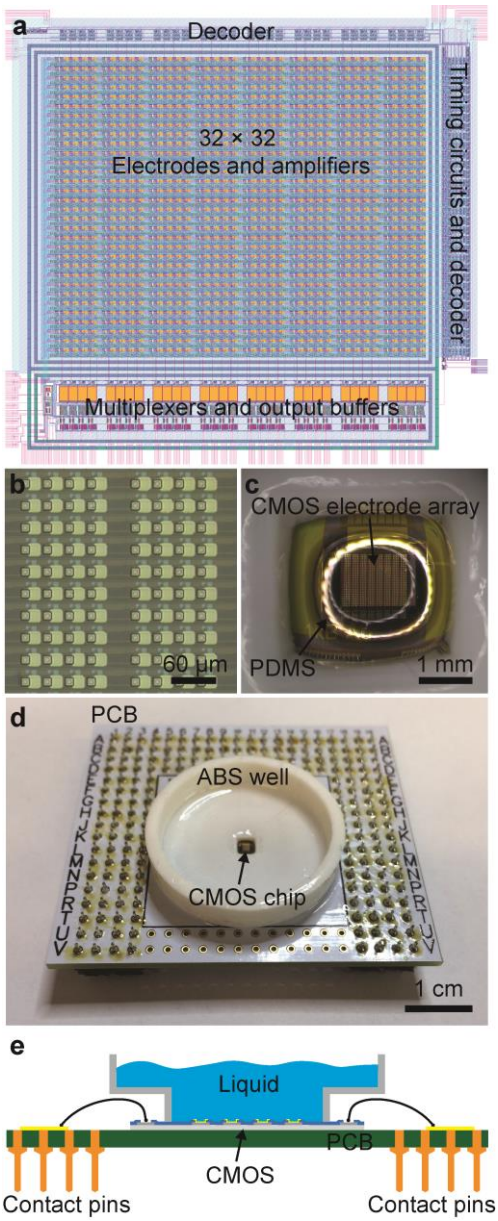


Figure 3.2. Post-CMOS processing and packaging of the monolithic sensor. (a) The layout for the 1024-ch CMOS electrochemical sensor. (b) On-chip gold electrode array with each electrode size of ~15 μm × 15 μm. (c) The CMOS chip is packaged using a 3D-printed ABS well and PDMS, leaving a small opening on the electrode array. (d) The packaged chip on a custom-designed PCB. (e) The cross-sectional diagram of the packaged chip where the 3D-printed well contains the liquid above the electrode array and prevents liquid contact to the wire bonds and other electronic components. © 2018 IEEE

simulated using the Cadence Virtuoso Analog Design Environment. The CMOS chip is fabricated using astandard 0.35 μm CMOS foundry process and the die size is 5 mm × 5 mm, and the detailed specifications are provided in Table 3.1.

Electrochemical recordings require a polarizable electrode, including gold or platinum, to exhibit a high signal-to-noise ratio in measuring oxidative current without background current due to chemical reaction of the electrode itself [69]. However, standard CMOS foundries do not offer polarizable metals in the manufacturing process. Thus, post-CMOS fabrication is performed to monolithically integrate an electrode array on the surface of the CMOS chip. Each chip, fabricated from the foundry, is processed using photolithography to accomplish gold patterning through a lift-off process. Initially, the die is attached to a coverslip (25 mm × 25 mm) to ease the handling of the small substrate. The die is cleaned using acetone, isopropanol (or methanol), and DI water. A negative photoresist layer using NR9-1500PY is patterned, followed by sputtering of 15 nm Ti and 150 nm Au (Figure 3.2b). Lift-off is then achieved by rinsing the die with acetone. Each gold electrode pattern is ~ 15 μm × 15 μm and is connected directly to its respective amplifier through a small insulation opening (Figure 3.1a). After the photolithography process, the CMOS chip is bonded to a custom PCB that allows for the insertion of the CMOS device into a socket. This allows for the same experimental setup to be used with other CMOS chips with ease. The CMOS chip is wire-bonded to this custom PCB and a plastic well is used to protect the wire-bonds from liquid contact (Figure 3.2c). The well is 3D-printed out of ABS plastic and coated with a layer of PDMS, for waterproofing and biocompatibility. The well is then bonded to the custom PCB and CMOS chip using additional PDMS (Figure 3.2d). The well has a small opening in the center to allow access to the surface of the CMOS chip as shown in Figure 3.2e.

Table 3.1: Specifications of the CMOS electrochemical sensor © 2018 IEEE

| Properties | Specifications |
|---|---|
| **Technology node** | 0.35 μm |
| **Die size** | 5 mm × 5 mm |
| **Number of electrodes** | 1024 |
| **Number of amplifiers** | 1024 |
| **Design area per amplifier** | 30 μm × 30 μm |
| **Electrode size** | 15 μm × 15 μm |
| **Noise performance** | 470 $fA_{RMS}$ |
| **Transimpedance gain** | 0.54 mW/pA |
| **Bandwidth** | ~ 4.4 kHz |
| **Sampling rate per channel** | 10 kHz |
| **Accumulated Sampling rate** | ~10 MHz |
| **Electrochemical frame rate** | ~ 10,000 frames/s |
| **Total power consumption** | 12.5 mW |

## 3.4 Multifunctional Data Acquisition System

The multifunctional data acquisition board is used to operate the monolithic CMOS electrochemical sensor (Figure 3.3). The multifunctional data acquisition board provides key capabilities to enable high-throughput applications, including 32-ch 16-bit resolution analog recordings, 16 digital inputs and outputs (I/O), 2-ch 12-bit analog recordings, 2-ch 12-bit analog outputs, and 400 MB/s data transmission over USB 3.0. The system uses a custom-designed PCB and a Cypress FX3 board (Figure 3.3).

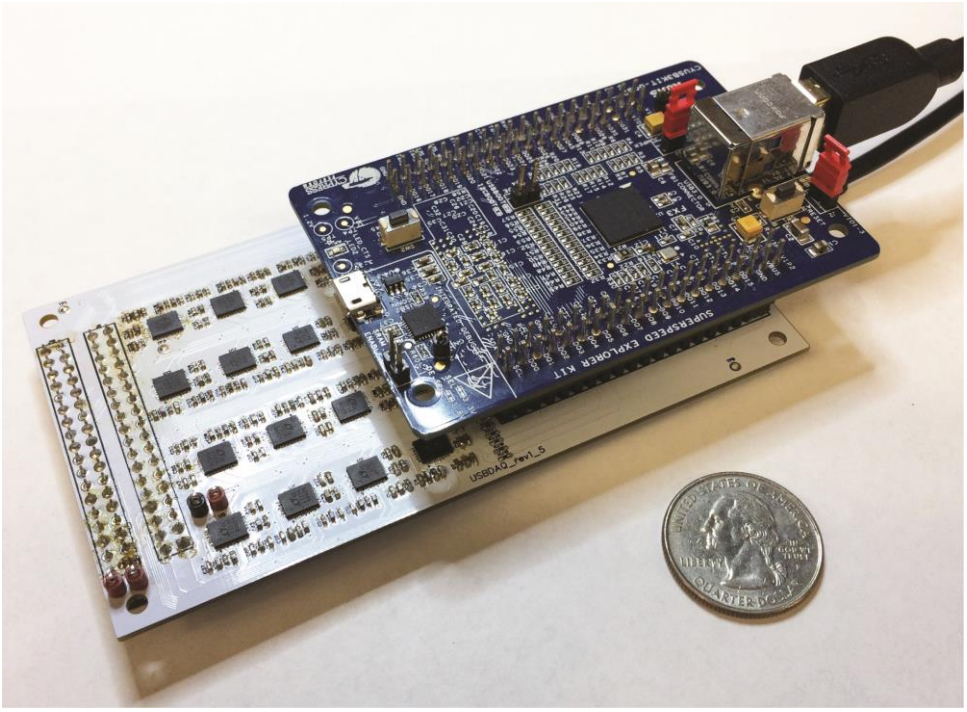


Figure 3.3. The multifunctional data acquisition system. The system consists of a custom-designed PCB (white board) and a USB 3.0 controller board (navy board). The system is capable of 32-ch simultaneous analog recordings with digital I/O and analog output functionalities and can transmit up to 400 MB/s of data over USB 3.0. © 2018 IEEE

### 3.4.1 Design of multifunctional data acquisition system

The Atmel SAME70 32-bit microcontroller unit (MCU) functions as the control center for the data acquisition system and receives commands from a computer through the serial USB port (Figure 3.4). The chip generates all of the clock signals required for the ADCs and USB 3.0 controller to operate synchronously as well as any clock signals required for external devices to operate in sync with the data acquisition system. The MCU chip also provides additional ADCs, digital I/O, and waveform generation using the embedded digital-to-analog converters (DACs).

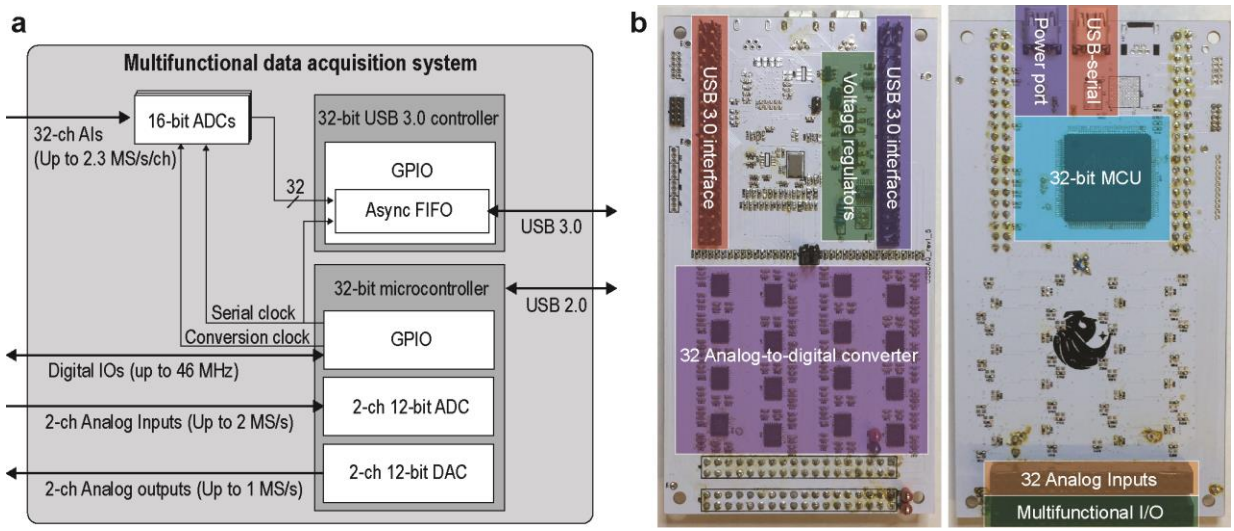


Figure 3.4. Functional blocks and photographs of multifunctional data acquisition system. (a) The system diagram of the data acquisition system consisting of 32 16-bit ADCs, 16 fully-customizable digital I/Os, additional 2-ch ADCs, and 2-ch DACs. The USB 3.0 controller transmits data to the computer at high-speed and the 32-bit MCU communicates with the computer to receive commands for various configurations. (b) The PCB of the acquisition system consisting of 32 ADCs, USB 3.0 interfaces for USB board connection, the 32-bit MCU, voltage regulators, and a versatile I/O interface of 32 analog inputs and multifunctional I/Os. © 2018 IEEE

There are 16 ADC chips (LTC2323-16, Linear Technology) used in the presented data acquisition system. Each ADC chip has two embedded ADCs with an individual maximum sampling rate of 5 MHz, providing a total of 32 high-speed 16-bit ADCs. The board is designed without anti-aliasing filters to offer flexibility in the sampling bandwidth. For each application, appropriate anti-aliasing filters are attached directly to the I/O interface of the data acquisition board. These ADCs convert the 32 parallel analog inputs from the CMOS chip to their 16-bit serial digital representations. The parallel output streams of the 32 ADCs are connected directly to 32 parallel general purpose I/O (GPIO) pins on the USB 3.0 board through the USB 3.0 interface pin headers. The USB 3.0 controller is used to transfer the large amounts of data acquired from the ADCs to a computer with high-throughput. The USB controller accumulates data in its embedded first in, first out (FIFO) memory and transfers data to the connected computer in packets at a rate up to 400 MB/s. The overall size of

the system is 13 cm × 6.3 cm × 3 cm and weights 79.7 g. The system operates using the USB 5.0 V power, and thus can be used for portable applications in conjunction with a laptop.

### 3.4.2 Embedded programming and software

The firmware loaded into the USB 3.0 controller is designed to achieve a slave FIFO interface. This firmware configures the controller to receive a clock signal for synchronous operation from the MCU, record the parallel outputs from the high-speed ADCs, and send packets of data through the USB interface. A data streamer application is created to control the streaming of data from the USB controller to a computer. Additionally, a LabVIEW program is created to execute this streamer application and simply requires the user to start data transfer from the ADCs to the computer. This LabVIEW program specifies where the data is saved by the streamer application and the settings for the streamer are preset for optimal data throughput. The firmware programmed into the MCU provides the capability to operate and activate the multifunctionality of the data acquisition system. When powering up, the MCU will first configure its internal clocks to become operational. After this initialization, the MCU waits for the chip to receive a command from the computer. An MCU LabVIEW interface is developed to provide a user interface for controlling the MCU. This program allows the user to communicate with the chip through the USB serial port and tailor the functionality of the available pins to their needs. Each digital I/O can be individually set, the waveforms generated by the DACs can be changed, and the MCU embedded ADCs can be used for additional analog sampling.

## 3.5 Analysis of High-performance Data Acquisition

The simultaneous recording and multifunctional capabilities of the data acquisition system are tested by operating the high-throughput CMOS sensor, which demands both a fast-analog acquisition rate and a high channel count. The CMOS device has 32 analog outputs, and each output requires at

least a 1.3 MHz sampling rate from the ADC to effectively resolve all of the multiplexed data. The external clock sources required for the CMOS device are generated by the MCU.

### 3.5.1 Simultaneous 32-ch analog recordings at 1.3 MHz sampling rate per channel

For this test, 332 kHz analog test pulses are generated by the CMOS device and the amplitude of the analog pulses varies between 1 – 2 V. The ADCs are configured to operate at 1.3 MHz per channel and the 32 individual analog signals are successfully recorded in parallel using the 32 ADCs in the system (Figure 3.5). The USB 3.0 controller is set to operate with a 26 MHz peripheral clock (PCLK) which determines the digital sampling rate. Because each data package of the 32-bit USB controller is 4 bytes, the resulting transfer rate from the USB controller is ~10 MB/s. The data acquisition is stable for long-term continuous recordings and is mainly limited by the size of the computer's hard drive. With the 1.3 MHz per channel sampling rate, a one-minute recording results in a 6.24-Gbyte binary file.

### 3.5.2 Performance and noise characteristics

For this test, a 2-pole anti-aliasing filter with a cutoff frequency of 530 kHz is attached in the I/O interface of the data acquisition system to minimize aliasing noise. The system is tested with two different ADC sampling rates, 1.3 MHz, and 2.3 MHz, and a reference voltage is recorded using each sampling rate to analyze the performance and the noise characteristics. The recorded noise spectral densities (NSD) are shown in Figure 3.6. The measured noise densities are $1.01\times10^{-12}$ $V^2/Hz$ and $4.58 \times 10^{-12}$ $V^2/Hz$ for 1.3 MHz, and 2.3 MHz, respectively, which are suitable for the electrochemical imaging application.

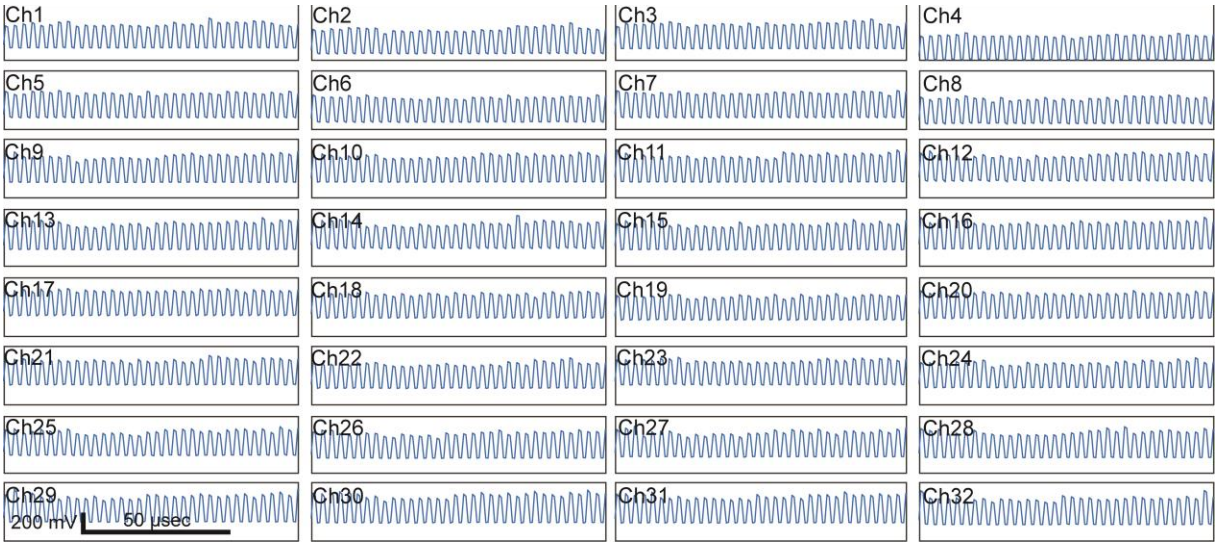


Figure 3.5. The parallel recording of 32-ch ADCs at 1.3 MHz sampling rate per channel using the data acquisition system. Each measurement shows individual column's output from the CMOS device. All 32 outputs contain time-division multiplexed signals from 1024 electrodes. Each square-wave period corresponds to the output of an individual electrode. © 2018 IEEE

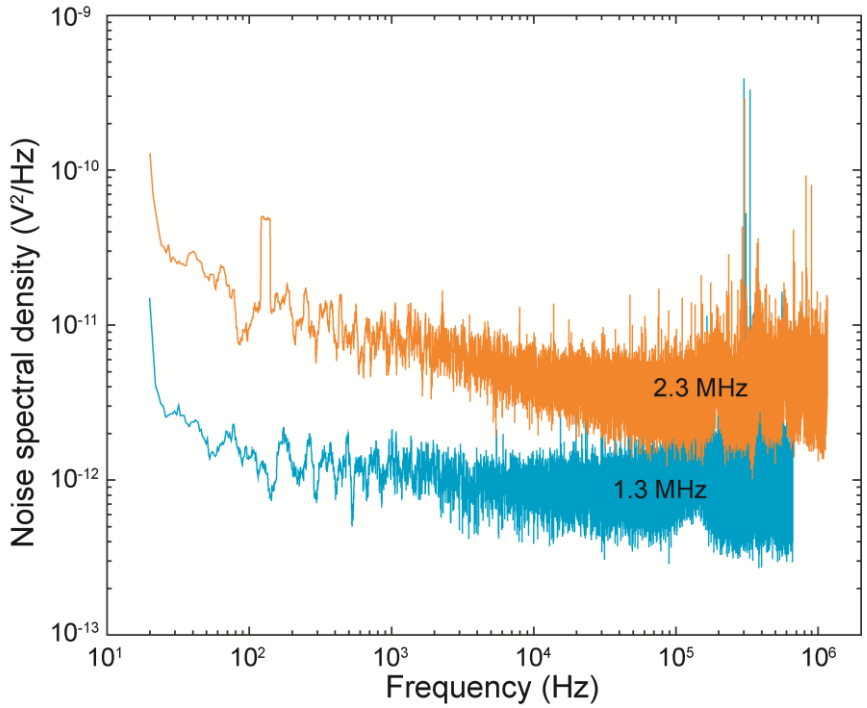


Figure 3.6. The NSD of the multifunctional data acquisition system at two different sampling rate settings: 1.3 MHz and 2.3 MHz. The measured average noise levels are $1.01 \times 10^{-12}$ $V^2/Hz$ and $4.58 \times 10^{-12}$ $V^2/Hz$ for each sampling rate. © 2018 IEEE

## 3.6 Electrochemical Imaging of Dopamine Diffusion

The setup for the electrochemical imaging is shown in Figure 3.7. The setup consists of the multifunctional data acquisition system, monolithic CMOS sensor, biasing board for the CMOS device, and a 3D-printed microscope mount for the system. Each CMOS-based electrochemical electrode measures the oxidation current at 10.38 kHz sampling rate, and thus, the parallel recording from the 1024 electrode array sums to a total sampling rate of 10.63 MHz sampling rate. Each ADC samples with four times redundancy, thus the total sampling rate of the multifunctional data acquisition system is 42.52 MHz. The electrochemical imaging is performed by measuring the oxidation of dopamine molecules at each electrode. For this experiment, the 3D-printed well is initially filled with 2 mL of phosphate buffered saline (PBS) and an Ag|AgCl reference electrode is inserted into the PBS solution. After the recording is started, 20 μL of 10-mM dopamine solution is injected into the well. This is expected to result in a 100-μM dopamine solution in the well by diffusion.

Electrodes located in the outer perimeter of the electrode array are covered by PDMS to deactivate their sensitivity to dopamine molecules (Figure 3.8a). These electrodes are used as a control in this experiment to monitor the stable operation of overall circuits and electronics. Although these PDMS-covered electrodes are insensitive to the dopamine injection, they are functional in terms of recording capability and data processing. Any activity recorded in these electrodes may indicate the electrostatic injection of electrons or malfunction of the underlying circuits. Thus, the control can be used to isolate dopamine responses from any artifacts exhibited in recordings from uncovered electrodes. Dopamine oxidation is successfully measured from the electrodes which are not covered by PDMS (Figure 3.8b). As configured by the multifunctional data acquisition system, a 2D electrochemical imaging of dopamine oxidation with over 10,000 frames per second is achieved (Figure 3.8b and c). As a large concentration of dopamine reaches the electrodes, a significant increase

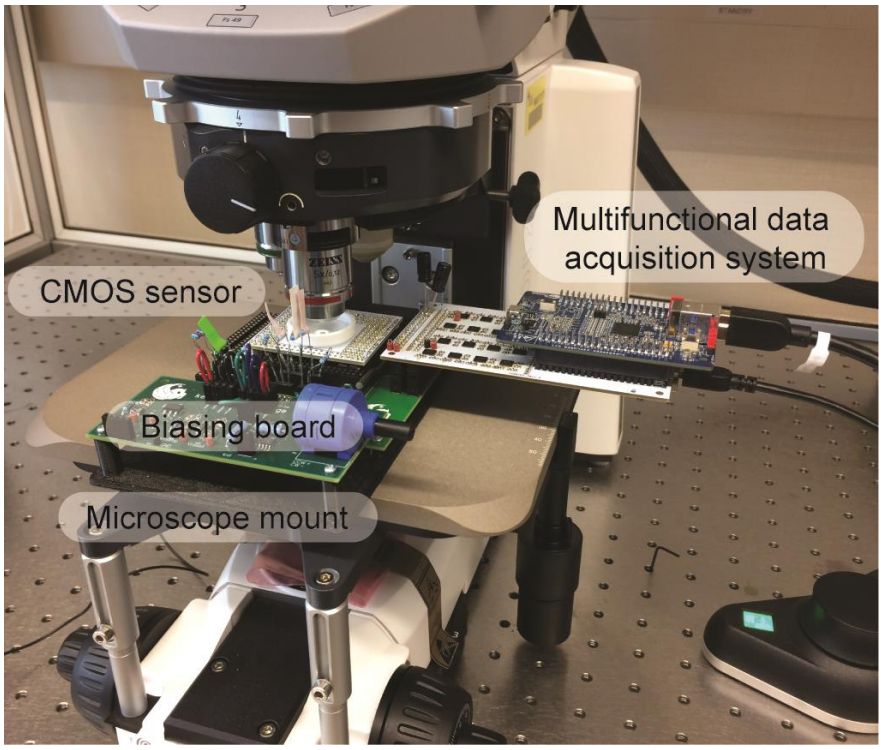


Figure 3.7. Electrochemical imaging setup consisting of multifunctional data acquisition system, monolithic CMOS sensor, biasing board for the CMOS device, and a 3D-printed microscope mount for the system. © 2018 IEEE

in oxidation current is observed. A set of 32 electrochemical measurements from 7th row from the bottom of the array is shown in Figure 3.8b. The visual inspection of the microphotograph in Figure 3.8a indicates that 16 electrodes (columns 1 – 8 and 25 – 32) are covered by PDMS and the remaining 16 electrodes (columns 9 – 24) are not affected by PDMS in the 7$^{th}$ row from the bottom. As expected, the 16 uncovered electrodes (columns 9 – 24) exhibited dopamine responses over 50 pA, while the rest show little or no response (< 35 pA) to the dopamine injection.

The spatial diffusion of dopamine is visualized by 2D plotting the recordings of individual electrodes. Contour plots with filled color are generated for each frame, which includes all 1024 electrodes' current responses at each time point. Overall, 380 electrodes have detected the dopamine influx with responses over 50 pA. For the 2D plotting, a normalization is performed for the dopamine-

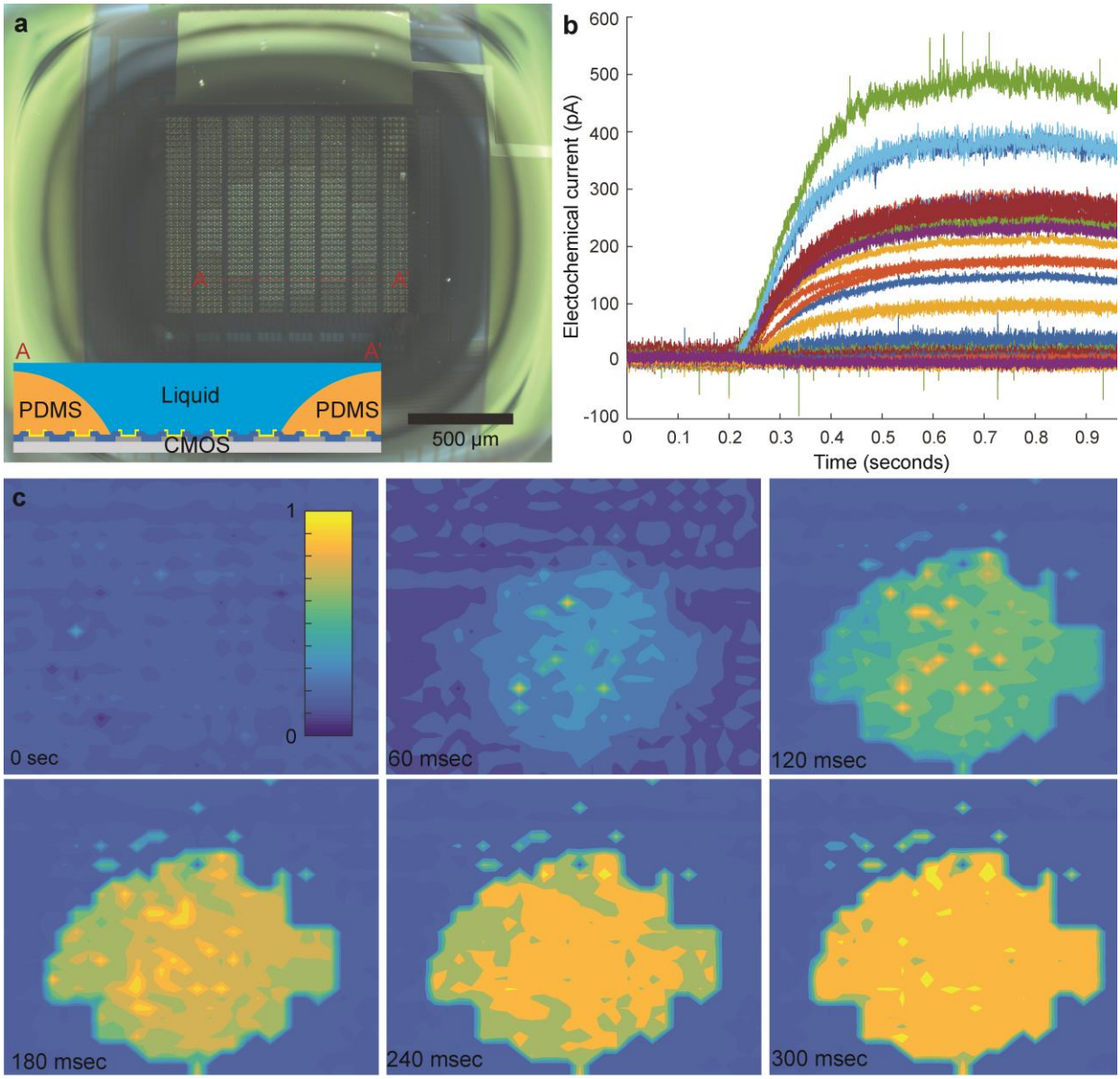


Figure 3.8. The electrochemical imaging using the monolithic CMOS imaging sensor and multifunctional data acquisition system. (a) The microphotograph of the monolithic sensor with PDMS. Electrodes on the perimeter of the 1024 array are covered with PDMS to impede the dopamine measurement on those electrodes so that they can used as a control. The electrodes toward the middle, which are brighter in color, are open for dopamine measurements. (b) Electrochemical recordings from the 7$^{th}$ row from the bottom of the array. Each color corresponds to a different column of the measured row. (c) Diffusion of dopamine throughout the array in a 300ms time frame is shown at six selected frames, at 60 ms intervals, out of the 3000 recorded frames. © 2018 IEEE

sensitive electrodes. Six frames, out of 3000 frames recorded for a 300-ms measurement, with a 60-ms interval are presented in Figure 3.8c. In the 0-ms frame, none of the electrodes in the array are

sensing the oxidation of dopamine. At the 60-ms frame, electrodes in the center of the array are starting to detect the oxidation current, indicating the increase in the dopamine concentration near the array due to the dopamine injection in the 3D-printed well. In the following frames (120-ms, 180-ms, and 240-ms), the level of detection sharply increases, and most of the electrodes reach a steady-state at 300 ms. The steady-state is due to the slow diffusion of dopamine toward the electrode array compared to the quick oxidative consumption of dopamine by the electrodes [43]. Thus, the oxidation current reaches a diffusion-limited steady-state.

## 3.7 Conclusion

In this paper, we present an electrochemical imaging platform that is comprised of a monolithic CMOS electrochemical sensor and a multifunctional data acquisition system that enables the system's high-throughput capability of over 10,000 frames per second. The multifunctional data acquisition system can potentially be used for other high-through applications with high versatility by reconfiguring the functions of most I/Os and the sampling rate of the ADCs.

## 3.8 Acknowledgment

The authors thank Edward Dein for his technical assistance in the clean room. Post-CMOS processing was carried out in Advanced Microfabrication Facility (AMPAC) at the University of Central Florida. Also, the authors thank the technical support team, Denise Tjon Ket Tjong, Steven Dick, and Derrick McQuern, in College of Engineering and Computer Science at University of Central Florida for their excellent support in maintaining the lab computers and file server used for this research project

# CHAPTER 4: A 512-CH DUAL-MODE MICROCHIP FOR SIMULTANEOUS MEASUREMENTS OF ELECTROPHYSIOLOGICAL AND NEUROCHEMICAL ACTIVITIES

## 4.1 Chapter Notes

Having demonstrated the concept of using a high-density and high-throughput on-chip MEA in our previous publications, our focused shifted to the concept presented in this paper. That is, the dual-mode concept. The goal is to produce an MEA chip that can simultaneously measure both modalities of signals from neurons. Our previously developed electrochemical chip is fully capable of measuring neurotransmitter release and flow across a large array, but it is incapable of measuring the more commonly studied action potential spikes. These spikes are a voltage domain signal and require a different amplifier topology than the TIA that is used in our previous designs. This design therefore required the development of a low-noise and high-performance voltage amplifier capable of integration at a similar scale with our previously developed TIA. Also presented in this paper is the evolution of our previously designed TIA that greatly increases the dynamic range and enables cyclic voltammetry. The resulting dual mode chip has a 512 electrode MEA and is capable of simultaneously measuring neurotransmitter release and action potential spikes at 40,000 kHz. This device has applications for neuroscientists being one of the first devices to allow measurement of the dynamic process of neurotransmission through both modalities and possibly the ability to discover a mechanism of the breakdown in neurotransmission that occurs in common neurodegenerative diseases such as Parkinson's or Alzheimer's diseases. This paper is co-authored by Kevin A. White and Brian N. Kim. At the time of writing, this paper in in the submission process for publication.

## 4.2 Introduction

The detailed study of synaptic function is of paramount importance for a better understanding of neurodegenerative diseases. Many diseases involving motor function, sensory, and cognitive impairments such as Parkinson's Disease, Huntington's Disease, and Alzheimer's Disease are speculated to be caused by dysfunction of the synapses [17]–[21]. Alzheimer's has been shown to develop in patients with an abnormal buildup and accumulation of amyloid-beta and tau oligomer proteins, which have been shown to harm the communication between synapses as well as neuronal loss [17], [70], [71]. Parkinson's and another neurodegenerative disease, Lewy Body Dementia, are thought to develop from a similar underlying process through the buildup of alpha-synuclein and/or tau oligomers [72]–[74]. This degradation in synaptic function is common to all of these neurodegenerative diseases and is even noticed in many preclinical cases, suggesting the need for early detection of degradation [20], [75], [76].

There are primarily two types of electrical measurement used when studying neuronal activity: electrophysiology and amperometry. Electrophysiology is a broader term but within the study of the brain, it generally refers to measurements of voltage, particularly the measurement of Action Potentials (AP) and local field potential (LFP). An AP is also known as a "spike" or a "nerve impulse" and is caused when a neuron "fires" and causes a depolarization and repolarization to travel along the neuron's axon. Amperometry involves the measurement of electrical current by fixing the potential of an electrode held near an active cell and measuring the current produced by the oxidation of neurotransmitters with a transimpedance amplifier (TIA). The process of secretion of neurotransmitters is known as exocytosis and is heavily studied using amperometry. Traditionally, researchers in a typical study perform either amperometry measurements or electrophysiology

measurements, seldom both simultaneously. Additionally, these measurements are typically low throughput, involving in many cases only single electrodes.

Recent developments in the field have begun to use CMOS technology to integrate large numbers of amplifiers and microelectrode arrays (MEA) onto a single chip for high throughput electrochemical measurements [43], [77]. Presently, there is no current technology that exists at the microscopic scales to measure both modes of electrical activity involved in neurotransmission. Without this dual-mode capability, it is difficult to accurately monitor the dynamics of neuronal degradation. Most current studies are relying on measurements using microelectrode arrays to measure action potentials as they travel along axons to synapses. However, when studying Parkinson's disease (PD), synapse disfunction has been seen to precede the common features of PD, such as complete synapse failure and neuronal loss, suggesting a need for the measurement of neurochemical activity when studying neurodegenerative diseases [78]–[81]. Furthermore, action potentials themselves are caused by secretions of neurotransmitters near the synapses of the neurons [82]–[84]. Thus, measuring action potentials alone, as is commonly done, is an indirect measurement which is not seeing the complete picture. If a complete understanding of the normal and dysfunctional neurotransmission is to be developed, a technology is needed that can measure neurotransmitter release and action potentials simultaneously and at a small enough scale to actually capture relevant information at a statistically significant quantity. The integrated circuit presented in this work is the first of its kind being presented to solve these problems.

Many CMOS chips have been presented that focus on providing a high-density MEA capable of performing electrophysiology [43], [85]–[88]. Unfortunately, since they are performing electrophysiology, typically using a transconductance amplifier (TCA), they are incapable of measuring neurotransmitter release. However, there has been at least one recently-reported high-density CMOS

MEA device that includes a small number of electrochemical amplifiers to measure neurotransmitter release in addition to typical electrophysiology measurements [33]. This device has a large number of electrodes (59,760), but can only measure from a selected portion of them (2048) at a time. Additionally, it only contains 28 amplifiers for measuring neurotransmitter release which have a noise performance on the order of 100s of $pA_{RMS}$. The low amplifier count and poor noise performance make this device incapable of measuring neurotransmitter release at a similar spatiotemporal resolution as its electrophysiology capability.

In this paper, we present a new dual-mode chip that expands on the commonly studied high-density CMOS MEA by treating neurochemical detectors with the same importance as electrophysiological detectors in an effort to provide a useful tool for the study of neurochemical effects in parallel with traditional electrophysiology effects so the interrelatedness can be better understood. The presented chip can simultaneously measure action potential propagations and neurochemical secretions at the synapses. Neurons can be measured using the dual-mode chip as demonstrated in Figure 4.1a, which shows a cross-sectional view of a pair of neurons sitting above the surface of the device. By integrating both neurochemical and action potential amplifiers onto a single chip, presynaptic action potentials, neurotransmitter release at the synapse, and postsynaptic action potentials can be observed simultaneously. If a large quantity of both modalities of amplifier are arranged into a large array, then the flow of action potentials and neurotransmitters across complex neuronal networks can be studied (Figure 4.1b). The dual-mode device presented in this paper is capable of measuring both neurotransmitter release and action potentials from 512 on-chip electrodes simultaneously and at the same spatiotemporal resolution. This device enables the study of the dynamic relationship between neurotransmission and action potential propagation using a single CMOS chip and MEA. Expanding on our previous work with high-density CMOS electrochemical

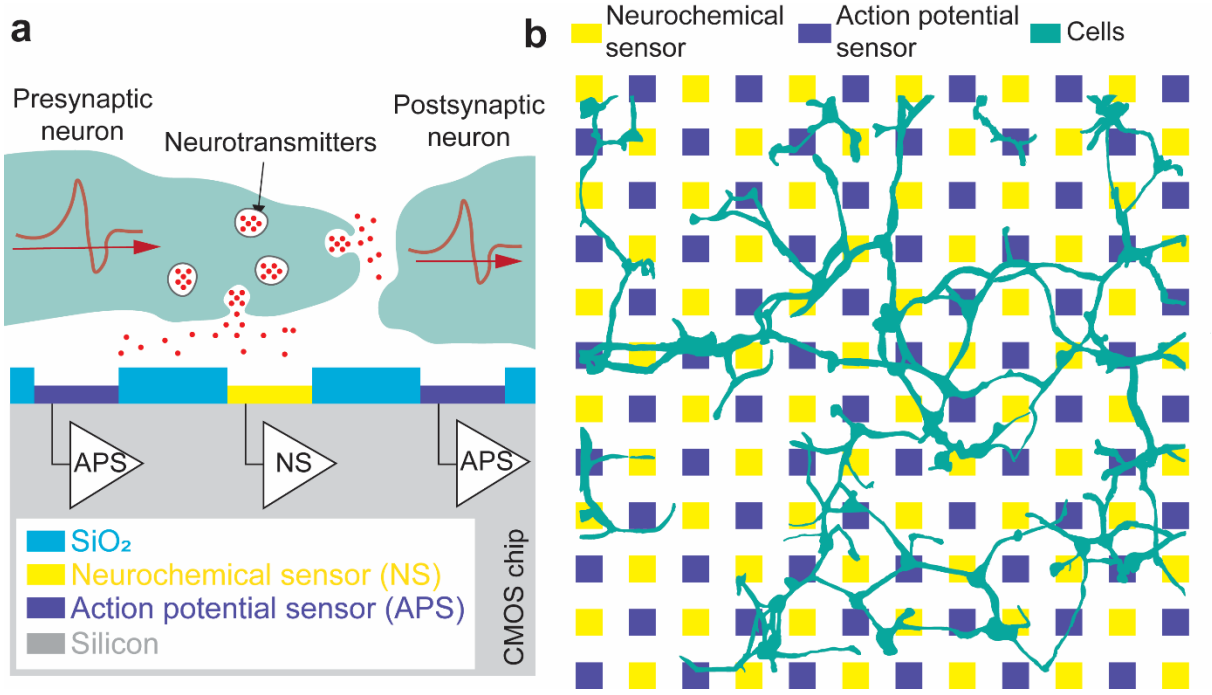


Figure 4.1. Conceptual view of the dual-mode device. (a) Cross-section showing simultaneous measurement of presynaptic action potential, neurotransmitter release at synapse, and postsynaptic action potential using dual-mode CMOS chip. (b) Top-down view showing large network of neurons located on the dual-mode microelectrode array.

MEAs [77], [89], we also add additional functionality to enable on-chip fast-scan cyclic voltammetry (FSCV). In section 4.3 we describe the overall concept and design of the dual-mode chip. Next, details of the circuitry used in the electrochemical amplifier as well as its performance will be discussed in section 4.4. The design and function of the electrophysiology amplifier are presented in section 4.5. In section 4.6, information about the dual-mode CMOS chip's layout and fabrication are provided. Finally, conclusions and discussions related to the dual-mode chip will be given in section 4.7.

## 4.3 Dual-Mode Chip Concept

The dual-mode concept is to simultaneously record neurotransmitter release and action potentials with a high electrode count, and high-density array. To create a large array of amplifiers, their design must be compact and scalable. This section describes simplified models of the

electrochemical and electrophysiology amplifiers used in the dual-mode chip to achieve the goals of measurement of both signal modalities while enabling a high electrode count without sacrificing performance. More detail about the actual amplifier designs used on the fabricated dual-mode chip as well as their measured performance will be provided in the subsequent sections.

### 4.3.1 System design

The dual-mode chip integrates three main functional blocks: a microelectrode array, 256 TIA neurochemical amplifiers, and 256 TCA electrophysiology amplifiers (Figure 4.2). Each and every electrode on the MEA is connected to its own dedicated amplifier. The approach of having dedicated amplifiers for each electrode has several benefits over multiplexed electrodes at the input of the amplifiers. The main benefit is that the bandwidth requirements of the amplifiers are greatly reduced. For example, if a hypothetical system were to be made using amplifiers each measuring 16 electrodes, then for the same per electrode sample rate, the required bandwidth of such an amplifier must be at least 16 times higher than a system using 16 separate amplifiers with much narrower bandwidth. The relatively small bandwidth needed for measuring neural signals is straightforward to obtain with smaller low power amplifiers. Additionally, good noise performance is much simpler to achieve in the lower bandwidth amplifiers than in amplifiers which must run at high speed. Using multiplexing, all 512

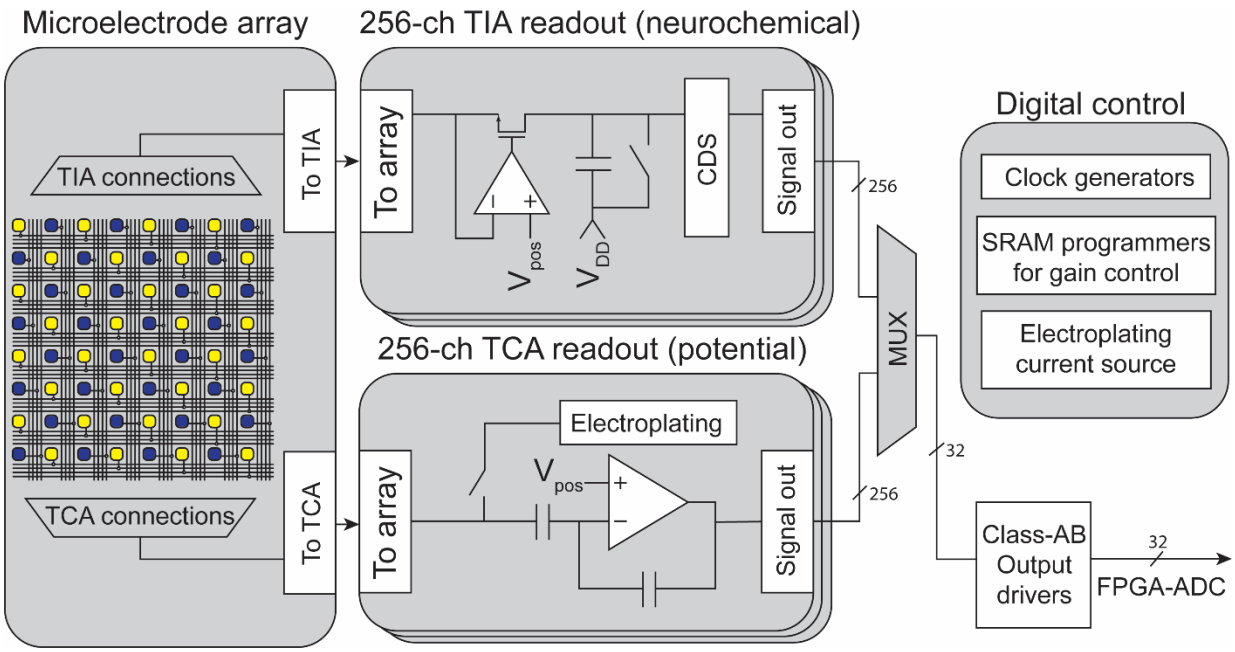


Figure 4.2. Block diagram of the dual-mode chip. Simultaneous measurement is enabled by multiplexing 256 parallel channels of neurochemical amplifiers and 256 parallel channels of electrophysiology amplifiers each of which is connected to its own electrode on a high-density microelectrode array. Additional on-chip circuitry controls the multiplexing, allows for electroplating of the electrodes, programs amplifier gain settings, and drives the off-chip ADCs.

amplifiers are fed to class AB output buffers for simultaneous parallel measurement using an off-chip data acquisition system [34]. The chip also contains additional circuitry for controlling the time-division multiplexing scheme, programming of SRAMs for gain control and testing modes, as well as on-chip current sources for electroplating of the electrodes with a suitable electrode material such as platinum black for potential measurements.

### 4.3.2 Fundamental transimpedance amplifier concept

The dual-mode chip's electrochemical amplifier is based on our half-shared TIA design (Figure 4.3a) [90]. This circuit converts electrode current by clamping the electrode voltage at a known level, $V_{pos}$, and integrating the current onto a capacitor. Before reaching $C_{int}$, the current must pass through the cascode transistor $M_2$ and the current mirror formed by $M_3$ and $M_4$. The current mirror is designed

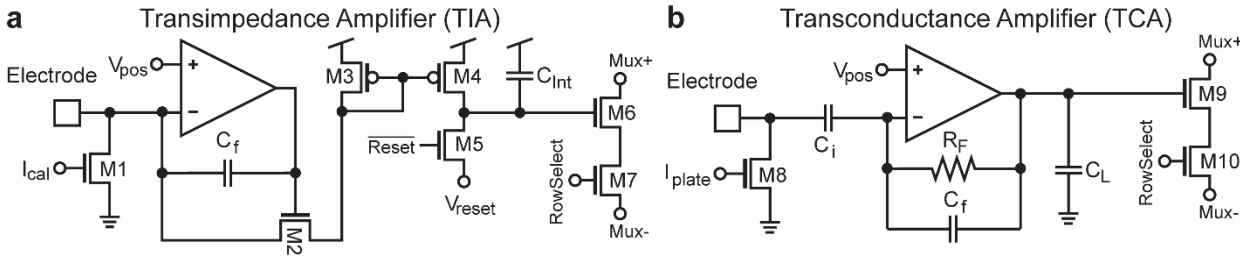


Figure 4.3. Simplified schematics of the TIA and TCA (a) The integrating TIA is based on a regulated cascode amplifier that integrates electrode current onto $C_{int}$ through the adjustable ratioed current mirror formed by $M_3$ and $M_4$ to enable different gain settings. (b) The TCA is a capacitive feedback design to measure electrode potential. The output current is passed to $C_L$ to produce a voltage. Both the TIA and TCA include output multiplexing circuitry and current mirrors on the electrodes to enable electroplating of suitable electrode materials such as gold, platinum black, or Ag/AgCl.

so that the W/L ratio of $M_3$ can be changed which causes more or less current to flow in $C_{int}$ for the same electrode current, thus providing multiple transimpedance gain settings. The transistor $M_4$ is part of a current mirror that serves two purposes. The first is to add an offset current to the measurement so that both oxidation and reduction currents can be measured by the amplifier while maintaining the same direction of current flowing through $M_2$ and $C_{int}$. The second is to enable accurate calibration of TIAs. A multiplexer ($M_6$ and $M_7$) is used to read out the integrated voltage. At the sample rate ($f_s$), the integration capacitor is reset using $M_5$ by discharging the capacitor to $V_{reset}$. The gain can be determined by the following expression:

$$Gain\ [A/V] = \frac{C_{int}}{t_{int} \times div} \tag{4.1}$$

where $C_{int}$ is the value of the integration capacitor, $t_{int}$ is the integration period ($1/f_s$) and *div* is the current mirror divider ratio. Because of the integration and sampling, the expected frequency response will correspond to the *sinc()* function [90].

### 4.3.3 Fundamental transconductance amplifier concept

The electrophysiology amplifier (Figure 4.3b) is based on a neural amplifier design that is commonly used with some simplifications [91]. It uses capacitors $C_i$ and $C_f$ to AC couple the electrode and to set the gain of the amplifier. Resistor $R_f$ is a high-value resistance to provide DC stability for the amplifier. The output of the TCA drives a load capacitor $C_L$ to produce an output voltage. Some important design equations for this amplifier are given below for the gain and bandwidth:

$$Gain\ [V/V] = \frac{C_i}{C_f} \tag{4.2}$$

$$BW \propto \frac{1}{Gain \cdot C_L} \tag{4.3}$$

Like the TIA, an output multiplexer ($M_9$ and $M_{10}$) and an electroplating current mirror ($M_8$) is included in the design.

## 4.4 Electrochemical Amplifier

The electrochemical amplifier that is used in the dual-mode chip builds on our previously published amplifier design which is one of the highest performing transimpedance amplifier arrays published [34], [77], [89], [90], [92]. For the dual-mode chip, the electrochemical amplifier can operate two modes of operation, amperometry and cyclic voltammetry. Cyclic voltammetry (CV) is a method to study neurotransmitters as well as other electroactive molecules. FSCV or fast-scan cyclic voltammetry can achieve higher temporal resolution and sensitivity compared to slow-scan CV [45], [93], [94]. We have been able to successfully perform traditional slow-scan CV using our previous device [92] however, to implement FSCV, a wide dynamic range and flexible gain settings are added to the dual-mode chip's electrochemical amplifiers. This section will describe the circuitry used in the

electrochemical amplifiers, how FSCV is implemented, and give some performance results from the fabricated device.

### 4.4.1 Amperometry mode

Amperometry mode for the electrochemical amplifier is implemented using a design that we have previously reported [34], [77], [89], [90], [92]. The portion of the schematic to the left of the dashed line in Figure 4.4a shows the reused elements of the electrochemical sensor. Briefly, this circuit is an integrating transimpedance amplifier comprised of a half-shared op-amp [90] with a cascode transistor $M_9$, where electrode current is integrated onto $C_{LoG}$, or onto the parasitic capacitance of the node at the drain of $M_9$, depending on the amperometry gain setting (changed by $M_8$ and LoG). The potential of the electrode is maintained at $V_{pos}$ due to the op-amp's feedback through the cascode transistor. The addition of $M_{10}$, $M_{12}$, and $M_{15}$ allows disconnection of the reset transistor $M_4$, disconnection of the output multiplexer circuitry, and connection to the additional FSCV mode circuitry to the right of the dashed line. More information on the multiplexing operation is presented in section 4.4.4.

### 4.4.2 Fast scan cyclic voltammetry mode

FSCV measurements require a wide dynamic range in the range of μA rather than pA to nA seen in amperometry, because of the large displacement current coming from the double-layer capacitance of the electrode-electrolyte interface. In the dual-mode chip, adjustable ratio current mirrors and a larger integration capacitor are included to provide a significantly higher dynamic range which corresponds to lower gain settings. These changes are shown in Figure 4.4a to the right of the dashed line. $M_{10}$ is added to enable switching to CV mode when $CV_{on}$ is set high. This disables the reset signal from resetting the capacitance at the drain node of $M_9$. $M_{12}$ is enabled when $CV_{on}$ is high, connecting the original circuit to the new additional CV mode circuity. Conceptually, $M_{19}$-$M_{22}$ form a

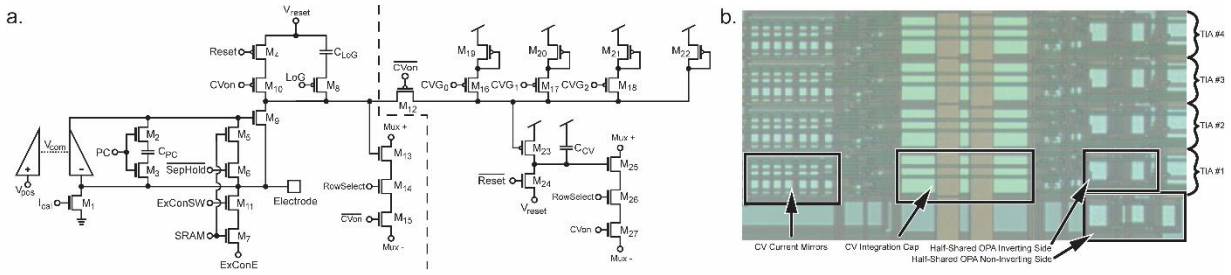


Figure 4.4. Details of the TIA's design. (a) Schematic of the TIA. To the left of the dashed line, the schematic is similar to our previously reported TIA design and is used for amperometry. The circuitry to the right of the dashed line implements FSCV functionality using the current mirrors formed by $M_{19}$-$M_{22}$ and $M_{23}$ with integration cap $C_{CV}$. Switches $M_{16}$-$M_{17}$ enable multiple gain settings for FSCV mode. (b) Image of a group of 4 half-shared TIAs on the fabricated chip. Four amplifiers share the non-inverting side of the OPA to conserve space. [90] The CV integration cap and CV current mirrors occupy a considerable die area.

ratioed current mirror with $M_{23}$ whose ratio is programmable by enabling or disabling the signals $CVG_0$-$CVG_2$. The current is then integrated onto the capacitor $C_{CV}$ which is reset by $M_{24}$. The output is sent to the output buffers through output mux transistors $M_{25}$-$M_{27}$. This configuration allows for the two original TIA's gain settings set by the parasitic capacitance at the drain node of $M_9$ or the integration capacitor $C_{LoG}$, as well as new lower gain settings for FSCV. With these current mirrors and larger integration capacitor, FSCV mode allows for gain settings in the range of ~0.48 to 1.6 V/μA which greatly extends the range into levels more suitable for FSCV, where signals typically have amplitudes in the range of a few microamperes. A photomicrograph of a group of four TIAs fabricated on-chip is shown in Figure 4.4b. Four amplifiers are shown to demonstrate the space-saving half-shared structure of the op-amps along the right side of the layout. The large $C_{CV}$ integration cap is seen in the middle of the layout. This capacitor would need to be made considerably larger to achieve the same gains if not for the next largest group of components, the current mirrors for FSCV mode, which can be seen on the left. The total size of an individual amplifier is 180.15 μm by 20.45 μm, or ~3070 $\mu m^2$.

### 4.4.3 Electrochemical amplifier performance

The transimpedance gain of individual TIAs can be directly measured by injecting known currents into the built-in $I_{cal}$ current mirrors ($M_1$) and plotting the difference in output voltage against the input currents. For amperometry mode, current was input ranging from 0 to 9 nanoamperes, resulting in a voltage difference ranging from 0 to ~1 volt (Figure 4.5a). The measurements of the entire collection of 256 amplifiers are plotted in blue with dots for the mean and error bars showing the standard deviation. A linear fit is performed to show the gain of the TIA (red line), resulting in a transimpedance gain of 144 mV/pA at a sample rate of 40 kHz. Notice that the gain tapers off at currents above ~7 nA, this is caused by limitations of the output buffers. Data points above this level are excluded from the linear fit.

The frequency domain characteristics of the TIA are also studied (Figure 4.5b and c). A frequency response was obtained by enabling the external electrode connection to an amplifier and injecting a small sine wave into the electrode through a resistor to produce a known AC current. In Figure 4.5b, the result of this measurement is shown. Blue points are the measurements at test frequencies ranging from 0.1 Hz to 30 kHz. The response of the integrating amplifier is known to correspond to a *sinc()* function [90], and by fitting to this response produces a cutoff frequency of ~10.3 kHz. A noise spectral density is presented in Figure 4.5c. Integrating under this curve yields a total noise of 4.51 $pA_{RMS}$.

For FSCV mode, there are five distinct gain settings. Each of these was measured in the same way as previously mentioned for amperometry mode. In Figure 4.5d these measurements are shown where each setting is plotted as its own colored points and fit line. The resulting gain settings range from ~0.48 to 1.6 V/μA when sampled at 40 kHz. To determine the matching characteristics of the

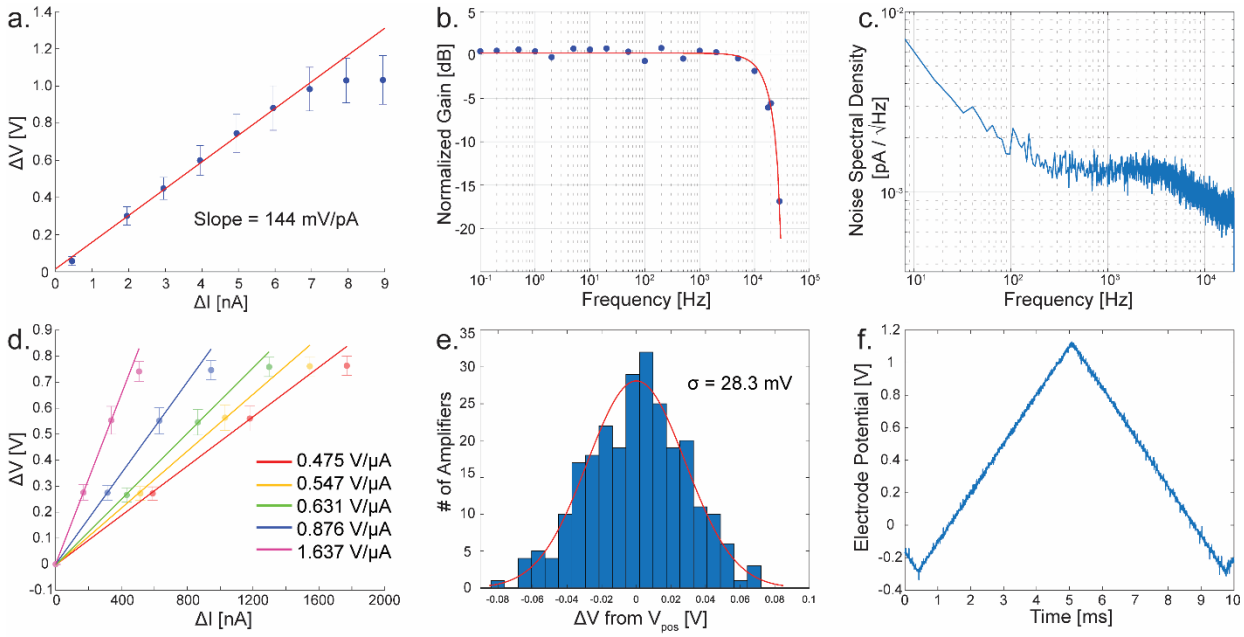


Figure 4.5. Measurements of the TIA with amperometry and FSCV modes. (a) Gain calibration in amperometry mode. (b) Frequency response at measured points (blue) with *sinc()* response best fit (red). (c) Noise spectral density of a typical TIA. (d) Gain calibration of the multiple FSCV gain settings. (e) Histogram showing the mismatch distribution between all 256 TIAs in FSCV mode. (f) Measured electrode potential of an amplifier in FSCV mode. The scan rate is 300 V/s.

current mirrors, $I_{cal}$ is grounded to ensure zero input current, and the resulting output voltage is subtracted from the $V_{pos}$ level, a histogram is plotted and shown in Figure 4.5e. By fitting the data of all 256 channels, the standard deviation of this mismatch is 28.3 mV. Because the measurements are calibrated to a zero current input (Figure 4.5d), the voltage mismatch between channels does not harm the performance of the amplifier until the mismatch becomes so great as to limit the dynamic range of the circuit. To implement FSCV, it is necessary to stimulate the electrode potential. Typically, this is performed using a triangular-shaped pulse with a ramp rate of 300 V/s with an amplitude range up to 1.7 V [45], [94]. To ensure that the amplifier is indeed capable of driving the electrode at such speeds, a triangle wave with a ramp rate of 300 V/s and amplitude of 1.4V was applied to $V_{pos}$ while the electrode potential was measured using ExConE. The result is shown in Figure 4.5f. The amplifier

Table 4.1: Comparison to Similar Transimpedance Amplifiers

| Reference | [95] | [33] | [96] | [43] | [88] | [87] | Dual-Mode TIA |
|---|---|---|---|---|---|---|---|
| **Process Node** | 0.5 μm | 0.18 μm | 0.5 μm | 0.5 μm | 0.13 μm | 0.18 μm | 0.35 μm |
| **Die Size** | - | 12 × 8.9 mm | 2.5 × 2.5 mm | 3 × 3 mm | 3 × 2 mm | 5 × 2.65 mm | 5 × 5 mm |
| **Electrodes** | 25 | 59760 | 100 | 100 | 1024 | 200 | 512 |
| **Amplifier Size** | 525 $\mu m^2$ | ≥0.04 $mm^2$ | 0.06 $mm^2$ | 900 $\mu m^2$ | 8000 $\mu m^2$ | 0.03 $mm^2$ | ~3070 $\mu m^2$ |
| **Parallel Channels** | 25 | 28 | 25 | 100 | 4 | 200 | 256 |
| **Noise** | ~ 110 $fA_{RMS}$ | 120 $pA_{RMS}$ | 7.2 $pA_{RMS}$ | ~ 100 $fA_{RMS}$ | 56 $pA_{RMS}$ | 480 $fA_{RMS}$ at 110 Hz filtered | 4.51 $pA_{RMS}$ |
| **Bandwidth** | 2 kHz | 16 kHz | 11.5 kHz | ~1 kHz | 700 Hz | 110 Hz - 10 kHz | 10.3 kHz |

shows no distortion of the triangular shape at these speeds and amplitude ranges. A comparison of the TIA to other reported designs is presented in Table 4.1. Compared to other designs, the TIAs presented in the dual-mode chip have one of the highest number or parallel channels versus the number of on-chip electrodes. Half of the MEA's electrodes are dedicated to the TIAs and each electrode is measured at the full sample rate, enabling a high spaciotemporal measurement from a large neuronal network.

### 4.4.4 Multiplexing

To facilitate the integration of hundreds of amplifiers onto a single chip the outputs of the amplifiers are multiplexed together. The multiplexing circuitry in the circuit consists of $M_6$-$M_7$ and $M_9$-$M_{10}$ (Figure 4.3), $M_{13}$-$M_{15}$ and $M_{25}$-$M_{27}$ (Figure 4.4a), and the circuit shown in Figure 4.6a. Focusing on the simplified schematics in Figure 4.3, the multiplexing circuit works by mirroring the gate voltage at $M_6$ or $M_9$ when the corresponding switch ($M_7$ or $M_{10}$ respectively) is turned on. In Figure 4.4a, the

schematic of the multiplexer circuit is shown. Here, $M_9$ and $M_{10}$ represent the $M_9$ and $M_{10}$ seen in Figure 4.3b. Assuming that the RowSelect signal on the gate of $M_{10}$ is high, current can flow from the node labeled MUX+ to MUX-. Effectively, a basic unity-gain op-amp structure is created with $M_1$-$M_5$ and $M_9$-$M_{10}$. The input pair is $M_3$ and $M_9$ where $M_3$ is the inverting input and $M_9$ is the noninverting input. Because the gate of $M_3$ is tied to the output, a unity gain is achieved. $M_4$ is included to balance the effect of $M_{10}$ (or any $M_k$.) A different amplifier can be selected for readout by any number of $M_j$ and $M_k$ devices, in the dual-mode chip there are 16 of these shared in each output multiplexer. In the electrochemical amplifiers there are two possible output nodes depending on the mode of operation (amperometry or FSCV mode.) The corresponding switch is turned on ($M_{15}$ or $M_{27}$ from Figure 4.4a.) to select the desired mode. In the multiplexers, the schematic is identical to that shown in Figure 4.6a except for an additional $M_4$ device to balance the effect of the additional CV mode switches ($M_{15}$ and $M_{27}$.) For the neurochemical amplifiers, the outputs are also passed through correlated double sampling circuitry (CDS.) In this design, 16 amplifiers are multiplexed together. The resulting output waveforms are shown in Figure 4.6. The multiplexing is digitally controlled using on-chip circuitry. One of the important signals is TimingD, which is shown in Figure 4.6a. This signal has a period of 40 kHz (equivalent to the sample rate.) When TimingD goes low, the multiplexing logic is reset, so that the readout of the 16 amplifiers returns to the first amplifier. Output waveforms are shown in Figure 4.6b and c. The y-axis is the voltage difference between $V_{clamp}$ and the amount of voltage integrated on the capacitor. In Figure 4.6b, the amplifier is in FSCV mode, so the amount of charge on the capacitor is subtracted from $V_{clamp}$. The output is sampled at the points shown by the red dots. This point is centered on the negative pulse produced by the CDS and is sampled at a rate that is 16× faster than the sample rate (640 kHz for a 40 kHz sample rate.) In Figure 4.6c, the amplifier is in amperometry mode, and therefore the amount of charge on the capacitor is added to $V_{clamp}$.

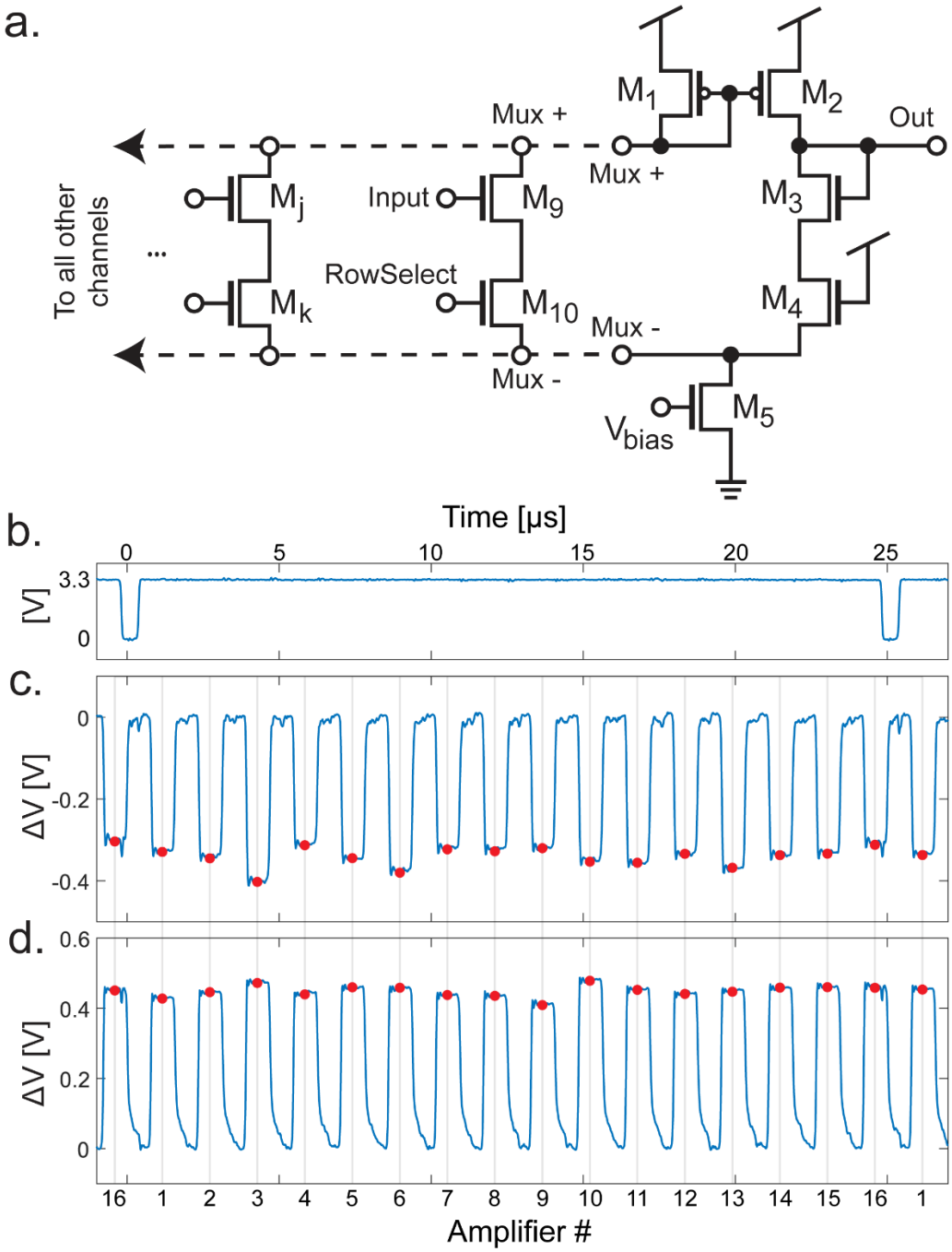


Figure 4.6. Detail of multiplexing scheme. (a) Schematic of the multiplexer circuit (b) The TimingD signal, resetting of the multiplexers during the low period. (c) Signal from output buffer in FSCV mode. The red dots are the points where the output is sampled. (d) In amperometry mode, the polarity is reversed, and the signal is sampled on the peaks of the output waveform.

In this case, although the samples happen at the same time with respect to the TimingD pulse, the samples are now on the positive side of the output pulse.

## 4.5 Electrophysiology Amplifier

In order to create a dense amplifier array, the design and performance of an electrophysiology amplifier must be compact while still providing low noise and high performance to be effective at measuring neuronal signals. In on-CMOS electrophysiology, measurement of action potential and local field potentials is often achieved using transconductance amplifiers which are usually based on a design originally published in [91]. This design also provides the basis for the electrophysiology amplifier used in the dual-mode chip. This section will describe the circuit design and modifications to the common design, as well as the performance of amplifiers on the fabricated dual-mode chip.

### 4.5.1 Transconductance amplifier design

The circuit used in the dual-mode chip to implement the TCA is based on a design widely used [91], however, miniaturization has been made to facilitate high-density integration and scalability. The circuit topology of the miniaturized TCA design is shown in Figure 4.7. Unlike the common design, the noninverting feedback capacitors are removed to greatly reduce the required die area consumption. To allow this modification, the noninverting input of the TCA is tied to a stable reference voltage known as $V_{pos}$. The TCA stabilizes its inverting input by negative feedback through $R_F$, which is implemented as a MOS-bipolar pseudoresistor (Figure 4.7a). Perturbations in the voltage at the electrode are amplified by the TCA at a ratio defined by the ratio of $C_i/C_f$, including the parasitic capacitance. The TCA's output current is converted to voltage by feeding the output to the load capacitance $C_L$ which is implemented as a MOS capacitor ($M_L$) to further minimize the required die area (Figure 4.7b). Some ancillary circuitry is also contained in each TCA for the output multiplexing and electroplating of the electrode surface. $M_{plate}$ forms half of a current mirror which enables

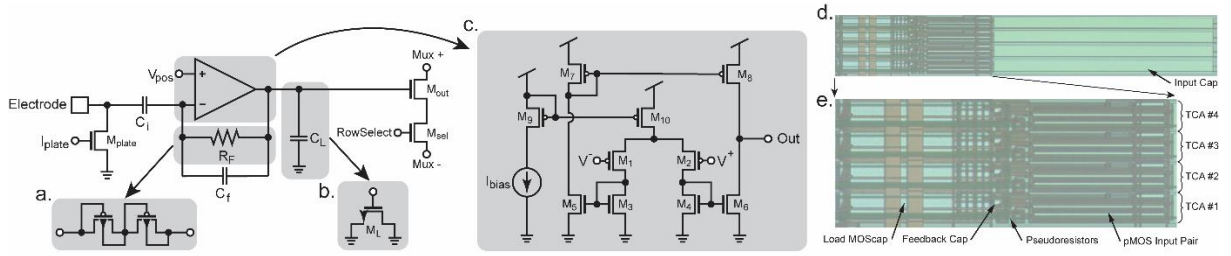


Figure 4.7. Details of the TCA's design. The TCA uses capacitive feedback providing a gain of roughly $C_i/C_f$. (a) DC stability is provided by a pseudoresistor $R_F$ which is implemented as a pair of diode-connected pMOS devices to conserve die area. (b) The load capacitor $C_L$ is implemented as a MOScap for compactness. (c) The internal schematic of the multiple current mirror TCA. (d) Layout image of a group of four TCAs as fabricated. The input capacitors consume ~60% of the die area. (e) Zoomed-in image of the active area of the TCAs. The largest components are the pMOS input devices $M_1$ and $M_2$ to minimize their noise contribution. The MOScap $C_L$ also consumes a significant area. Comparatively, the feedback cap $C_f$ and the pseudoresistors $R_F$ are relatively small.

electroplating when current is forced into $I_{plate}$ and the global current mirror transistor. $M_{out}$ acts as an output buffer when RowSelect is high and the switch $M_{sel}$ is activated similarly to what is described in section 4.4.4. This allows for a current path to flow between Mux+ and Mux– which are connected to the output multiplexer.

The TCA design is scaled down dramatically and adapted for the 0.35 μm process while maintaining the ideal operating regimes of the transistors (Figure 4.7c) [97]. The capacitors dominate area consumption even more than the transistors. Careful consideration was taken to reduce the needed area while still yielding an effective gain, bandwidth, and noise performance of the TCA. Overall, the reduction in die area using these optimizations results in dimensions of 541.9 × 20.45 μm and a total area of 0.011 $mm^2$ per amplifier which is one of the smallest reported to date. A photomicrograph of a group of fabricated TCAs is shown in Figure 4.7d. Most of the area, approximately 60%, is consumed by the ~10 pF input capacitor, emphasizing the importance of capacitor dimension optimization. Because of the large size of the input capacitor (Figure 4.7e) is also presented, which shows only the active area of the TCAs. The large input pair, $M_1$ and $M_2$ can be seen

with their extreme $W/L$ ratio enabling their operation in moderate-to-weak inversion for better noise performance. The load capacitor $C_L$ is the next largest component in terms of die area. Also shown are the relatively small pseudoresistors and feedback capacitor. All other components consume negligible area compared to those already mentioned.

### 4.5.2 Transconductance amplifier performance

The gain and bandwidth of each TCA are obtained by injecting a small sine wave into the ExConE connection (Figure 4.4a $M_7$ and $M_{11}$ and similar in the TCA). A signal is generated using a National Instruments USB-6363 interface while the the output amplitude is recorded using the FPGA-based data acqusition system. The response of a typical amplifier is presented in Figure 4.8a. The passband gain is 37.5 dB, about 75 V/V. The bandwidth is from ~0.2 Hz to ~10 kHz which is sufficient to measure signals in both the local field potential (LFP) band (<300Hz) and in the action potential (AP) band (300 Hz - 7.5 kHz) [98], [99]. Since APs are very low amplitude signals, the noise performance of the amplifier must be low. Figure 4.8b shows a measured noise spectral density of a TCA. Integrating this noise in the AP band yields an input-referred noise of 24.9 $\mu V_{RMS}$. To show the transient performance of the TCA, a measurement of a synthetic neural spike is performed at two different amplitudes (~1 mV and 4 mV, peak-to-peak). The spikes are generated using a common scheme [100] and fed into the amplifier. Figure 4.8c shows the resulting signal of a synthetic neural spike with a peak-to-peak amplitude of ~1mV. The signal is also shown filtered to the AP band, and a closer view of a single spike is also shown. Similarly, another measurement was performed with spikes of ~4 mV amplitude (Figure 4.8d). These measurements show that neural spikes of approximately 1mV or more are easily discerned from the random spikes occurring in the noise, and the amplifiers would therefore be capable of measuring actual spikes from live neurons in an *in-vitro* experiment, but the noise performance must be improved for future designs indended for *in-vivo*

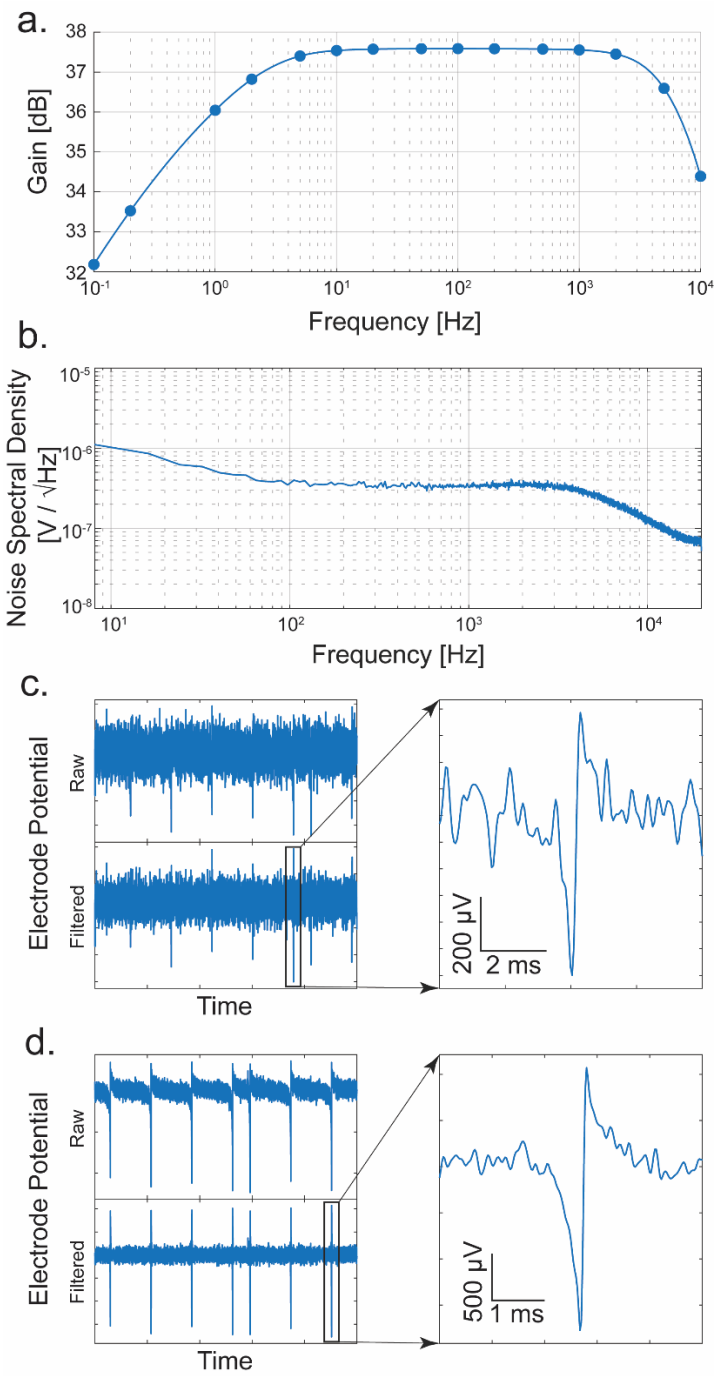


Figure 4.8. Performance of the TCA. (a) Frequency response of a typical amplifier. (b) Noise spectral density of a typical amplifier. (c) On-chip measurement of a synthesized neural spike of ~1mV amplitude. The raw and filtered from 300 to 7000 Hz are shown, as well as a close-up of a selected spike. (d) Measurement of a ~4mV amplitude synthetic neural spike.

measurements where action potentials are typically smaller in amplitude. Table 4.2 is shown to compare the TCA's performance with other presented designs.

## 4.6 CMOS Implementation

The dual-mode CMOS chip is designed and fabricated using a typical 0.35 μm 4 metal 2 poly N-well CMOS process. For this initial concept device, a die size of 5×5 mm is used (Figure 4.9), resulting in 512 fully parallel channels, with 256 dedicated to electrochemical measurements and 256 to electrophysiology measurements. The total power consumed by the dual-mode chip by all 512 amplifiers, multiplexers, and output buffers is 11.5 mW. This section describes considerations made in the layout of the device, as well as details of the on-chip microelectrode array.

Table 4.2: Comparison to Similar Transconductance Amplifiers

| Reference | [91] | [33] | [88] | [101] | [102] | Dual Mode TCA |
|---|---|---|---|---|---|---|
| **Noise** | 2.2 μVrms | 5.4 μVrms | 7.7 μVrms | 2.2 μVrms | 6.4 μVrms | 24.9 μVrms |
| **Sample Rate** | - | 20 kHz | - | 25 kHz | 30 kHz | 40 kHz |
| **Bandwidth** | 7.5 kHz | 300 Hz - 10 kHz | 300 Hz - 6 kHz | 300 Hz -10 kHz | 10 kHz | 0.2 Hz - 10kHz |
| **Size (per amplifier)** | 0.16 $mm^2$ | - | - | 0.07 $mm^2$ | - | 0.011 $mm^2$ |
| **Process Node** | 1.5 μm | 0.18 μm | 0.13 μm | 0.35 μm | 0.13 μm | 0.35 μm |
| **Voltage** | 5 V | - | - | - | 1.8 V | 3.3 V |
| **Current** | 8 μA | - | 2.5-37.5 μA | - | - | 8 μA |
| **Power** | 40 μW | 16 μW | - | 30 μW | 49.1 μW | 26 μW |
| **Parallel Channels** | 6 | 2048 | 1024 | 36 | 384 | 256 |
| **Electrodes** | - | 59760 | 1024 | 36 | 966 | 512 |
| **Electrode Pitch** | - | 13.5 μm | 58 μm | 25 μm | ~70 μm | 16 μm |
| **Die Size** | 2.2 × 2.2 mm | 12 × 8.9 mm | 3 × 1.85 mm | - | 9 × 5 mm | 5 × 5 mm |

### 4.6.1 Chip layout

The microelectrode array is placed at the center of the die (Figure 4.9a). In Figure 4.9b an annotated view of the layout's active area is shown. Wiring from the electrodes fans out to both sides of the array to connect to the amplifiers. On the left and right sides of the MEA, the amplifiers, digital circuitry, output multiplexing, output buffers, and biasing circuitry are mirrored. This arrangement gives a compact use of space and simplifies the electrode interconnection wiring. The dual-mode chip is designed to be interfaced with a custom-designed data acquisition system, so the 512 amplifier channels are multiplexed into 32 output channels [34]. To accomplish this, the outputs are grouped into 16 current channels and 16 voltage channels. These are then split into 8 and 8 on each side of the chip. Thus, each dedicated output serves groups of 16 amplifiers. In the close-up section of Figure 4.9c, this grouping of 16 amplifiers can be seen. Each of these groups of 16 contains 16 TIAs, 16 TCAs, and 2 output buffers. They are multiplexed together using digital control circuitry and the signals are buffered by the output buffers which are then connected to wire bonding pads to drive the off-chip ADCs. Within the group of 16 amplifiers, the TIAs are grouped in groups of 4 for half sharing. This is clearly seen in both Figure 4.9c and Figure 4.9b with the gaps between the groups of 4 amplifiers. For future designs, further space optimization could be obtained, for example, by rearranging the TCA input capacitors to use this empty space. For this initial design, this was not done to simplify the layout and ensure that all amplifiers are as identical as possible to minimize any potential peculiarities caused by nonidentical layout.

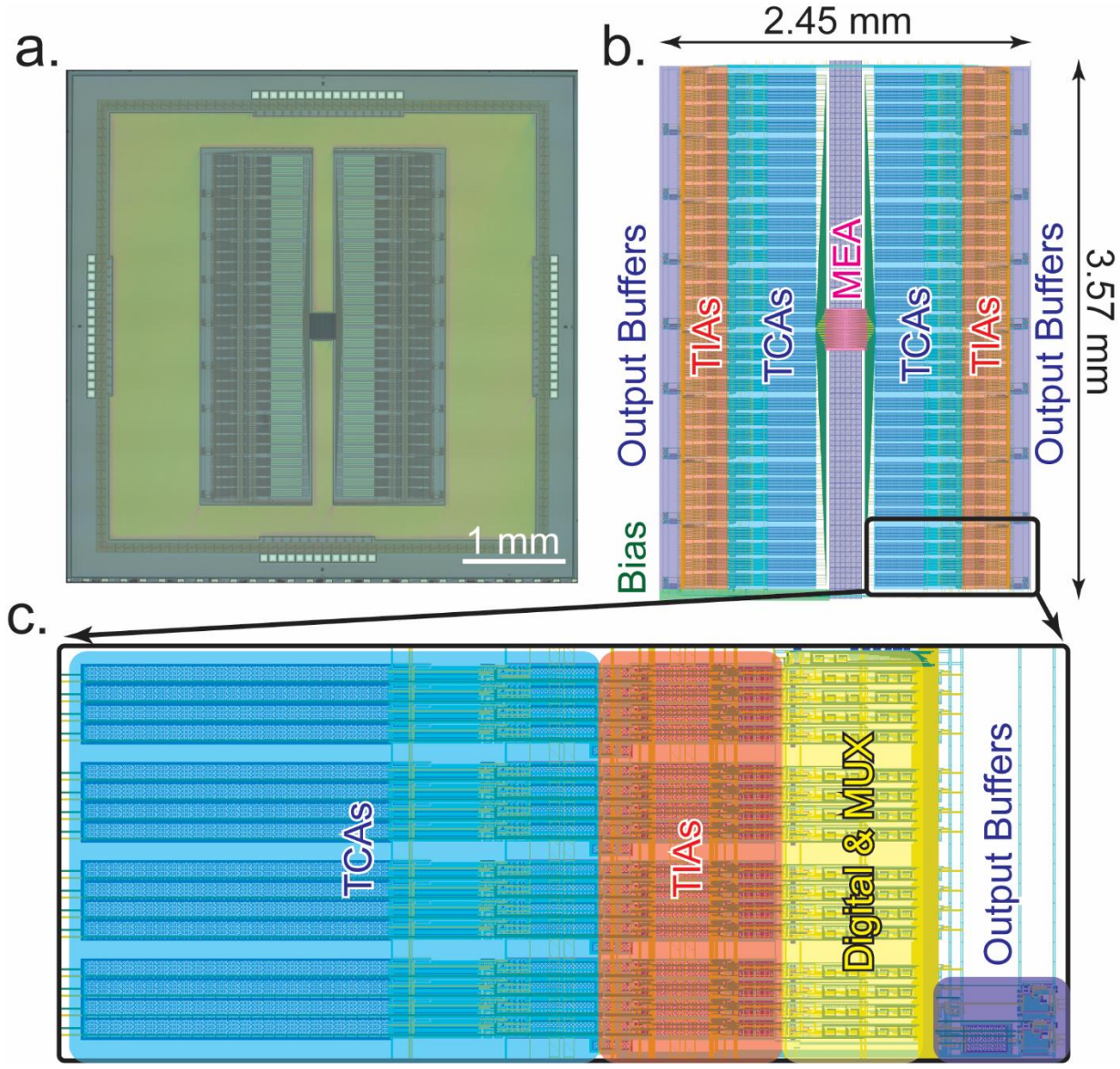


Figure 4.9. Layout information of the dual-mode chip. (a) Photomicrograph of the fabricated dual-mode chip using 0.35 μm CMOS technology. The total size is 5×5 mm. (b) Location of various structures on the chip. Amplifiers are mirrored on both sides of the centrally located microelectrode array. The active area is 2.45×3.57mm. (c) Close-up view of a "pseudocolumn" showing how each group of 16 amplifiers is arranged to enable multiplexing into a single output buffer.

### 4.6.2 Microelectrode array

The microelectrode array is a critical part of the dual-mode chip since it is the source of the signals that we are aiming to measure. It must have a high enough spatial resolution to resolve fine details between neurons. To determine a reasonable pitch, we examined other literature and chose a

value on a similar scale. In other MEAs some typical ranges are from 13.5 μm [33], 18 μm [103], to 42 μm [86] and even wider. For this design, the value was chosen to be 16 μm between electrodes. This value was chosen to stay closer to the smallest pitch reported in the literature, while giving sufficient space for the routing of the wiring out from the electrodes to the amplifiers as well as potential post processing that my take place. The resulting electrode array is shown in Figure 4.10. In Figure 4.10a, the layout is shown. The routing of the wiring fanning out from the center to the left and right sides, where they run out to connect to the amplifiers. The overall size of the MEA is 255.4 μm on each side. A closer view is shown in Figure 4.10b. The opening in the top glass passivation layer is 5 μm which is seen as an orange-colored square in the opening. This is the exposed area of AlCu where signals will enter the chip. Between similar mode electrodes, the spacing is 16 μm and between differing mode electrodes, the pitch is 8 μm. The array is effectively two separate arrays with a pitch of 16 μm between adjacent electrodes. One for the voltage channels and one for the current channels. Each array is interdigitated at an 8 μm pitch to produce a checkerboard pattern that can be seen in Figure 4.10c. Finally, a fabricated MEA is shown in Figure 4.10d. The density of the MEA is close to the limit of what can practically be fabricated in 0.35 μm technology without deliberately violating design rules which would potentially result in shorted electrodes or non-exposed electrodes on the chip's surface. For effectiveness in practical measurements, the electroplating circuitry within the amplifiers can be used to deposit a suitable and biocompatible electrode surface such as gold, platinum black, or Ag/AgCl. Additionally, our previously reported post-CMOS processing can be performed to create high quality electrodes and interelectrode isolation by the metal deposition and lift-off technique [35].

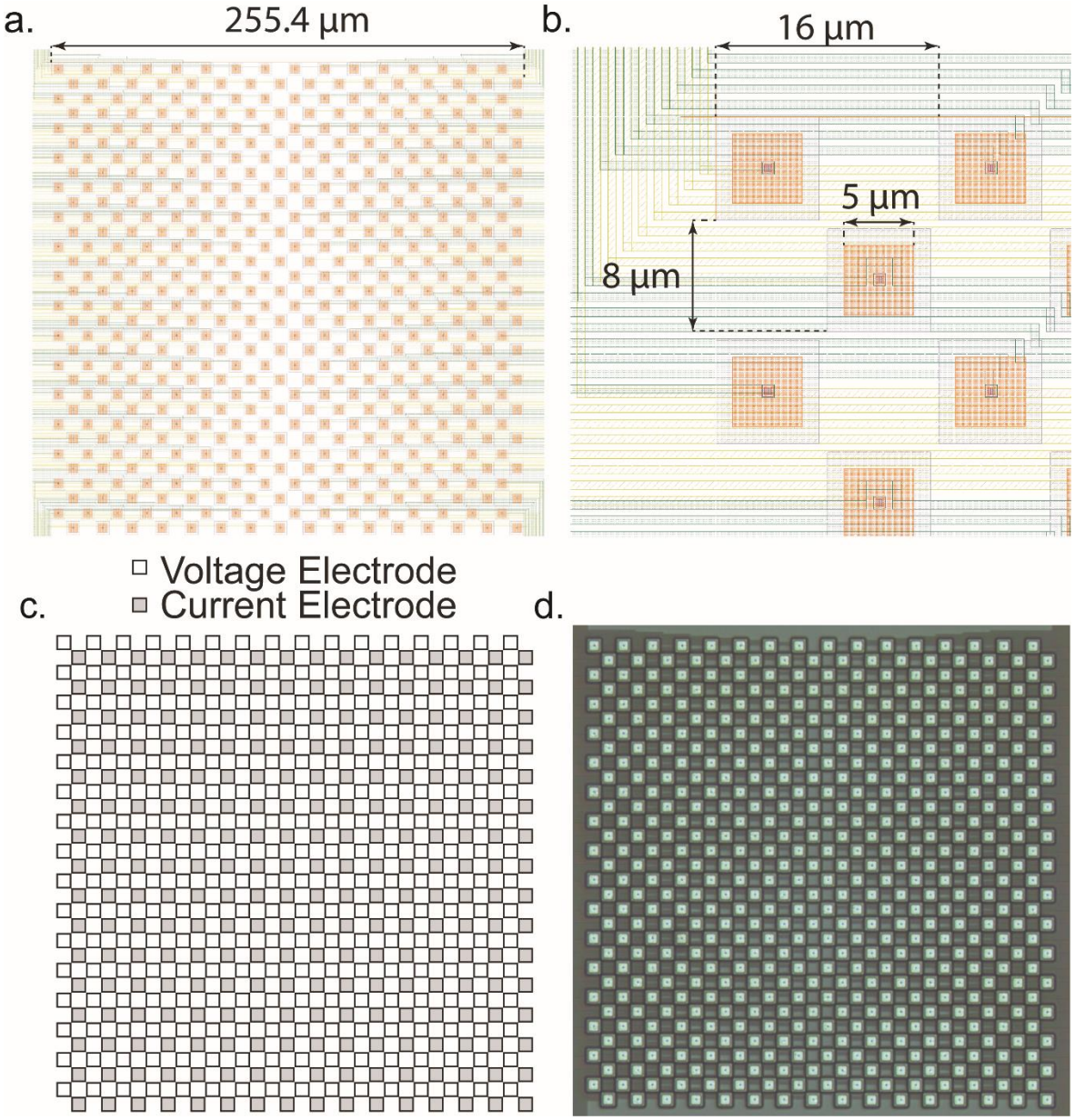


Figure 4.10. Design of the microelectrode array. (a) Layout image of the MEA. The MEA is 512 electrodes with 256 dedicated to voltage measurement and 256 dedicated to current measurement. The total size is ~250×250 µm. (b) Detail of the individual electrodes. The pitch between electrodes is 16 µm, the glass opening is 5 µm, and between rows the pitch is 8 µm. Each row is staggered, forming the checkerboard pattern. The yellow and green layers are the metal interconnects that connect the electrodes to the amplifiers. (c) Arrangement of the voltage and current electrodes. Each row serves a different modality amplifier. (d) Photomicrograph of the MEA as fabricated on-chip.

## 4.7 Conclusion and Discussion

We present a CMOS chip that is capable of a fully parallel and simultaneous measurement of 512 channels from an on-chip microelectrode array with 256 neurochemical and 256 electrophysiology amplifiers. Since the amplifiers are compact and scalable, a larger array with 1000s of amplifiers could easily be integrated into a chip that would fit within a commonly used silicon reticle. This proof-of-concept design fits 512 amplifiers and an electrode array into a total active area of only 2.45×3.57mm. This dual-mode technology allows the simultaneous study of the interactions between neurotransmission, synaptic function, and action potential propagation. As a tool, this technology could provide a means for neuroscientists to study the mechanisms of neuronal degradation and synaptic dysfunction seen in cases of many neurodegenerative disorders.

For future implementations, an increase in electrode count would be desired to enable measurements of larger physical areas. Additionally, a potential improvement to this design applies specifically to the design of MEA itself. The soma of a neuron is roughly equivalent in size to our MEA's electrode pitch, but a neuron will typically have multiple dendrites for receiving neurotransmitters from presynaptic neurons. This fact would suggest that if a more complete analysis of the interactions between neurotransmission and action potentials is desired, then an optimal MEA would have more neurochemical electrodes than electrophysiology electrodes. However, the dual-mode device in its current form is still the first device reported that is capable of measuring neurochemical signals at a similar spatial resolution as action potentials, and the design of a dual-mode chip with an improved MEA would be simple as the amplifier designs are compact and scalable.

# CHAPTER 5: 3D PRINTING AND MILLING A REAL-TIME PCR DEVICE FOR INFECTIOUS DISEASE DIAGNOSTICS

## 5.1 Chapter Notes

Shifting focus to the medical diagnostics area, this paper is included which presents the design and development of a portable and easily manufactured PCR device for the detection of viral infections. PCR is a technique that produces a large quantity of copies of a specific DNA sequence. It can be used for medical diagnostics by designing a probe containing a sequence that is only found in a particular virus and then amplifying that sequence from a sample. If that sequence is present in a patient's sample, it can be amplified and detected by the PCR. By adding fluorescent dyes to the probe, one is able to observe the amplification of the target as the PCR is running. The device presented in this paper accomplishes this using a microcontroller to control a custom-made heating element, fan, and optical system consisting of an LED and photodiode with amplifier. The structure of the device is created with 3D printed pieces, and the electronic components are readily available off-the-shelf parts. The design and 3D files are published along with the paper in an open-source fashion so others can build their own PCR device. Since the COVID-19 outbreak brought PCR to the general public's attention, this paper has received public attention and has been cited 31 times at the time of this writing. It was also selected to be included in the Diagnostic Tests in Low-Resource Settings curated collection[*]. The open-source design files for the 3D printed PCR machine can be found on the PLoS ONE webpage for the paper [24]. This paper was published in PLoS ONE and was co-authored by Kevin A. White, Manjusha Vaidya, Kiminobu Sugaya, Brian N. Kim[†].

[*] https://collections.plos.org/collection/diagnostic-tests-low-resource/

[†] This chapter uses previously published material from PLoS ONE, 2017 [24].

## 5.2 Introduction

Early diagnosis and prompt treatment is crucial to provide the best health care to a patient and to reduce the risk of further spreading, especially in cases involving malaria parasites, tuberculosis (TB), and human immunodeficiency virus (HIV). For this reason, many different techniques have been introduced and developed under the category, rapid diagnostics tests (RDT). The RDT offers low manufacturing cost and provides the first-level screening to determine the necessity of follow-up tests. A typical tradeoff from the RDT methods is accuracy and lack of quantification to obtain low-cost and ease of use. For example, the RDT devices for malaria detection, measures specific antigens, such as Histidine Rich Protein II, pLDH, and pAldo, produced from malaria parasites [104]. The antigen-based detection device typically has nonspecific bindings that produce false positive results, and yields low accuracy. Also, most antigen-based devices require a relatively high-level of pathogens in the patient sample compared to Polymerase Chain Reaction (PCR) to be detected as a positive result. The World Health Organization (WHO) recommends at least a 75% panel detection score, the detection success rate for low parasite density samples (200 parasites/μL), and a false positive rate of less than 10% [105]. Even for the commercially-available RDT devices that satisfy these criteria, the panel detection score is marginally higher than the recommended score, and false positive results exist. For HIV RDTs, antibodies for HIV-1 and HIV-2 are often measured, and a strategy to combine the detection of HIV-1/2 is recommended. Over the last generations of HIV RDT, the HIV antigen detection is incorporated with the antibody detection in attempt to detect the HIV infection in an early phase [106]. However, it lacks quantitative result and only outputs positive or negative. For acute HIV infection (AHI), an early HIV infection, most antigen- and antibody-based RDT fail to report the infection because the antigen and antibody biomarkers are not present in that phase [106]. The

only diagnosis mechanism that can measure the presence of HIV infection is nucleic acid-based and detects the presence of HIV RNA [107].

According to the Centers for Disease Control and Prevention (CDC) and WHO, for diseases such as Malaria and HIV, the use of PCR is highly recommended to obtain results and to determine the proper treatment [107], [108], because PCR reveals both the presence and the quantity of the pathogen and have high sensitivity and specificity. However, alternative techniques such as RDT are often used to make a diagnosis because of the more accessible nature of those techniques. The quantitative PCR (qPCR) is a robust technique that amplifies the target DNA sequence, while monitoring the amplitude of signal originating from DNA-intercalating probes, typically fluorescence, to quantify the amount of DNA being amplified [109], [110]. With custom-designed primers, PCR can be designed to amplify a specific sequence of DNA, providing high specificity in diagnostics. This is useful in differentiating various strains of malarial infection to coordinate proper treatment. The characteristic of the fluorescence signal reveals the original quantity in the sample before amplification. From the early phase of HIV infection, qPCR is capable of detection and characterization of the low-level infection. Theoretically, a well-designed PCR reaction, with low non-specific binding, can detect the presence of a single DNA molecule in the reaction tube [111]. However, a PCR assay presents a major logistical challenge for primary clinics, requiring equipment such as a clean bench, thermocycler and detection module that can cost several tens of thousands of dollars. Furthermore, the cost increases to maintain such equipment and facilities. PCR involves the heating and cooling of a sample containing target DNA and reagents upwards of 40 times. Because of this cycling process, a complete PCR reaction involves a reasonably long amount of time, usually around 2 hours, a fact which causes most PCR machines to be designed to hold many samples at one time. This greatly increases the size of these machines, which in turn raises the price. Due to such difficulty, many clinicians especially in

a tight budget condition frequently skip confirmatory diagnosis on many occasions and prescribe medicine either based on a relatively inaccurate diagnostic method or pursue empirical treatments based on vague symptoms without adequately ruling out differential diagnoses [112]. This practice has several disadvantages such as increasing the chance of wasting a limited supply of medications and increasing antibiotic/antiparasitic drug resistance in a local community. Treating patients empirically or based on comparatively inaccurate diagnostic methods also increases a chance to have a delayed diagnosis, especially in early stages of infection or in the asymptomatic phase. Complications from delayed diagnosis include irreversible organ damage, increased usage of medical supplies to contain exacerbated symptoms and failure to quarantine early. For instance, *P. falciparum* can cause ischemic insults to the brain, lungs and kidneys when not treated promptly which frequently can cause mortality to children and irreversible damage even if patients recover from a disease. When patients enter the advanced clinical phase from infectious diseases, hospitalization with intravenous support/patient monitoring is required. In addition, an antibiotic/antiparasitic is frequently required to deal with systemic inflammation caused by an infectious agent. Containment for HIV in a community level is always challenged by frequent quarantine failures due to undiagnosed/misdiagnosed asymptomatic carriers. Having access to low-cost, easy to manufacture and low-maintenance PCR equipment at a primary doctor level enables rapid on-site diagnosis which brings a great benefit to community health. Treatments can be given before infection causes more damage to patients. The clinic can be more efficient on distributing their limited medical resources and authorities can set up quarantine for rapid containment of infectious disease if needed.

Previously, attempts have been made to lower the cost and increase the accessibility of PCR instrumentations [113]–[117]. A small chip with a heater and temperature sensor was fabricated by silicon micromachining, and was integrated into a handheld device to perform qPCR in under six

minutes [114], [118]. A pocket-sized PCR thermocycler was designed by fabricating heating blocks with various temperature for convective-flow of PCR samples [116]. A real-time PCR device was made using a micro-fabricated glass device and 3D printer [117]. Most devices developed under this motivation had custom parts that needed to be manufactured with unique or expensive processes, such as printed circuit board (PCB), microfluidics, and micro-fabricated devices, in order to miniaturize the size of the device for portability (accessibility). Recently, 3D printing technology has been adapted to the medical device manufacturing [117], [119], [120]. The main reason is to reduce the cost of manufacturing medical devices and to increase the accessibility in various places around the globe through a simple process of design sharing over the internet. Microfluidic devices were fabricated using inkjet 3D printing methods as well as stereolithography [119]. A custom-built microfluidic, suitable for cultivating Methicillin-resistant Staphylococcus aureus (MRSA), was used to detect the presence of MRSA with a gold nanoparticle-based assay [120], [121].

The goal of this research is to design a low-cost 3D manufacturing method to fabricate a portable qPCR device (Figure 5.1). Thus, the digital format of design files can be shared over the internet, which enables any person to easily download the files and produce a qPCR device (Figure 5.1A). The open-source instrumentation allows wide distribution of valuable methods [122]–[125], in this case, a medical diagnostics device. For the manufacturing (Figure 5.1B), a simple 3D filament deposition printer and 3D CNC milling device are selected, because of their wide availability and low-cost (ranging from $300 - $4,000). For example: the Wanhao Duplicator I3 3D printer is priced at $379, the Inventables X-Carve CNC mill is priced between $1328 and $1608, and the ZMorph 2.0SX 3D printer /3D CNC mill used to manufacture this device is priced between $2690 and $3440. Additionally, if the person downloading the files is unable to access these 3D manufacturing tools, they can elicit the help of a third party. The device, resulting from 3D manufacturing, can perform

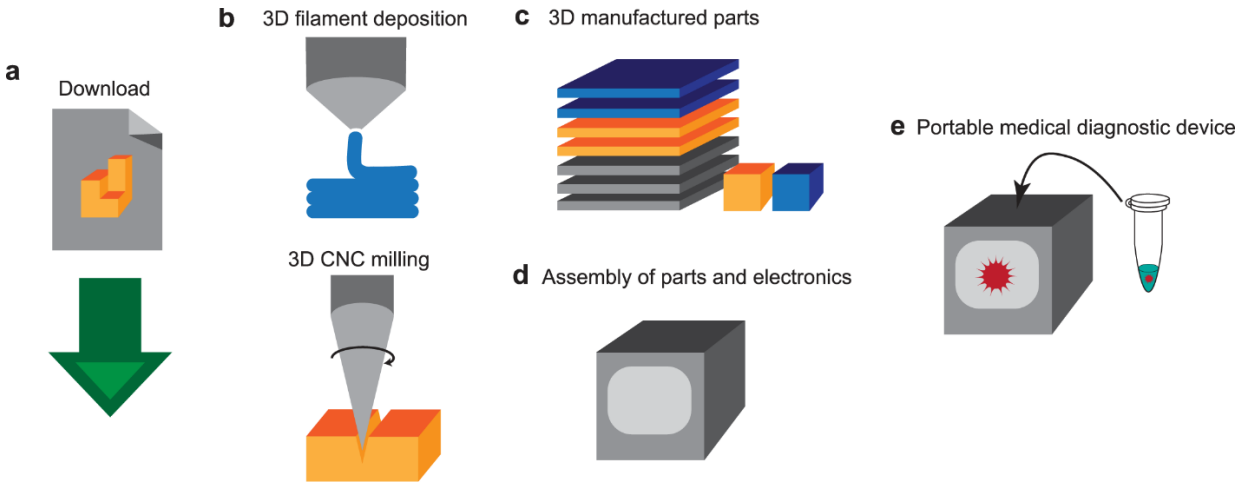


Figure 5.1. From digital design file to portable diagnostics device. (a) A digital format of design file is uploaded to the internet and downloaded by users. (b) A user uploads the digital files into 3D printer and 3D CNC milling machine for manufacturing. The 3D printer extrudes and deposits filament and the 3D CNC mill cuts and drills through material to engrave patterns and shapes. (c) This results in 3D manufactured parts for assembly. (d) The parts and off-the-shelf electronics components are assembled. (e) This assembled device can function as a portable medical diagnostic device for detecting and quantifying the pathogen in a sample through qPCR. © 2017 PLoS

real-time PCR for amplifying while monitoring the target nucleic acid sequence, and conclusively detect as well as quantify an infection of pathogens (Figure 5.1E). This study grants easy access to high-quality biochemical instrumentation on resource-limited settings for medical diagnostics.

## 5.3 Materials and Methods

The qPCR printed device consists of custom designed parts, such as a heating element, circuit board, and fixtures for the light path and casing. All of the custom parts are designed for ease of manufacturability and no dependency on advanced manufacturing infrastructure or equipment, most of which are 3D printed. The tools used for custom manufacturing are a 3D printer, a 3D milling machine, and a hand-drill. The casing for the overall device, the holder for the heating element, the fan and cooling system as well as the structure of the light path for fluorescence reading are made of 3D fused-filament deposition parts. A 3D CNC mill is used to fabricate the circuit board for the electronic controls. The device is designed to use a typical PCR tube that has several key features,

including a complete seal for inhibiting evaporation of the sample and high optical transparency for the excitation and emission wavelengths. The details of the design and manufacturing of custom parts are described in the following section. The mechanical parts of the device are designed using AutoDesk Inventor, a 3D computer-aided design (CAD) software. Using Inventor enabled the device to be designed as compact as possible by testing multiple designs without having to manufacture them. When a part is ready to be made, it is simply printed using the 3D printer or milled using the 3D CNC mill.

### 5.3.1 Heating element design

The heating element is based on a section of aluminum rod with holes axially bored in from the top and bottom (Figure 5.2A). One of these holes (① in Figure 5.2A) allows for the insertion of the PCR tube and is a depth and diameter which allows the portion of the PCR tube containing the reaction solution to be fully inserted. The other (② in Figure 5.2A) is used to increase the surface area of the rod while simultaneously decreasing the rod's volume. This is done so that both heating and cooling times are minimized. On the sides of the rod there are two additional holes. One (③ in Figure 5.2A) is located where the PCR tube is inserted and allows for light to excite the sample. The other (④ in Figure 5.2A) is located in the middle of the rod and houses a thermistor used to measure the temperature of the heating element. This aluminum rod is covered with polyimide tape that provides electrical insulation and is then wrapped with 7 turns of 0.255 mm diameter NiCr wire. This number of turns was chosen to result in a length of wire with a resistance of ~5.6 Ω that will draw ~1.3 A from the 7.4 V battery, which is below the maximum current draw of 1.6 A that can be safely used with the chosen lithium-ion batteries as per the manufacturer's datasheet. The current passed through the NiCr wire dissipates ~11.8 W and thus releases heat which is used to raise the temperature

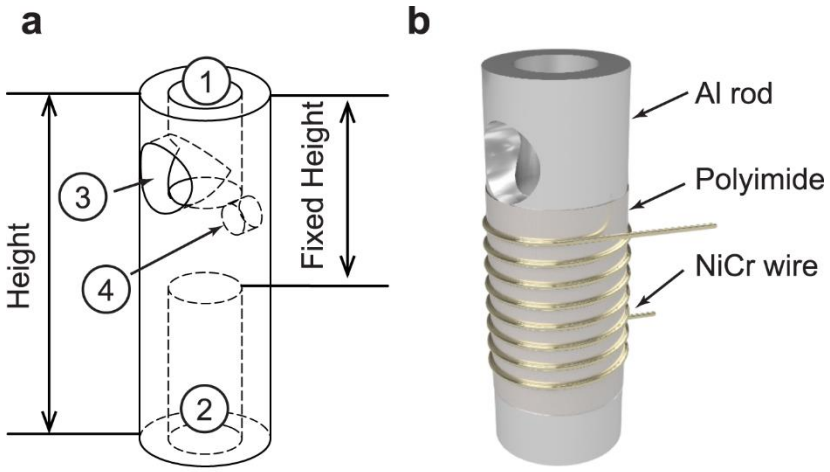


Figure 5.2. The aluminum heating element for qPCR device. (a) The aluminum rod has four holes for ① PCR tube insertion, ② convection cooling, ③ the excitation light path, and ④ thermistor insertion. (b) The heating element consists of an aluminum rod, a layer of polyimide film, and a coil of NiCr wire. The dimension and location of the holes are: ① ⌀ is 3.72 mm and depth is 5.46 mm, ② ⌀ is 3.72 mm and depth is 8.59 mm, ③ ⌀ is 3.56 mm and location from top is 3.70 mm, and ④ ⌀ is 1.59 mm and depth is 1.00 mm and location from top is 3.70 mm. © 2017 PLoS

of the aluminum rod, a process known as Joule heating. The resulting heating system has a time constant of ~9.133s.

To cool the heating element, a centrifugal fan is employed. The fan consists of a small brushed DC motor that is controlled by the microcontroller using a relay. Since electrical noise is introduced onto a portable power supply when a DC motor is operating, the motor is connected to a network of capacitors. Without these capacitors, the noise created by the motor dramatically degrades the readings from sensors using the same power source, in this case, the photodiode and thermistor. The motor drives a small 3D-printed impeller, which is the main element of the 3D-printed centrifugal fan. This impeller pulls in air at ambient temperature from the bottom of the device and accelerates it towards the aluminum heating block located in the cartridge. This process aids in rapidly lowering the temperature of the heating block, and thus, the sample. The more efficient cooling process using the fan allows for the reduction in time it takes to complete a PCR amplification. The resulting cooling

system has a time constant of ~20.97s. The dimensions of the heating element are optimized using thermal simulations.

### 5.3.2 Thermal simulation of the heating element

To achieve easy manufacturability of the heating element, the section of aluminum forming the heating block is cut from a 6.35 mm diameter aluminum rod using a saw, allowing for a variable height and a fixed outer diameter. In order to determine the optimal height of the heating element, thermal simulations are performed in COMSOL Multiphysics 5.2a to determine the effects of the element's height on the duration of heating and cooling cycles. Increasing the height of the heating element, whilst maintaining the hole diameters and distance between the top (① in Figure 5.2A) and bottom holes (② in Figure 5.2A), will increase the surface area of the rod, thus improving convection and reducing the cooling period. Additionally, the increase in height will increase the volume of the aluminum, thus increasing the heat capacity and the heating period. The simulation model consists of an aluminum rod and polyimide tape. The Heat Transfer in Solids interface in COMSOL Multiphysics is used to study the thermal conduction and convection. In the heating simulations, the joule heating from the NiCr wire is applied to the polyimide tape as thermal power. The thermal power applied is determined by measuring the power dissipated by the NiCr wire during heating cycles. In the heating simulations, a fan-less operation is assumed, while the cooling simulations are performed with a higher convection coefficient to model a fan. The convection coefficients and polyimide tape thickness, which accounts for air pockets between layers of tape in the experimental setup, are defined so that the simulation cycle time (heating and cooling) matches the cycle time measured in our preliminary data. The determined convection coefficient and polyimide tape thickness for the heating stimulations

are 15.8 W/ ($m^2$·K) and 0.73 mm, respectively. For the cooling simulations, the convection coefficient is 69.1 W/($m^2$·K) and the polyimide tape thickness is the same.

### 5.3.3 Optical design of real-time fluorescence measurement

The optical components are critical to the functionality of a real-time PCR system as they provide the means of determining the concentration of amplified target DNA. The system consists of a photodiode and emission filter located coaxially to the PCR tube, and an LED and excitation filter located adjacent to the sample (Figure 5.3). All the components used to position these optical parts in the correct locations are 3D printed. The LED emits blue light through the blue excitation filter and travels through a hole in the side of the aluminum heating block and finally illuminates the sample located in the PCR tube. The intercalating dyes in the sample emit green light when exposed to this blue excitation light in an intensity proportional to the concentration of the target DNA. This green fluorescence light travels up through the lid of the PCR tube, through the emission filter, and arrives the photodiode sensor. The photodiode produces a voltage corresponding to the fluorescence intensity emitted by the sample. This voltage is then amplified and read by the microcontroller. The resulting system is able to quantify the amplification of DNA produced by qPCR. This optical design adapts a simple separation of the emission and excitation light paths to reduce the direct injection of excitation wavelength into the photodiode. In a typical qPCR device, this is accomplished by using a dichroic mirror with a significantly separated property of reflection and transmission wavelength. However, avoiding to use a dichroic mirror simplifies the optical path design and reduces cost. Additionally, the optical filters and LED can be chosen to operate with various fluorescent dyes. For the components in this design, detailed in supplemental data S1 Table, the optics are compatible with both FAM probes as well as SYBR green dye.

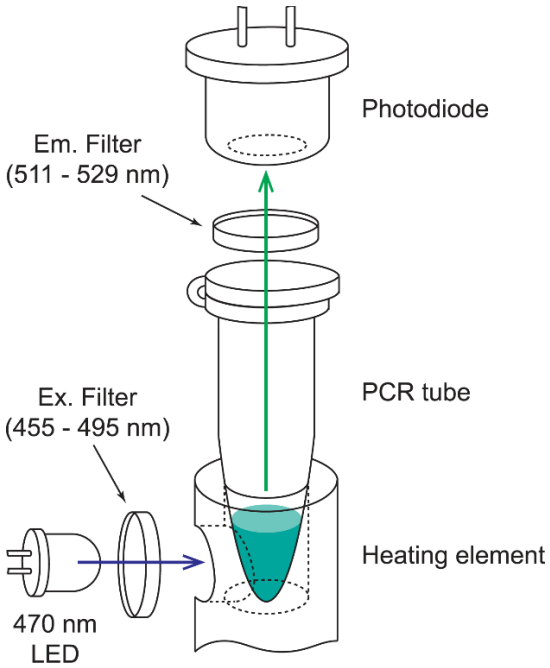


Figure 5.3. Optical design of real-time fluorescence measurement for qPCR. The blue LED (470 nm) emits excitation wavelength that is filtered through an excitation filter which is a band-pass filter of 455 to 495 nm. The excitation light travels through the hole in the aluminum rod and is absorbed to the sample in the PCR tube. The emitted light is collected by an avalanche photodiode through an emission filter, with a band-pass at 511 to 529 nm. © 2017 PLoS

### 5.3.4 3D printing and 3D milling for easy manufacturability

All the 3D-printed enclosures, holders, and parts are 3D printed using the Zmorph 2.0 SX multitool 3D printer (Figure 5.4A). For 3D printing, a 1.75 mm black ABS filament is used. This is chosen because of ABS plastic's relatively high strength compared to PLA, the other common 3D printing plastic. Black filament is used so that the case and optical components are opaque to avoid interference with the fluorescent measurements. The printing is performed with a 0.4 mm nozzle and a 0.2 mm layer height which results in a smooth surface finish, with deviations from the CAD model being less than 0.2 mm. The walls of the main case are 1.6 mm thick resulting in a structure that can support a mass of 70 kg. The Zmorph tool offers the capability to switch out the tool head to carry out different tasks, such as 3D CNC milling and paste extrusion. To integrate the heating, cooling,

and optical systems, a circuit board is made to connect all elements together. The circuit board has been made using an isolation milling process with the Zmorph 2.0 SX multitool 3D printer (Figure 5.4B). This method uses the milling tool on the printer to cut slots and holes in a piece of laminated copper board. The un-milled copper that remains forms the electrical contacts for the circuit. The electrical components are then fixed to the board by hand soldering, a process which can easily be learned by the average person. Utilizing the process of isolation milling avoids the use of another method such as a photolithographic process, which requires more equipment including a dark room for sensitizing boards, transparency printer, a UV light source for board exposure, an acid-based chemical bath for etching, and a drill press for creating holes. While effective, the difficulty of the photochemical method makes it unachievable for many. Isolation milling avoids unnecessary equipment, careful training, and hazardous chemicals. For those who do not have access to a 3D printer or milling machine, access to this low-cost qPCR machine is still a possibility. Many universities and machine shops have these 3D manufacturing machines available and will allow access to them for individual uses. Providing the files to these establishments will allow them to manufacture the parts for nothing more than a small fee. In the case of the PCB, there are numerous board houses that will accept the files and mail back finished boards for a relatively low-cost.

### 5.3.5 Electronics and closed-loop feedback

The main part of the electronic control system is the SparkFun MicroView. The MicroView is a microcontroller with a built in OLED Screen. The microcontroller is used to control the two relays that operate the fan motor and the NiCr heating wire, and is also responsible for turning on the blue excitation LED and for obtaining a reading from the photodiode. Additionally, the microcontroller takes in input from the user via a set of buttons and delivers output to the user by way of the built in OLED screen. The screen displays several menu-based interfaces to the user.

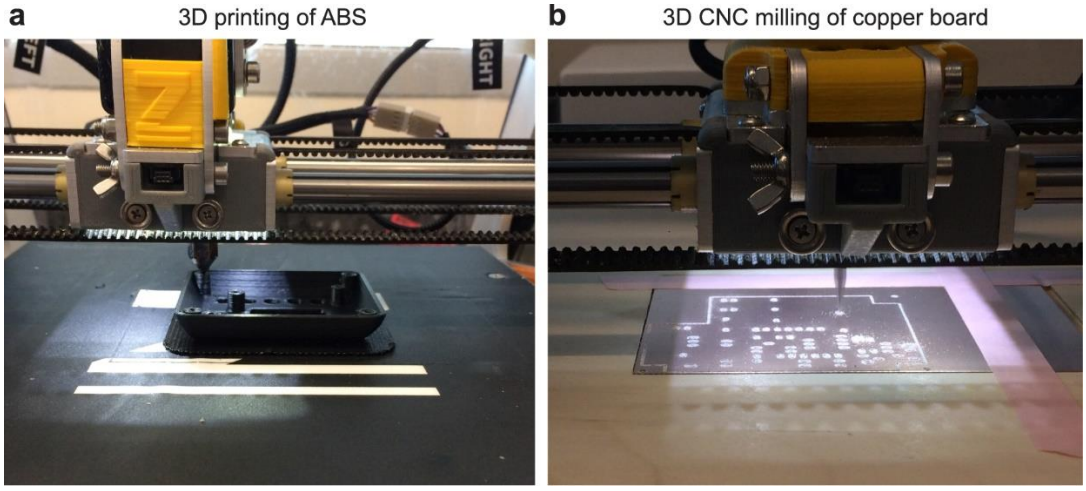

Figure 5.4. Photographs of 3D printing and 3D milling of all the parts using a multitool 3D printer. (a) The faceplate is being printed with black ABS material on a heated bed. (b) The main board is being engraved using 3D CNC mill. © 2017 PLoS

These include: "New PCR" and "View Data". "New PCR" begins the thermocycling and displays the current temperature reading, the current cycle number, the most recent fluorescent measurement, and a plot of the temperature in real time. "View Data" shows the fluorescent measurements for each cycle number in both a tabular and graphical format and can be accessed while the PCR reaction is taking place. The software that controls the operation of the device and runs on the microcontroller is responsible for reading the buttons, controlling the heater and fan, enabling the LED, measuring the fluorescent reading, and displaying information on the screen. The temperature control works using a thermistor mounted on the aluminum heating block. This thermistor is connected in series with a 10 kΩ resistor and creates a voltage divider. The result is a voltage that is proportional to the temperature of the aluminum block. This voltage is read by the microcontroller and converted to degrees Celsius. When in the thermocycling mode, the microcontroller enables the heater. Once the temperature reaches a high threshold, the fan is enabled and the heater is disabled. The fan blows ambient temperature air over the aluminum block and cools until the low threshold is reached. The

fan is then disabled and the heater enabled for short pulses until the temperature inside of the tube finally reaches the low threshold. At this point, the LED is enabled and 5 readings are taken from the photodiode. The median of these five samples is recorded to avoid any errors caused by noise on the reading. All the electronic components used are listed in S1 Table in supporting information.

### 5.3.6 Sample preparation and detection of lentivirus

Lentivirus, a virus family that HIV belongs to, is used to test the 3D manufactured qPCR device. The lentivirus containing a mouse *SOX2* gene sequence [126], which is targeted for amplification and detection. Real-time Reverse-Transcription Polymerase Chain Reaction (RT-qPCR) is performed. Initially, the RNA is reverse transcribed into cDNA, and the qPCR cycle amplifies the amount of DNA and monitors the corresponding fluorescence changes. The purified virus sample (2 μL) of various concentration tested is mixed into a typical PCR tube with RT-PCR reagents and TaqMan Gene Expression Assay, Mm00488369_s1, that targets 68 bp of the mouse *SOX2* gene. The lentivirus, containing the mouse *SOX2* gene, is chosen to reduce risk of HIV infection to the researcher during this work, while still being able to simulate the detection of lentivirus RNA. Three virus concentrations were tested, $2 \times 10^7$ vp/mL, $2 \times 10^6$ vp/mL, and $2 \times 10^5$ vp/mL, to determine the quantification capability of the presented device. These viral loads are clinically relevant for HIV infection [127]. The total volume of a reaction mix is 20 μL. The reverse transcription step is performed at 55 °C for 10 minutes, and the PCR cycles are performed at 95 °C for denaturing and at 60 °C for annealing and extension. The lysis of lentivirus is not conducted separately, and is integrated as a part of reverse transcription step. To confirm the product length of the qPCR, a gel electrophoresis is used. A 3% Agarose gel (50 mL of 1× TBE, 1500 mg Agarose powder and 5 μL of 10,000× SYBR safe gel stain), with a channel length of 100 mm is ran at 75V for approximately 2 hours.

## 5.4 Results

### 5.4.1 3D assembly of the system

The structure of the system consists of four assemblies and a case enclosing them. An exploded view of the system is shown in Figure 5.5A, indicating the placement of all components with respect to each other. The detailed structures of each assembly, control assembly, photodiode assembly, bottom assembly, and cartridge assembly, are presented in Figure 5.5B. The control assembly contains of all of the electronics that control the device as well as the user interface. This assembly is made of two circuit boards and a faceplate. The lower main board holds the MicroView, photodiode amplifier, and heater and fan relays, as well as the connectors for the cartridge, fan, LED, and upper control board. The control board contains the connection to the battery, the power switch, and control buttons. This assembly is mounted to the top of the case with screws. Under this assembly and mounted to the case is the photodiode assembly. This assembly houses the photodiode as well as the green emission filter. The main housing for the photodiode assembly also contains a tapered portion that helps to align the cartridge with the photodiode when inserted. The bottom assembly houses the fan, the LED and the blue excitation filter. The opening in the bottom cover allows for the insertion and removal of the cartridge. The cartridge consists of a cylindrical shaped housing which accepts a typical PCR tube. On the lower side of the cartridge is a cover with several holes, the central hole holds the aluminum heating block while the outer holes allow for warm air to escape. Along the back side of the cartridge is a channel that holds the wires for the heating element and the thermistor to reach the connector on the top. This connector makes contact with the main circuit board when the cartridge is inserted into the case. Two holes in the side of the cartridge allow for the entrance of air on the left side and for the entrance of blue light from the right. The control,

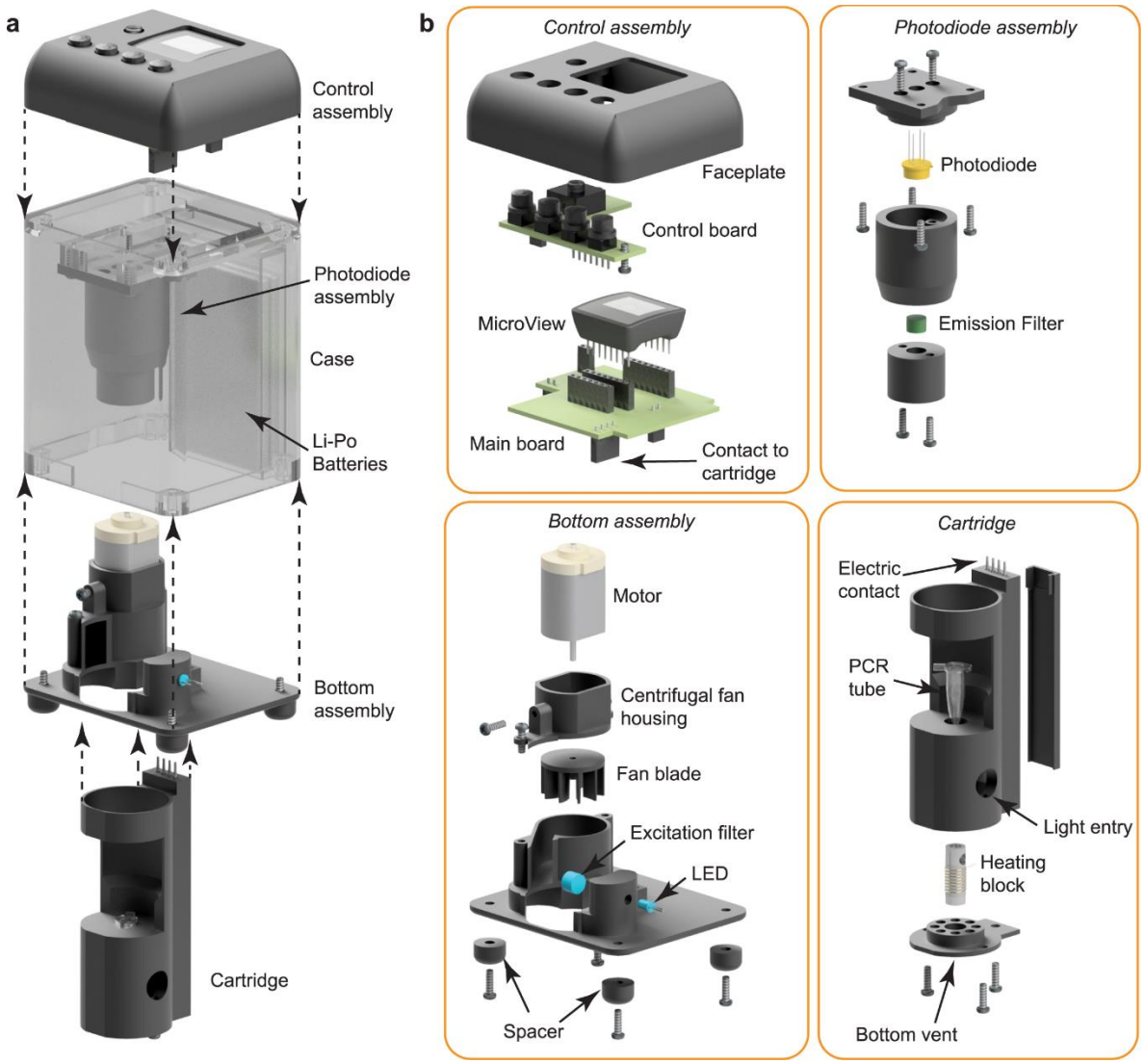


Figure 5.5. 3D assembly of the system with exploded views. (a) The complete device showing locations of Control assembly, Photodiode assembly, Bottom assembly, Case, and Li-Po batteries. (b) Detail of assemblies. The Control assembly contains a faceplate, a control board, a main board, and a MicroView microcontroller. This assembly provides a user interface and houses all electronic controls. The Photodiode assembly contains the photodiode and emission filter. This assembly is used to determine the target DNA concentration present in the sample. The bottom assembly contains a motor, a fan blade, spacers, and a centrifugal fan housing, forming the cooling fan system. It also contains an LED and excitation filter, establishing the light source for illuminating the sample. The cartridge is a removable assembly allowing for easy insertion of the PCR tube containing the sample. It contains the heating block, electrical contacts for connection to the main board, and a vented bottom plate allowing for the escape of warm air. © 2017 PLoS

photodiode, and bottom assemblies are mounted to the case. The case also holds two lithium polymer batteries used to power the device. The digital file used for this assembly is shown in S1 Fig and uploaded as S1 File and S4 File in supporting information.

### 5.4.2 Optimization of thermocycling

Simulations are performed to optimize the height of the rod used in the heating element to minimize the duration of thermocycling. To do this, the height of the rod is varied. The smallest presented height of 18.5 mm (Figure 5.6) is the practical limitation for the aluminum rod to retain manufacturability with spacing for NiCr wire and holes. The heating periods are 9.5, 10.7, 11.6, 12.3, and 12.9 seconds for the heights 18.5, 23.1, 27.7, 32.3, and 36.9 mm respectively (Figure 5.6A and C). The increase in the heating period is directly related to the aluminum rod height as predicted. For the heights 18.5, 23.1, 27.7, 32.3, and 36.9 mm the cooling periods are 26.6, 25.4, 24.7, 24.2, and 23.9 seconds respectively (Figure 5.6B and C). As expected, the decrease in the cooling period is inversely related to the aluminum rod height. Although the heating and cooling periods react predictably to changes in height, the rate at which the cooling period decreases is lesser than the rate at which the heating period increases. This provides a motivation to decrease, rather than increase, the height of the heating element to reduce the period of a thermocycle. For a fanless system the contrary is true and there is motivation to increase the height of the heating element to decrease the period of a thermocycle. To achieve the shortest thermocycle period, the optimal height of the aluminum rod is 18.5 mm.

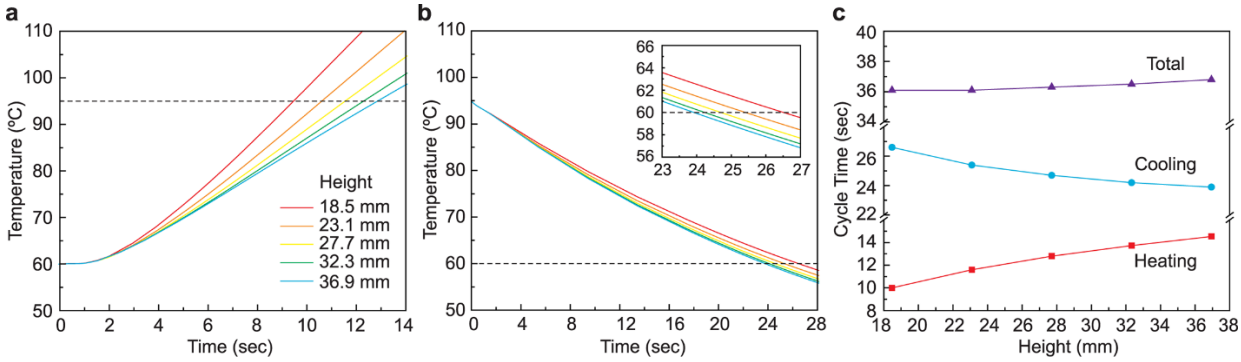


Figure 5.6. The thermal simulation of the heating element's heating and cooling cycle time. (a) The heating time from 60 °C to 95 °C in various heights of heating element. The shortest (9.5 seconds) to heat is 18.5 mm in height. (b) The cooling time from 95 °C to 60 °C in a fan-operating condition. The shortest (23.9 seconds) to cool is 36.9 mm in height. Increasing the height of the aluminum rod increases the surface area, resulting in improved convection and the length of the cooling period is reduced. The subset graph is an expended view at 23 to 27 seconds. (c) The summary of heating and cooling time for various heights of heating element. The height with the shortest total cycling time is 18.5 mm (36.1 seconds). The heating period increases at a faster rate to the increase in height than the cooling period decreases. © 2017 PLoS

### 5.4.3 Feedback calibration of thermocycling

Since the temperature of the sample cannot be taken directly from the inside of the PCR tube, the temperature must be measured at the heating element. Thus, a calibration of sample temperature is necessary and must be performed in the ambient environment where the PCR reaction will take place. A test setup is made with an additional temperature probe placed inside of the PCR tube, along with 20 microliters of water coated with 20 microliters of mineral oil to simulate a sample being present in the tube. The high and low temperature thresholds used for the feedback control by the microcontroller, are then adjusted until the temperature of the sample cycled between 60 °C and 95 °C, which is ideal for the primer and DNA sequence used in this work. The resulted calibration used the low threshold of 59 °C and the high threshold of 125 °C, the sample temperature of 60 °C and 95 °C, respectively, as shown in Figure 5.7.

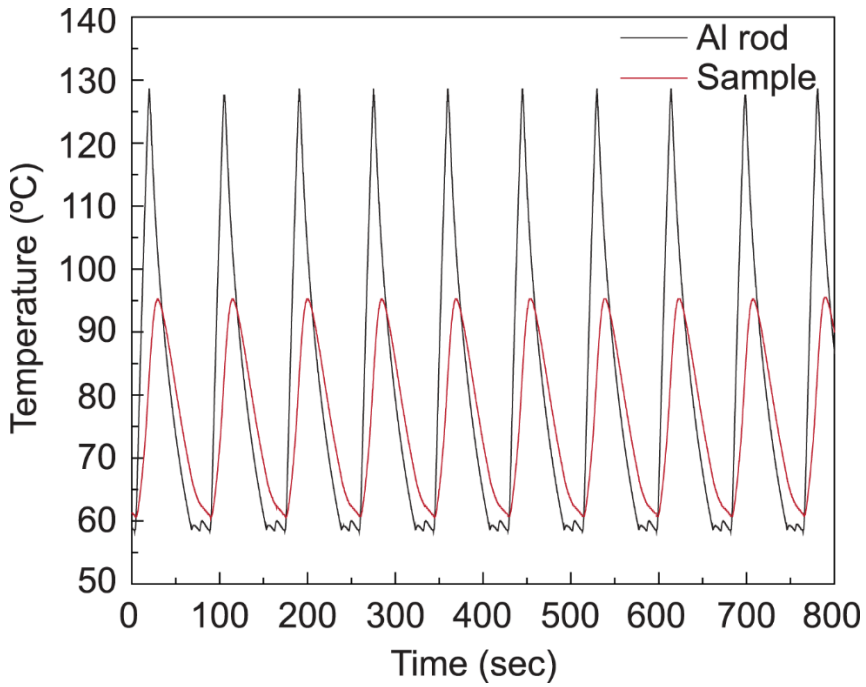


Figure 5.7. The temperature plot of the sample and the heating element for calibration. The plot is used to determine proper thermocycling control thresholds. The gray curve shows the temperature of the aluminum heating block; the red curve shows the temperature inside of the 20ul sample inside of the PCR tube. © 2017 PLoS

### 5.4.4 Quantitative viral detection using 3D manufactured qPCR device

The overall dimensions of the final assembled device are approximately 12 × 7 × 6 $cm^3$ with a mass of 214 g (Fig 8A). The bottom of the device has several critical elements (Figure 5.8B), including the opening which allows insertion of the cartridge, the air inlet for the centrifugal fan, and four spacers. These spacers allow for air to flow freely under the device when sitting on a flat surface, such as a benchtop. The dimensions of the cartridge are approximately 7.6 × 3.4 × 2.9 $cm^3$ (Figure 5.8C). The PCR tube containing the sample is inserted into the cartridge allowing for contact with the heating block. During the PCR cooling phase, the ambient air is pulled into the bottom assembly through the inlet of the centrifugal fan (Figure 5.8B) and the fan blade accelerates the airflow toward the air inlet of the cartridge (Figure 5.8C). This increases the convection coefficient on the heating element to

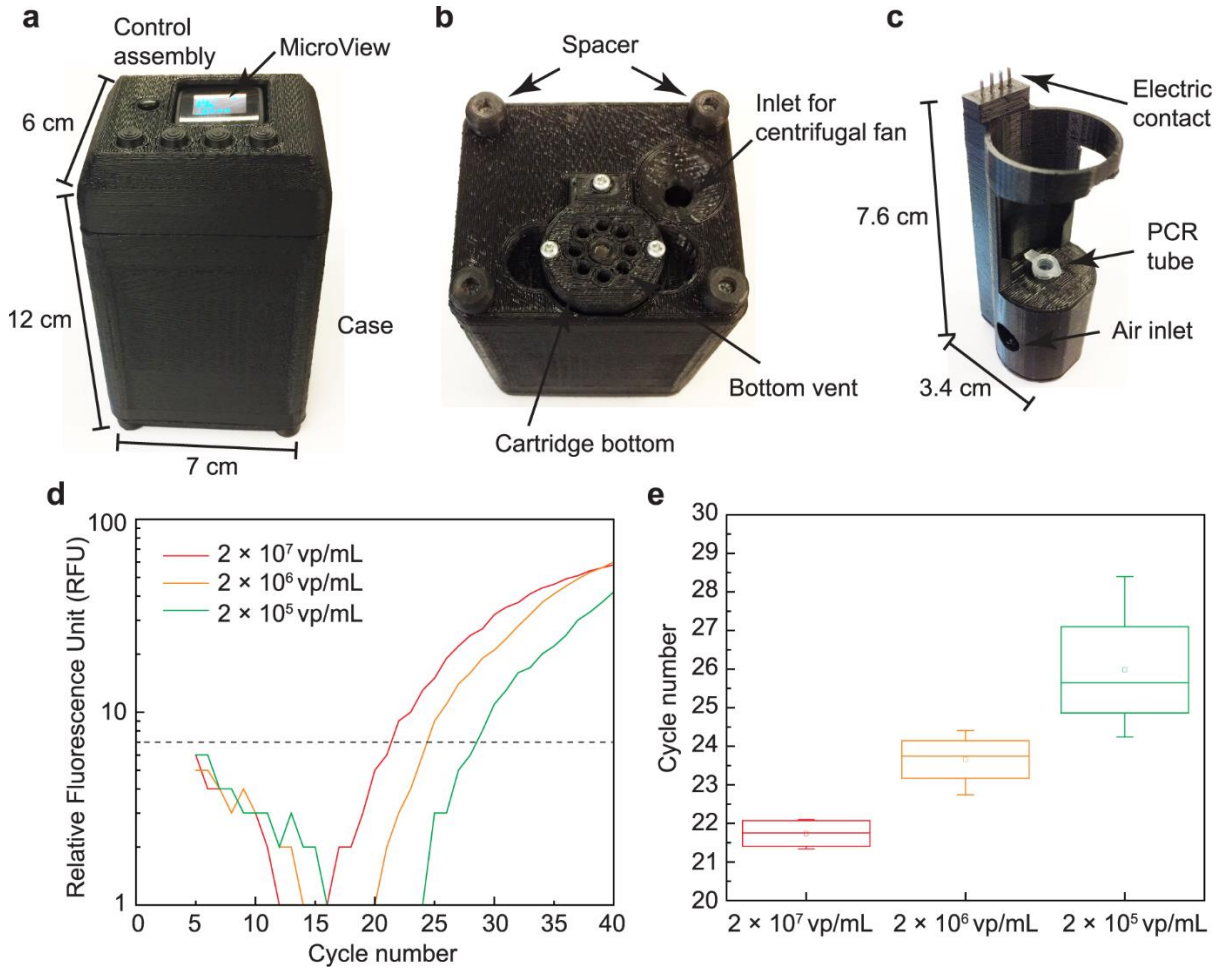


Figure 5.8. The photograph of 3D manufactured qPCR device and the resulted RT-qPCR from 3D manufactured qPCR device from three separate qPCR using 3 dilutions of target virus, $2 \times 10^7$ vp/mL, $2 \times 10^6$ vp/mL, and $2 \times 10^5$ vp/mL. (a) The dimension of the qPCR device is $12 \times 7 \times 6$ $cm^3$. The MicroView shows the status of amplification cycle and fluorescence reading. (b) The bottom view of the qPCR device showing cartridge bottom and an air inlet for centrifugal fan. (c) The size of the cartridge that holds PCR tube during qPCR is $7.6 \times 3.4 \times 2.9$ $cm^3$. (d) Measured fluorescence readings show the shift in the intensity measurements corresponding to the differing concentrations of target virus. The threshold for determining $C_q$ is also shown is a dotted line. (e) Measured Cq for three concentrations of target DNA. The mean and standard deviation of $C_q$ are $21.74 \pm 0.39$, $23.66 \pm 0.70$, and $25.98 \pm 1.75$, for $2 \times 10^7$ vp/mL, $2 \times 10^6$ vp/mL, and $2 \times 10^5$ vp/mL, respectively. © 2017 PLoS

accelerate the cooling. Then, the air is pushed out from the cartridge through the bottom vent (Figure 5.8B). This airflow continues until the desired temperature is met for annealing and extension of DNA.

The electrical wiring for the NiCr heating coil and thermistor run along the rear portion of the cartridge up to the electrical contacts located at the top of the cartridge (Figure 5.5B). These contacts mate with a connector located on the main board in the control assembly at the top of the device. The main objective of quantitative real-time PCR is to determine the concentration of target virus present in the sample (Figure 5.8D and E). Three different concentrations of virus sample are prepared, $2 \times 10^7$ vp/mL, $2 \times 10^6$ vp/mL, and $2 \times 10^5$ vp/mL. Experiments on each concentration are repeated 4 times with freshly prepared samples to verify the repeatability of the device. In order to determine the $C_q$, MATLAB is used to automate the analysis. The intensity readings are sent from the device's microcontroller to a PC using a serial connection and logged into MATLAB with the corresponding cycle number. The first step in the analysis is to omit the first 5 cycles to avoid reaction stabilizing artifacts. Following this, the set of data from multiple sets is normalized so that differences in baseline fluorescence are removed. A plot of three normalized curves is shown in Figure 5.8D. Each curve is then fit to a polynomial curve to smooth out the discrete steps caused by the digitization of the intensity measurements as well as to reduce noise on the measurements. The polynomials are then solved to find the corresponding cycle number where each curve crossed a threshold, or the $C_q$. The results from three concentrations are shown in Figure 5.8E. The threshold is determined based on the noise level of the fluorescence baseline. The raw data from the photodiode, including the result from the negative control, is shown in S3 Fig. The negative control had no fluorescence increase as expected. The qPCR typically required 90 minutes to complete the entire process, from reverse-transcription to 40 cycles of PCR. The measured $C_q$ (mean ± standard deviation) are 21.74 ± 0.39, 23.66 ± 0.70, and 25.98 ± 1.75, for $2 \times 10^7$ vp/mL, $2 \times 10^6$ vp/mL, and $2 \times 10^5$ vp/mL, respectively. For each concentration the $C_q$ clearly shifts between 2 and 3 cycles as one would expect for a ×10 dilution. However, the standard deviation in samples with $2 \times 10^6$ vp/mL and $2 \times 10^5$ vp/mL are

significantly larger than that of $2 \times 10^7$ vp/mL. This can be interpreted as a simple human error in accurate dilution. If the deviation is originating from the device, the original sample with $2 \times 10^7$ vp/mL, supplied by a vendor, should have been detected with a large deviation as well, which is untrue according the data (standard deviation = 0.39 cycle). This can also explain the low cycle count (2±3 cycles) separation between $C_q$ of ×10 dilutions. Ideally, the separation should be close to 3.32. The amplification using the presented qPCR device is confirmed by performing a gel electrophoresis. In Figure 5.9, the amplifications are compared with a conventional qPCR machine (Applied Biosystems 7900HT). A negative control and a sample with $2 \times 10^7$ vp/mL are thermally cycled and read using both the conventional machine and the presented qPCR device. The negative control and virus-containing sample results from the 3D printed device matches those from the conventional machine as shown in Figure 5.9. The length of amplicon amplified used for this experiment is 68-bp and the band shown in two negative controls are primers, consistent with other RT-PCR performed on TaqMan samples in other literature [128].

## 5.5 Conclusions and Discussions

The presented device has met the goals for easy manufacture and quantitative viral detection. The custom parts, including circuit boards, mechanical housing and holders, and the aluminum heating block, are easily made by a 3D printer, a 3D CNC mill, and by hand using simple tools. The majority of electronic parts are simple off-the-shelf parts that can be easily purchased. The total estimated cost of a unit is ~300 USD. A breakdown of this cost is shown in supplemental data in S1 Table. The use of the 3D printer has allowed for rather complex components to be made in a rapid and low-cost fashion which greatly opens access to this qPCR device, as well as future medical devices. For example, the resulting system contains thirteen unique 3D designed and printed components, each of which would be out of reach for someone without access to a machine shop. The low standard deviation of

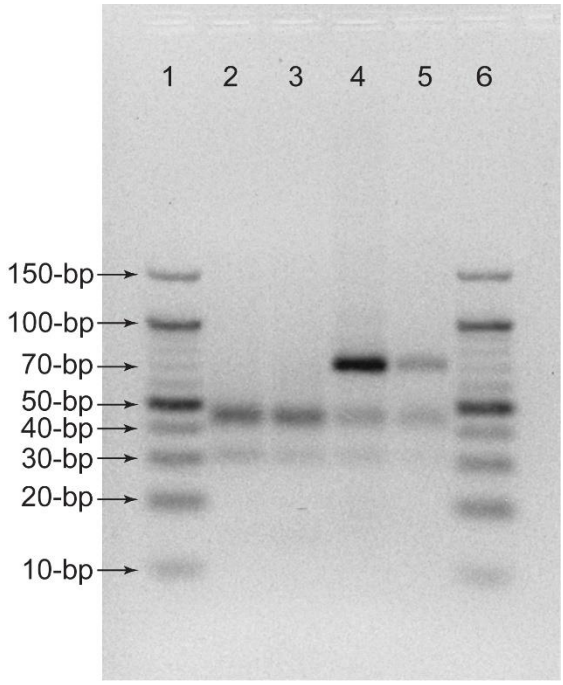


Figure 5.9. Comparison of conventional qPCR machine and 3D printed device using gel electrophoresis. Each lane included: (lane 1 and lane 6) 10-bp DNA ladders, (lane 2) negative control from conventional device, (lane 3) negative control from 3D printed device, (lane 4) $2 \times 10^7$ vp/mL sample from conventional device, and (lane 5) $2 \times 10^7$ vp/mL sample from 3D printed device. © 2017 PLoS

$C_q$ for $2 \times 10^7$ vp/mL indicates that the quantification is highly repeatable in this device. The recorded $C_q$ can be used as a calibration curve to quantify a patient sample with unknown amount of pathogen. The shift of $C_q$ toward high cycle counts is observed for lower-level concentrations, which indicates a successful quantification in the diluted sample as well.

Several challenges were addressed for the success of this project. One is the importance of the light path design. Our experimentation has shown that the layout of the light path is critical in obtaining an accurate fluorescent measurement. Also, the reasonable heating and cooling duration was a topic that needed to be investigated. In order to be consistent with the theme of this work, a simple fan-based cooling method is used, rather than adapting more elegant cooling methods, such as a Peltier device. However, the fluorescence-based quantitative reading requires a complete enclosure around

the heating element and the sample to reduce background noise in the photodiode reading. To satisfy both conditions, a centrifugal fan design is adapted to redirect the air inlet to the air vent, which inhibits any directional external light exposure to the photodiode through the air inlet and vent. As a part of future work, new heating and cooling mechanisms are being investigated to reduce the total qPCR duration. One important topic that is not addressed in the work is sample preparation. In order for a qPCR diagnostic device to be highly relevant in a resource-limited setting, it is essential to have an easy and low-cost solution for sample preparation, prior to qPCR detection. This is particularly true when using a blood sample that can inhibit PCR. The DNA or RNA needs to be extracted from the raw sample before loading the sample into the qPCR device. We are working toward integrating a simple sample preparations scheme to enhance the usefulness of the presented work.

## 5.6 Supporting Information*

**S1 Fig. The digital design files corresponding to each parts of 3D assembly.** The 3D model is given in STL file format, a file type commonly used for rapid prototyping and 3D printing. The file format for circuit boards, Control Board and Main Board, is DXF, that is compatible with 3D CNC mill. (EPS)

**S2 Fig. The circuitry and circuit board used in the control assembly.** (a) The control board consists of switches and pull-up resistors, that offers user interface with the microcontroller for initiation and control of qPCR. (b) The main board consists of a microcontroller, an amplifier for photodiode, a voltage regulator, and two relays for motor and heater controller. The circuit board layout (c) for control board, and (d) for main board are used in a 3D CNC mill for circuit board fabrication. (EPS)

* This supporting information is available online from the PLoS webpage at: https://doi.org/10.1371/journal.pone.0179133

**S3 Fig. Measured qPCR fluorescence readings including the negative control.** The raw data from the photodiode is read in voltage and is plotted after baseline subtraction. This data is used to produce the log-scale qPCR plot in Fig 8. (EPS)

**S1 File. This file contains all the 3D models in STL format.** The included files are: Bottom Plate.stl, Button Piece.stl, Cartridge Housing.stl, Case.stl, Emission Filter Holder.stl, Faceplate. stl, Fan Blade.stl, Heater Holder.stl, Motor Holder.stl, Photodiode Assembly Mount.stl, Photodiode Holder.stl, Spacer.stl, and Wire Cover.stl. The assembly order can be found in S1 Fig. (ZIP)

**S2 File. The file contains DIPTRACE file for control board and main board.** Also, DXF files are provided for 3D CNC milling. (ZIP)

**S3 File. The Arduino code is for programming the microcontroller for qPCR.** (ZIP)

**S4 File. This file contains all the source CAD files which includes those to create the STL files for printing.** Also, the 3D assembly of the device (3D Printed PCR.iam) as well as subassemblies and individual parts are contained in this file. (ZIP)

**S1 Table. The list of components used in the qPCR device.** (EPS)

# CHAPTER 6: HANDHELD BATTERY-OPERATED SAMPLE PREPARATION DEVICE FOR qPCR NUCLEIC ACID DETECTIONS USING SIMPLE CONTACTLESS POURING

## 6.1 Chapter Notes

For a complete diagnostic system relying on PCR, it is necessary to prepare patient samples so they are compatible with the PCR reaction's chemistry. For bloodborne diseases, this requires removal of most of the material found in the blood which would otherwise inhibit the reaction. In this paper we present a device that automates most of the sample preparation process to further reduce the required skill needed to perform a successful PCR diagnostic from a blood sample. A typical benchtop sample preparation requires a skilled lab technician and multiple non-reusable pipette tips. The technician must carefully pipette appropriate volumes of reagents from one tube to another in multiple tedious steps. To remove this requirement, this paper presents a device which automates all of the sample washing steps using magnetic separation. The battery-operated device utilizes a microcontroller controlling two stepper motors to move a sample-containing tube and a magnet, and a peristaltic pump to precisely dose washing buffer. This study shows that this device is capable of performing the washing steps more effectively and consistently than a human technician manually using pipettes, and does so without requiring as many consumable supplies. Devices such as this are critical to provide the ultimate goal of a fully automated PCR based diagnostic system. The paper was co-authored by Alissa Vuillier, Manjusha Vaidya, Kiminobu Sugaya, and Brian N. Kim[*].

[*] This chapter uses previously published material from Analytical Methods, 2018. Reproduced from Ref. [152] with permission from the Royal Society of Chemistry.

## 6.2 Introduction

Considering the emergence and persistence of infectious diseases such as malaria and Zika virus throughout the world, quantitative polymerase chain reaction (qPCR) processes have become increasingly useful to accurately test for these diseases and to also reveal the stage of infection by quantification [129]. However, alternative diagnostic methods are often used because qPCR requires a labor-intensive sample preparation process [130]. In a sample preparation process, nucleic acids (DNA and RNA) are extracted and purified from whole blood by removing other components of blood which can impede the nucleic acid detection mechanism. Sample preparation is involved in most diagnostic biochemical assays using whole blood [131]. When a person is speculated to be infected with pathogens by exhibiting common symptoms, their blood is drawn and transported to a centralized laboratory where the sample can be used for preparation and detection. Depending on the location, this process can take hours to days due to transportation and required labor. At the laboratory, the blood undergoes a sample preparation procedure, which involves many manual pipetting steps to perform blood lysis, DNA/RNA capture, washing, and elution (Figure 6.1a) and thus can only be done by a skilled person at a specialized laboratory. Despite its limitations, this procedure has seen minimal changes in laboratory settings over the last two decades [132]. Therefore, simple, low-cost, and robust sample processing tools requiring no skilled labor are currently in demand to enable early diagnosis of infectious diseases.

Several approaches to simplifying PCR sample preparation have been proposed and tested in the past for rapid detection of diseases. A lab-in-a-drop system was developed to integrate point-of-care detection of nucleic acid biomarkers into a single fluid droplet [133]. A rotationally-driven microdevice integrated mixing capability with multiplexed PCR amplification to simply the design and increase efficiency, resulting in a novel and inexpensive PCR amplification system [134]. These

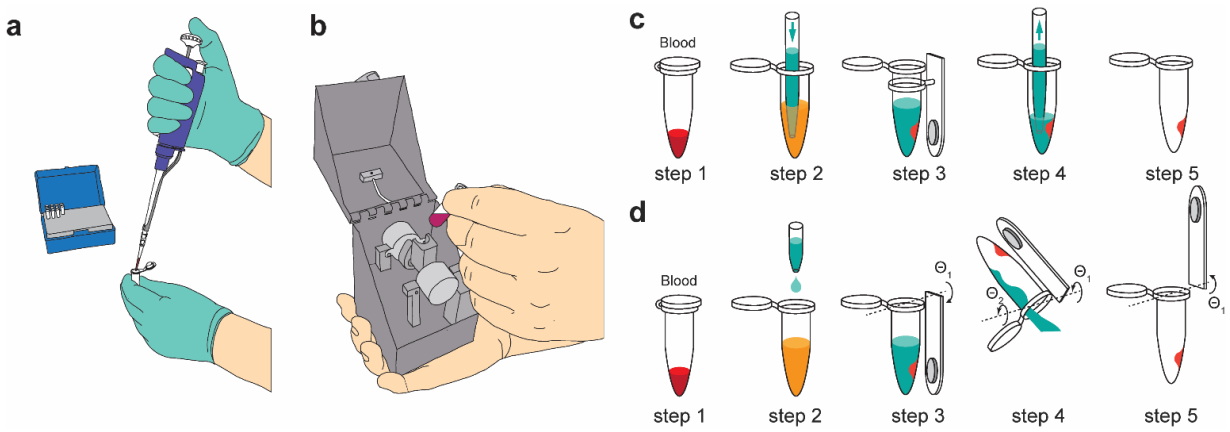


Figure 6.1. Overview of the labor-intensive manual sample preparation and the automated sample preparation device. (a) Typical sample preparation requiring manual handling of the sample using pipettes and disposable pipette tips. (b) The handheld sample preparation device which autonomously processes whole blood. (c) The sample preparation using magnetic beads and manual pipettes: (step 1) adding whole blood sample, (step 2) adding washing buffer, (step 3) separating magnetic beads, (step 4) removal of supernatant liquid using pipette, and (step 5) resulting in isolated DNA. (d) Detailed operation of the automated method: (step 1) adding whole blood sample, (step 2) adding washing buffer using integrated contactless dispenser, (step 3) separating magnetic beads using a rotating magnet arm, (step 4) removal of supernatant liquid using contactless pouring, and (step 5) resulting in isolated DNA. © 2018 RSC

approaches hold similarities in their attempts to lower costs and increase efficiency of sample preparation devices. Much recent research has moved more specifically in the direction of portable devices [135]. A portable room-temperature sample preparation system is pressure-driven for centrifuge-free nucleic acid extractions [136]. A chemical heater system was created to conduct rapid lysis to create a disposable system for increased convenience [137]. This approach to dry enzyme storage and sample heating was proven effective in amplifying both DNA and RNA, and was even capable of usage in low-resource laboratories. Additionally, electronic approaches have been studied in order to provide a hands-free sample preparation process. One system in particular integrates all the necessary agents for cell lysis, washing, and elution onto one chip to allow for total sample preparation to be handled at once [138]. Much research has strived for hands-free solutions, just as the device proposed in this paper is contact-free. Some research has utilized magnetic beads,

particularly a magnetically actuated bead-beating system. One such system specifically performs sample lysis using the magnetic beads, before a centrifuging clarification step [139]. This enables the device to efficiently extract nucleic acid from biological samples. Similarly, a magnetic bead suspension can be used to trap magnets and release periodically. By rotating small permanent magnets, another device is able to conduct a washing cycle with high purification efficiency [140]. It is worth noting that irreversible bead aggregation can affect the DNA purification and the efficiency of diagnostic [141]. Often, the irreversible bead aggregation is caused by the overexposure to the magnetic force. It is important to precisely control the magnetic exposure to yield a reliable DNA extraction efficiency. Throughout all research in this area, integrating efficiency, portability, and effectiveness has been identified as a key priority for a novel PCR point-of-care sample preparation device.

In this paper, we present a simple, handheld, battery-operated sample preparation device designed to minimize a user's skilled labor (Figure 6.1b). By simply inserting the sample, washing and DNA capture steps can be autonomously performed. To enable this, a simple pouring scheme is adapted. Manual sample preparation methods, as well as commercially-available automated sample preparation devices, rely on pipetting to exchange and transfer liquids (Figure 6.1c) [132]. The pipette uses disposable pipette tips which are designed for one-time use. Because pipette tips come in contact with the sample (Figure 6.1c, step 2 and step 4), they need to be replaced after every usage to prevent contamination. In manual and commercial automated sample preparation methods which are based on magnetic bead-based separation, the blood lysis buffer and magnetic beads are added to whole blood (Figure 6.1c, step 2), which promotes the binding of free DNA/RNA to magnetic beads. Beads with captured DNA molecules are accumulated by a magnet (Figure 6.1c, step 3). The supernatant liquid is removed by pipetting (Figure 6.1c, step 4), which results in a clump of magnetic beads. Steps 2, 3, 4, and 5 are repeated to thoroughly wash the beads before using DNA for nucleic acid detection.

Contactless pouring and dispensing to remove and add liquid can eliminate the need to replace disposable parts, like the pipette, and simplify the procedure. An overview of the pouring method is shown in Figure 6.1d.

The process begins with raw sample from a patient (Figure 6.1d, step 1), containing a large concentration of hemoglobin that is inhibitory to qPCR. This sample is placed into the automated sample preparation device (Figure 6.1b). At the beginning of the process, a tube is loaded into the device containing the sample (Figure 6.1f). This sample contains magnetic beads which bind to DNA in the sample. The tube motor then returns to the home position ($\theta_2 = 0°$) while the magnet motor simultaneously rotates to the downward position ($\theta_1 = 0°$). While in this state, the magnet is in a close proximity to the sample, attracting the magnetic beads to the tube wall. This step is ~30 seconds and results in a separation of magnetic beads by forming a bead pellet (separation step). To remove the supernatant before washing, both motors rotate simultaneously ($\theta_1 = \theta_2 > 100°$) so that the supernatant is poured into the waste reservoir, while the magnetic beads are left attracted to the tube wall (pouring step). To add new washing buffer, the tube motor rotates the sample tube to the home position while the magnet moves away to the upward position ($\theta_1 = 180°$). Then, the peristaltic pump is enabled, dripping washing buffer from the washing reservoir to the sample tube (washing step). This step is followed by the resuspension of the magnetic beads by rotating the tube motor back and forth between $-90° < \theta_2 < 90°$ to gently remove the bead pellet off the tube wall (resuspension step). The process, consisting of separation, pouring, washing, and resuspension steps, repeats several times, repetitively purifying the DNA targets in every cycle. This sample can then be used in a real-time qPCR device to perform the PCR reaction and determine the level of infection in the patient's sample.

## 6.3 Experimental

The contactless sample preparation device is designed using the pouring scheme to enable the automation of the DNA/RNA extraction process without many disposable parts that need to be replaced often.

### 6.3.1 Device design and fabrication

The automated sample preparation device is designed to perform a magnetic bead-based DNA isolation from whole human blood. The mechanical design for the device was performed using Inventor 3D CAD software (Autodesk, San Rafael, CA). Parts for this device are fabricated using a 3D-printer for low-cost manufacturing at the prototyping stage. The 3D printed parts are printed with a 0.2 mm layer height at 200 °C at 60 mm/s. The device consists of nine 3D-printed parts, magnets, two stepper motors, a control circuit board, a pump, and two lithium-ion batteries. The design of the device is shown in Figure 6.2. The operation of the device involves the movement of the two stepper motors, one motor moving the magnet ($\theta_1$) and the other moving the sample tube ($\theta_2$). The position depicted in Figure 6.1d, step 3 is when $\theta_1 = \theta_2 = 0°$. We used permanent magnets for the bead separation over an electromagnet to reduce power consumption. The small neodymium magnets produce a powerful magnetic field and have the added benefit of requiring no power to be consumed during their use, increasing battery life, an important consideration for a device designed for use at the point-of-care. The device is designed with integrated electronics to automate the sample preparation procedure by controlling the two stepper motors and peristaltic pump. An on-board microcontroller (Atmel ATmega328P) uses embedded programming to automate and time each step of the sample preparation. Two 3000 mA·h lithium-ion 18650 batteries are used for the power supply. The stepper motors are controlled through stepper motor drivers which take control signals from the

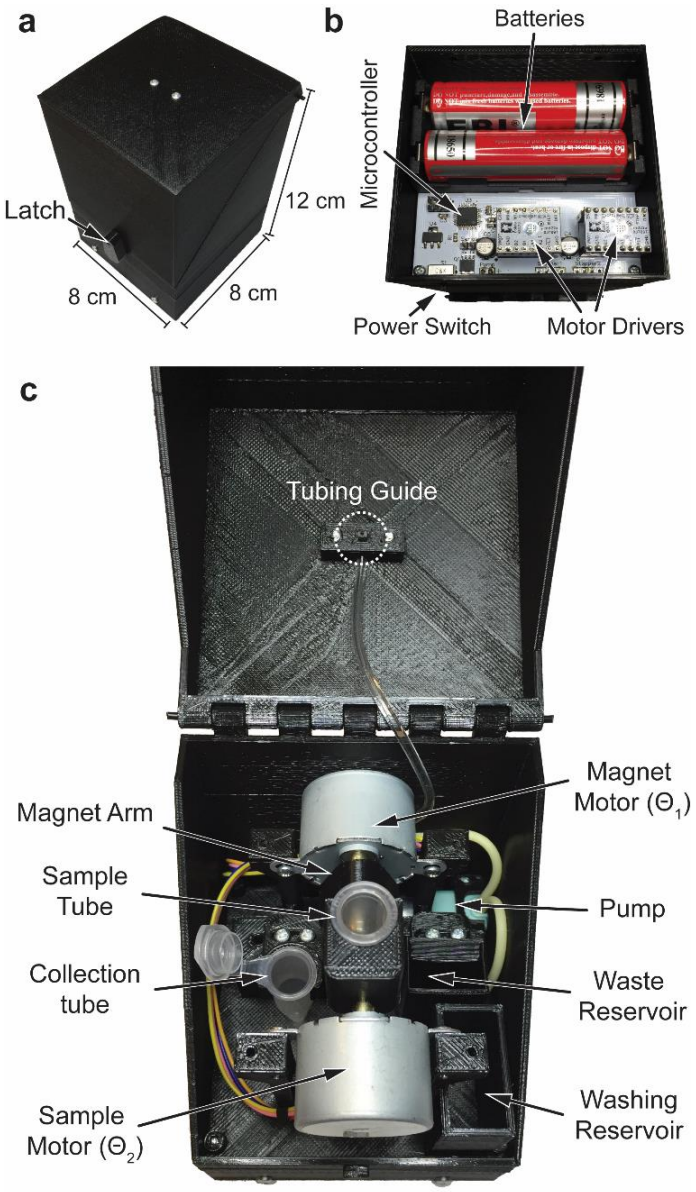


Figure 6.2. Photographs of the completed sample preparation device. (a) The device with its lid closed, viewed from the front. (b) The bottom of the device with the lower cover removed, showing the circuit board and batteries for controlling and powering the device. (c) The device with the lid opened, viewed from the top. This shows the locations of integrated functional components, including the motors responsible for rotating the sample tube and magnet arms, as well as the pump and washing reservoir for delivery of washing buffer to the sample tube. © 2018 RSC

microcontroller and supply power from the batteries to the motor coils. The peristaltic pump is controlled by the microcontroller using a MOSFET to turn on or off the DC motor on the pump.

### 6.3.2 Electronic and mechanical materials

The device is designed using filament-based 3D printing with polylactic acid (PLA) plastic as the filament. PLA was sourced from Hatchbox (Los Angeles, CA). Stepper motors (SKU 918) were sourced from Adafruit (New York, NY). The peristaltic pump (SKU RP-Q1.2N-P20A-DC3V) is from Aquatech (Osaka, Japan). All electronics were ordered from DigiKey (Thief River Falls, MN) except for the stepper motor controllers (item no. 2134) which were sourced from Pololu (Las Vegas, NV). The printed circuit board (PCB) was fabricated by PCBway (Hangzhou, China). The 18650 batteries were from EBL (China). Tubing (part no. ACF00001) was from Saint-Gobain (Paris, France).

### 6.3.3 Experimental setup

Because this project involves a new type of device, two different phases of experimentation are performed. The first phase involves qualification and optimization of the design itself, and the second phase involves testing the effectiveness of the sample preparation using the optimized design. These two phases will be explained in detail in the following sections.

#### 6.3.3.1 Design optimization experiments

Initially, the effectiveness of pouring is studied to minimize residual liquid after pouring due to surface tension. In order to quantify the effectiveness of pouring, the mass of the tube is measured before loading the sample, after loading the sample, and after pouring out the sample. The sample used for this test is 900 ml of water. The tube is then placed in the device which pours the tube's contents by rotating the tube motor. After returning to the home position, the mass of the tube is measured again. The difference between this value and the previously measured mass indicates the amount of residual water that is not effectively removed from the tube by the pouring process due to surface tension. This experiment is performed using conical-bottomed and round-bottomed tubes to study the effect of the tube's shape on supernatant removal. The effectiveness of the automated

magnetic bead separation is also studied for the optimization of the device. Because the magnetic beads retain DNA within the sample tube while the supernatant is being removed, the effective retention of the magnetic beads translates to effective isolation of DNA from the sample. To perform this experiment, a tube containing 200 ml of suspended magnetic bead mixture is placed in the device with the magnet in the upward position ($\theta_1 = 180°$). Next, the device's magnet is moved to the downward position ($\theta_1 = 0°$) using the magnet motor, and the magnetic beads are attracted toward the tube's wall for 30 seconds. After 30 seconds, the tube motor and magnet motor simultaneously rotate to position the sample tube and the magnet for pouring. The supernatant is poured into a separate waste tube. The device then returns the tube to the home position and the magnet to the upward position. It then resuspends the magnetic beads in 200 ml of water by operating the peristaltic pump.

#### 6.3.3.2 Sample preparation experiments

In a laboratory setting, the gold standard sample preparation methods are magnetic bead-based DNA separation and silica filter-based DNA extraction. The automated DNA extraction using the proposed device is compared with the two gold standard methods for DNA isolation yield. Each of these methods rely on whole human blood which is spiked with foreign DNA. For testing purposes, spiked whole blood with mouse DNA containing SOX2 gene is used to reduce the risk of infection to the researchers. Methods relying on magnetic bead DNA isolation protocol, both automated DNA extraction as well as manual DNA extraction, are carried out as described by the DynaBeads DNA DIRECT Blood user guide. Initially, 100 ml of DNA-spiked whole human blood is placed into a 2 ml round-bottomed tube. 1ml of chilled (-20 °C) Red Cell Lysis Buffer is added to the tube and the solution is allowed 5 minutes for lysis to complete at room temperature. The tube is occasionally agitated for thorough lysis. Once lysed, the tube is centrifuged at 8000 RPM for 2 minutes which

forms a pellet on the bottom of the tube. The supernatant is then carefully removed and 200 ml of well-mixed magnetic bead suspension is added. This mixture is now allowed to incubate at room temperature for 5 minutes, allowing DNA to attach to the beads. The protocol then diverges between the manual and automated methods. For the manual method, the tube is placed on a holder containing the same magnets used in the machine. The tube is allowed to sit for one minute allowing the magnet to attract the beads to the wall of the tube. After one minute, the supernatant is carefully pipetted out by hand and discarded. Next, 1 ml of washing buffer is quickly pipetted into the tube in a way that washes the magnetic beads off the tube wall. The tube is then placed back onto the magnet and the process is repeated two times, giving a total of three washing–separating–resuspending cycles. After this, the beads are again pulled to the wall and the supernatant is discarded. For the automated method using our sample preparation device, the device is first prepared by adding 3 ml of washing buffer to the reservoir. The sample tube is then placed into the device which is subsequently turned on. Once activated, the device brings the magnet to the upward position and simultaneously begins swinging the sample tube so that gentle mixing is performed for one minute. Next the tube is brought to home position and the magnet is brought to the downward position, allowing the magnetic beads to move to the tube wall. After 30 seconds, the magnet and tube rotate to discard the supernatant by pouring. The tube then returns to the home position, the magnet to the upward position, and the peristaltic pump is activated to pump 900 ml of washing buffer into the tube. After resuspension, the cycle repeats for a total of three washing– separating–resuspending cycles. The final resuspension does not take place, and the device simply returns to the home position, allowing for the user to easily remove the sample tube, which at this point contains only magnetic beads still attached to the wall. For both the manual and the automated magnetic bead protocols, the user adds 200 ml of resuspension buffer to the tube to wash the beads from the wall. The sample tubes are incubated at 65 °C for 5 minutes,

this incubation elutes the DNA from the magnetic beads. After elution, the tubes are placed on the magnet for 1 minute to pull the beads to the tube wall. The supernatant is then collected and transferred to new clean PCR tubes for qPCR quantifications. For each experiment, the $C_t$ of the captured DNA sample is subtracted from the $C_t$ measured from the positive control, to result in $\Delta C_t$. $\Delta C_t$ reveals the ratio of DNA between the positive control and the captured DNA from each respective method. For the silica filter-based isolation protocol, the process is conducted based on the QIAamp DNA Blood Mini Kit user guide. The first step to carry out this process is to pipette 20 ml of protease K in a 1.5 ml tube. The use of the protease is necessary in order to breakdown proteins in 200 ml of the sample, DNA spiked-human blood. Also, 200 ml of lysis buffer is added. The tube is agitated to thoroughly allow efficient lysis before incubating it for ten minutes at 56 °C and centrifuging to remove the evaporated drops. Next, to enhance the binding of the DNA to the silica, 200 ml of ethanol is mixed in. Afterward, the solution is pipetted into a spin column to centrifuge for one minute at 8000 RPM. During this step, DNA binding to silica occurs. The process repeats with 500 ml of washing buffer, which is centrifuged at 8000 RPM for one min, followed by another 500 ml of washing buffer, which is centrifuged at 14000 RPM for three minutes. After each time a spin column is used and centrifuged, the collection tube is discarded and replaced with a new one. Multiple washes ensure that the DNA is purified. After discarding the collection tube, the tube is then centrifuged again for one minute to guarantee complete liquid removal. After transferring the spin column into a 1.5 ml tube, 200 ml of elution buffer is added before centrifuging one more time. This step weakens the binding of DNA to the silica filter and elutes DNA into the elution buffer.

#### 6.3.3.3 PCR experiments

Each experiment proving the validity of the sample preparation device are run using qPCR. Three sets of experiments: manual magnetic bead method, automated magnetic bead method, and

silica filter method, are run using a conventional qPCR machine (7900HT Fast Real-Time PCR System, Applied Biosystems, Foster City, CA). PCR reagents are from VitaNavi Technology (Ballwin, MO) with a TaqMan probe that targets mouse SOX2 gene from Applied Biosystems (Waltham, Massachusetts). Target DNA was sourced from ABM (Vancouver, Canada). Human blood was supplied by Zen Bio (Research Triangle Park, NC). The DynaBeads DNA direct blood kit by Invitrogen (Carlsbad, CA) was used for magnetic bead experiments. For silica bead experiments, the QIAamp system by Qiagen (Hilden, Germany) was used. The presented device is also tested in conjunction with a 3D-manufactured qPCR device described previously[24]. For PCR reactions, each well, or tube (for reactions ran with the 3D-manufactured qPCR machine) are prepared as follows: 6 ml of PCR grade water, 10 ml of PCR mix, 1 ml of polymerase, 1 ml of TaqMan, and 2 ml of the desired sample. For PCR reactions performed in the 3D-manufactured qPCR device, an additional 20 ml of mineral oil is added to prevent evaporation of the reagents during thermocycling. The product length of the qPCR is measured by using a gel electrophoresis. A 3% agarose gel with a channel length of 100 mm is ran at 75 V for 2 hours (50 ml of 1× TBE, 1500 mg agarose powder and 5 mL of 10000× SYBR safe gel stain).

## 6.4 Results and Discussion

The comparison of pouring effectiveness between conical-bottomed tubes and round-bottomed tubes is shown in Figure 6.3. Rotating the tube motor by 128° results in a reliable pouring of bulk fluid from the bottom of the tube (Figure 6.3a). Steeper angles do not achieve any observable improvements in fluid removal. The residual liquid is quantified by subtracting the weight of the tube before ($w_{water}$) and after ($w_{poured}$) pouring. In Figure 6.3b, the effectiveness of pouring is plotted in percentile using eqn (6.1).

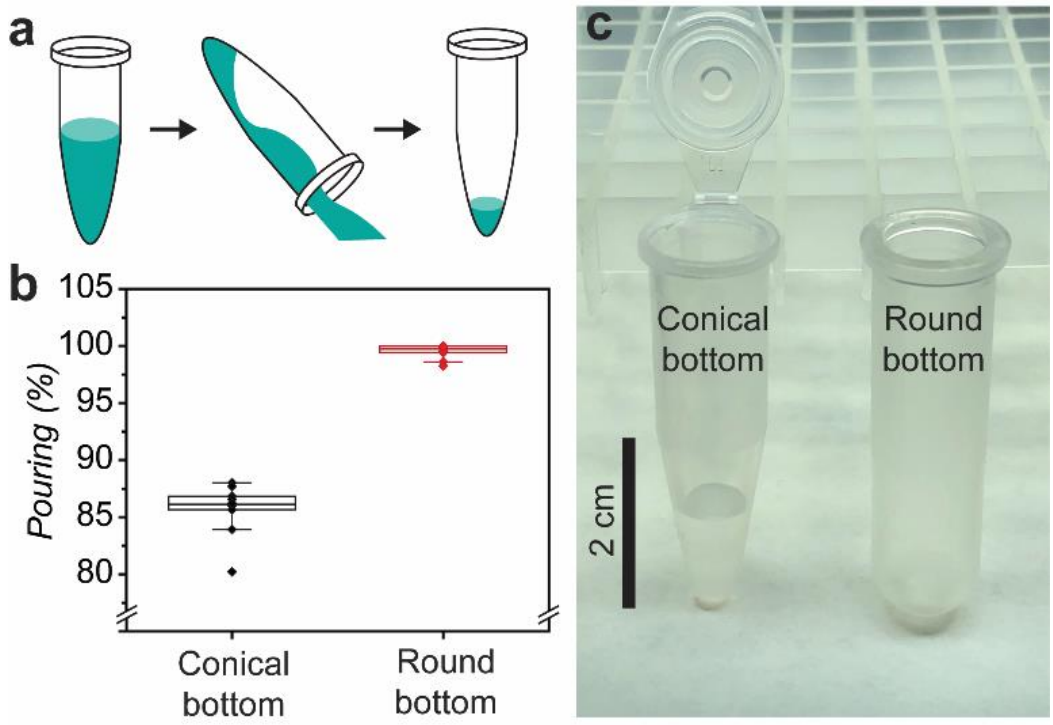


Figure 6.3. The effective removal of liquid using conical-bottomed tube and round-bottomed tube. (a) A tube is used to pour out the water and remaining liquid due to surface tension is measured. (b) The pouring efficiency comparison between the conical-bottomed tube, 85.7 ± 0.67% (SEM), and round-bottomed tube, 99.52 ± 0.19% (SEM). (c) The photograph of two tubes after pouring out water showing retained water in the conical-bottomed tube. © 2018 RSC

$$Pouring\ \% = \frac{w_{water} - w_{poured}}{w_{water} - w_{tube}} \tag{6.1}$$

With conical-bottomed sample tubes, the pouring method yields 85.7% (with the standard error of the mean (SEM) ± 0.67%) removal of water and the use of round-bottomed sample tubes yields effective removal of 99.52% (with SEM ± 0.19%). Each experiment is repeated for 10 times ($n$ = 10). The retention of water in the conical-bottomed tube is due to the water's adhesive force in the narrow conical bottom, supporting the weight of water in the presence of gravity. The round bottom forms much less overall adhesive force, resulting in an effective removal of water in the tube by simple pouring (Figure 6.3c). The automated sample preparation device is constructed with the pouring scheme

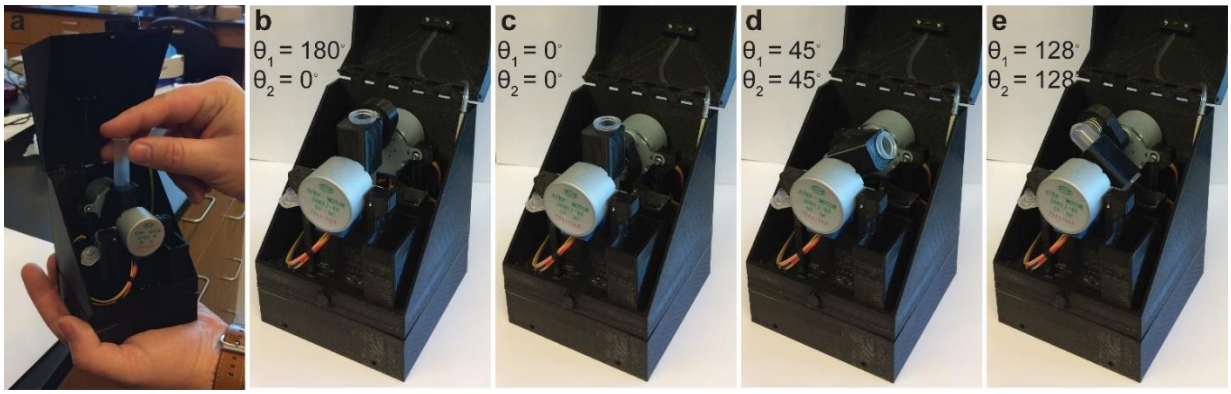

Figure 6.4. The automated handheld device which can perform magnetic bead-based sample preparation using two simple θ motions. (a) The insertion of the sample into the device, (b) the initial (home) position, (c) the engagement of magnet ($\theta_1 = 0°$) to start the magnetic bead separation, (d) simultaneous rotation of both motors ($\theta_1$ and $\theta_2$) to initiate pouring, and (e) the pouring position ($\theta_1 = \theta_2 = 128°$). © 2018 RSC

to perform the magnetic bead-based separation (Figure 6.4). The handheld device is completely portable, and battery operated. The internal batteries (3000 mA·h) have enough capacity to power the stepper motors continuously for 13 hours, giving ample battery life for many sample preparations on a single charge. The device is operated by inserting the sample in a round-bottomed tube (Figure 6.4a). The device's power is turned on by sliding the power switch (Figure 6.2b). Initially, the motors are in a home position ($\theta_1 = 180°$, $\theta_1 = 0°$, Figure 6.4b). By rotating the magnet motor ($\theta_1 = 0°$), magnetic separation can be started (Figure 6.4c). For pouring, both motors turn to 128° (Figure 6.4d and e). The combination of motions tested above can perform the sample preparation autonomously. The effectiveness of the separation and pouring is tested. To visualize the functionality of the device, a copy of the device without the enclosure is used (Figure 6.5). A sample round-bottomed tube with 200 ml of magnetic beads is inserted into the test device. After the magnet engages near the tube, the suspended beads are separated and accumulated on the tube's wall (Figure 6.5a). Afterwards, the magnet and tube motors rotate to 128° to pour the supernatant liquid (Figure 6.5b). The washing step

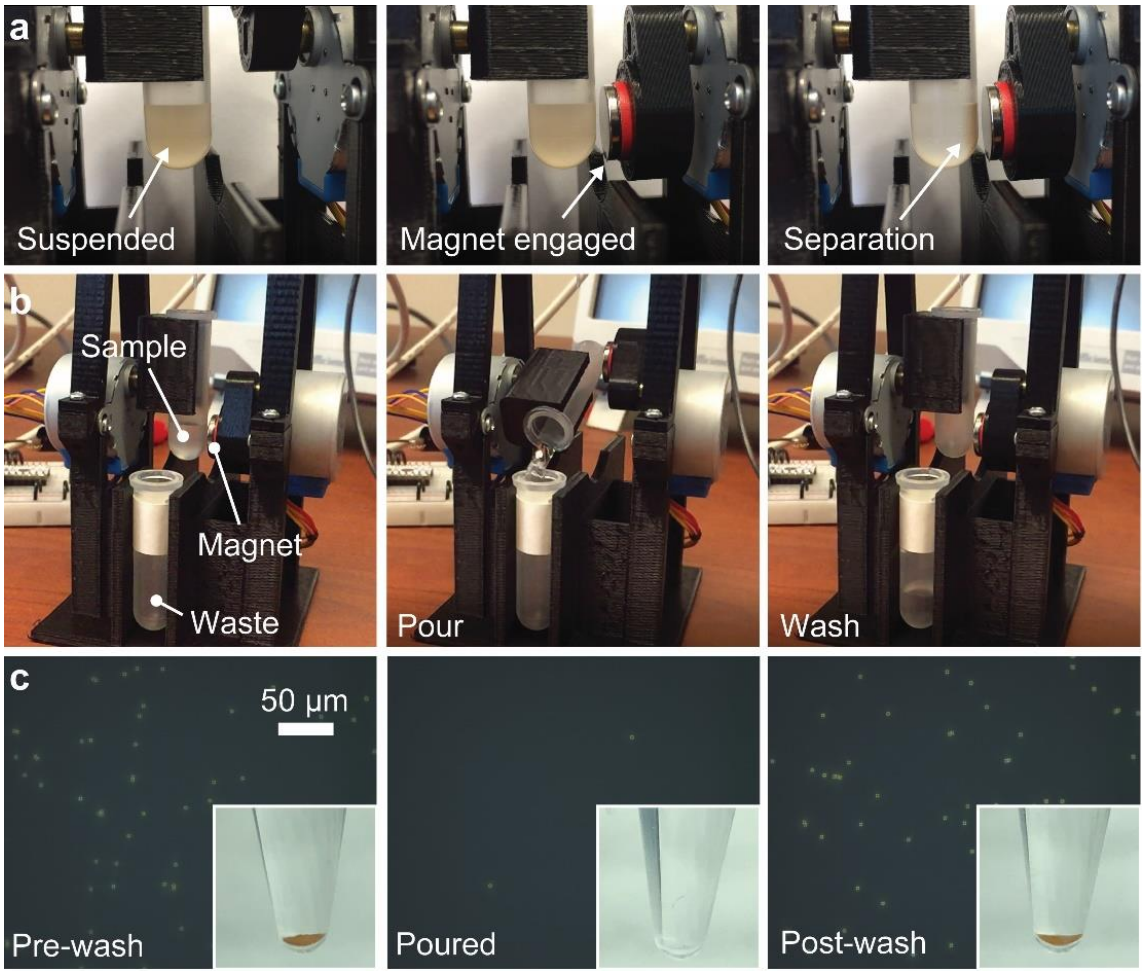


Figure 6.5. The photographs of the magnetic bead separation and pouring method. (a) The suspended magnetic beads in the tube are attracted toward the magnet once the magnet engages into position. This results in an accumulation of magnetic beads on the tube's wall. (b) To remove the supernatant liquid for washing steps, both motors for the tube and magnet simultaneously rotate. (c) The microphotographs of pre-wash, poured, and post-wash liquids to show an effective retention of magnetic beads in the tube after washing and pouring. © 2018 RSC

is performed by dispensing washing buffer into the tube, which causes a resuspension of the magnetic beads. The original (prewash) sample, the supernatant (poured) sample, and the resuspended (post-wash) sample are inspected under a microscope (Figure 6.5c). As expected, the poured sample contains few magnetic beads and the post-wash sample contains a comparable amount of beads to the pre-wash sample. This experiment demonstrates a successful pouring, removing the supernatant liquid without significantly disturbing the separated beads. The DNA capture efficiencies of the developed

device, manual magnetic bead-based separation, and silica filter-based DNA extraction are compared (Figure 6.6). For each of the extraction methods, qPCR is performed to determine the $\Delta C_t$, which can be correlated to the ratio of concentrations between the original DNA samples before the extraction and the extracted DNA samples. The automated method on average resulted in a deviation from the positive control by 2.872 cycles with a SEM of 0.262 cycles, the manual magnetic bead experiments deviated by 5.988 cycles with a SEM of 0.764 cycles, and the silica filter method deviated by 5.756 cycles with a SEM of 0.077 cycles ($n$ = 5 for each method). Each $\Delta C_t$ can be interpreted as 13.7%, 1.58%, and 1.85% for automated, manual, and silica-filter-based methods, respectively. These yields are low considering that each PCR cycle signifies a 2× amplification. However, due to the short length of the target used in this experiment (68 bp) this is expected as these DNA purification techniques are generally not optimized for such short DNA fragments, which is consistent with previously reports of less than 10% recovery for DNAs with shorter than 75 bp [142]–[144]. Consequently, the most important metric by which to evaluate the effectiveness of the automated method is in comparing it directly with other methods that use the same target. This data suggests that the automatic sample preparation method has a higher DNA capture yield than performing the same operation manually or by using an alternative method such as a silica filter for this length of DNA. This study does not guarantee an increased yield of any DNA length. However, it is likely to result in a comparable yield to the manual magnetic bead-based separation because the fundamental mechanism for capturing DNA is identical. In Figure 6.6, each bar represents data from each of the methods. The increased yield (lower deviation from the positive control) of the automated method is clearly evident. One possible explanation for the increased yield is the effectiveness of the pouring motion for supernatant removal and reduced risk of disturbing the bead cluster while removing the

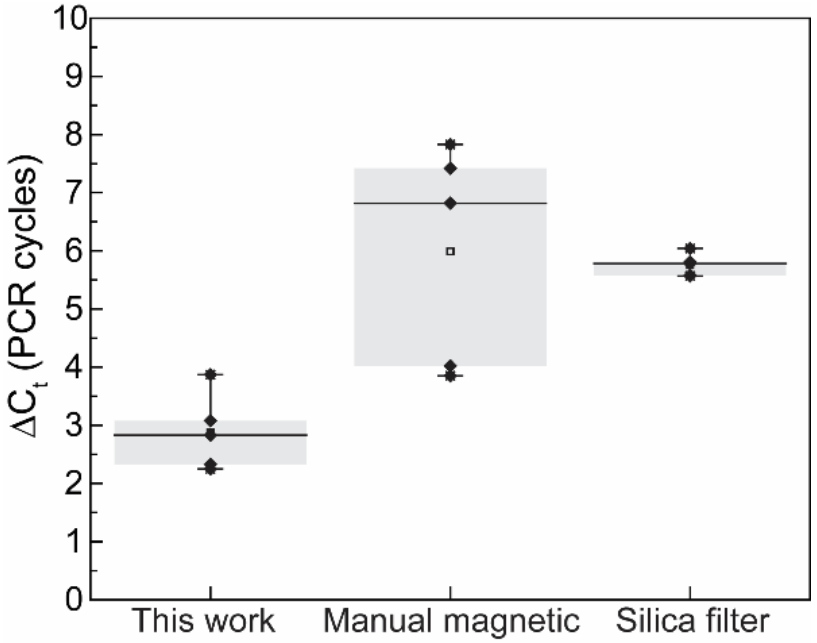


Figure 6.6. The comparison of DNA capture yields between automated, manual magnetic bead-based separation, and silica filter-based DNA extraction (n = 5 for each method). Deviations ($\Delta C_t$) from the positive control is 2.872 ± 0.262 (SEM), 5.988 ± 0.764 (SEM), and 5.756 ± 0.077 (SEM). The low $\Delta C_t$ level of the automated method indicates an efficient DNA capture compared to that of gold standard methods. © 2018 RSC

supernatant liquid, an advantage that is unique to this device. Additionally, the pouring motion allows for a contactless sample preparation protocol with fewer components requiring replacement between samples. The contactless nature of the device also reduces the risk of contamination compared to other devices due to the reduced number of possibly contaminated components that come in contact with the sample. Although the sample is exposed to the air, it has been found that air is rarely the source of PCR contaminants [145]. In order to determine the lowest number of DNA copies the presented device is capable of capturing, a blood sample containing different number of DNA copies ($9.6 \times 10^5$, $9.6 \times 10^4$, and $9.6 \times 10^3$) is processed using the automated sample preparation device and detected using the conventional qPCR. The average $C_t$ for each sample is 28.07 ± 0.54, 33.00 ± 0.14, and 33.90 ± 0.16, respectively. Between $9.6 \times 10^5$ and $9.6 \times 10^4$ samples, the $C_t$ values are significantly different, however, reducing the sample below $9.6 \times 10^4$ did not result in a noticeable change. Thus,

the extraction limit is on the order of $10^4$ DNA copies. The novelty of the system is to be able to operate complicated sample preparation tasks outside of a laboratory setting where tools, such as pipettes, are not readily available. We have previously reported a 3D-manufactured qPCR device which is also battery operated and a handheld device [24]. The combination of two presented devices (Figure 6.7a) creates a unique opportunity in point-of-care (POC) diagnostics by minimizing the user's involvement in performing a high-quality qPCR-based diagnosis of infectious diseases. To test this, samples are prepared using the automated magnetic bead sample preparation device and analyzed with the 3D-manufactured qPCR device from a previous study [24]. This experiment begins with a concentrated DNA sample (1×) that is diluted 10 times (0.1×) and diluted 10 times again (0.01×). The concentrated and two diluted DNA samples are used to spike 100 ml of blood used in the experiments. The qPCR measurements from the 3D-manufactured device are shown in (Figure 6.7b). $C_t$ values of the 1×, 0.1×, and 0.01× samples are 24.90, 28.57, and 32.33, respectively. Each dilution is separated by 3.67 and 3.76 cycles, which closely matches the ideal separation of 3.33 cycles between 10× dilutions. To confirm the amplification of the correct target DNA, a gel electrophoresis is performed (Figure 6.7c). The result shows a band near 70 bp indicating the amplification of target gene. The byproducts of TaqMan probe are also visible as expected [24], [128]. This experiment reveals the devices' robust operation and consistent DNA extraction as well as a portable handheld system that comprehensively performs qPCR measurements. qPCR allows for not only a positive/negative diagnostic result, but a quantitative one as well. This will aid in determining the proper treatment when used to diagnose an infection.

## 6.5 Conclusion

This work has demonstrated the effectiveness of an automated sample preparation device that is capable of extracting DNA used for PCR reactions from whole blood samples. In fact, the device

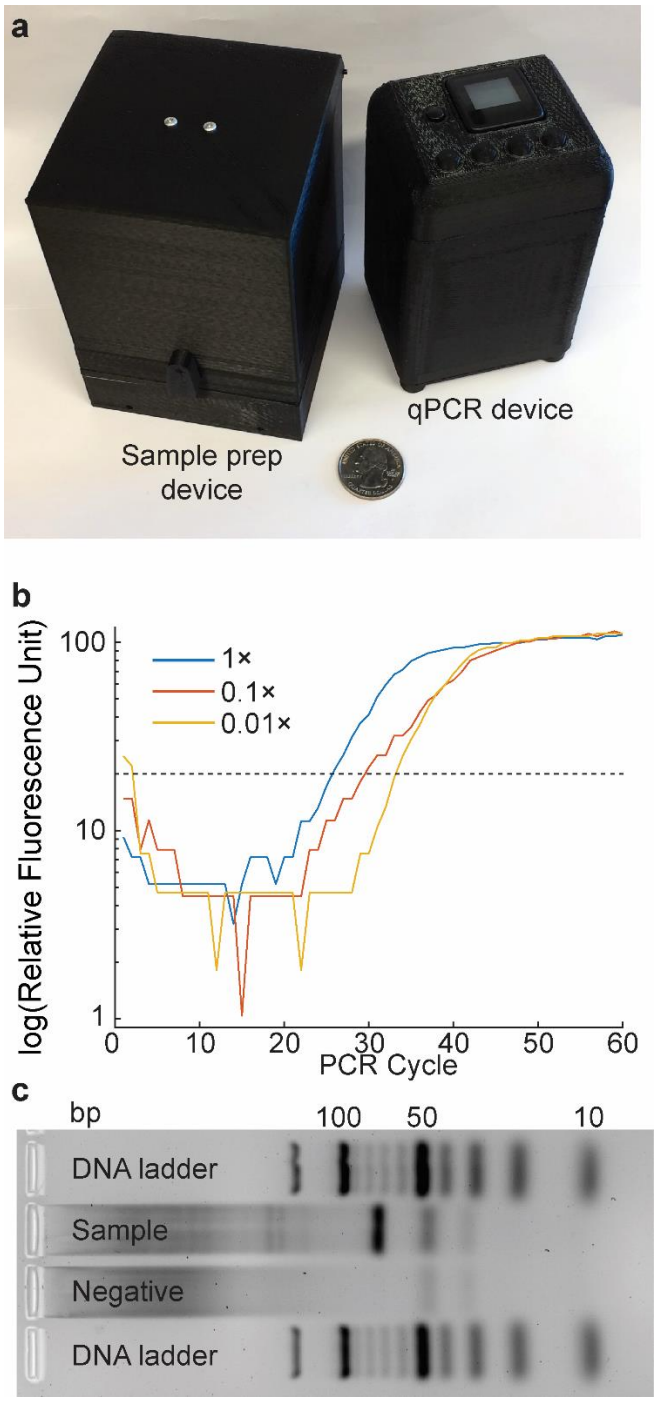


Figure 6.7. (a) A comprehensive, portable, battery-operated diagnostic system using the automated sample preparation device and 3D-manufactured qPCR device. (b) Fluorescence reading, in logarithmic scale, from the handheld qPCR device for three different concentrations of target DNA spiked in whole blood. For 1×, 0.1×, and 0.01× samples, Ct values are 24.90, 28.57, and 32.33, respectively. (c) Gel electrophoresis of the qPCR product, confirming a 68-bp band. © 2018 RSC

has been proven to result in a higher DNA yield than other common methods, which will result in a lower minimum detectable level of infection using qPCR. It has also shown the effectiveness of the isolated DNA sample when used with the authors' portable real-time qPCR machine. The work demonstrated a crucial step toward producing an autonomous nucleic acid testing method using qPCR, a gold standard test for many infectious disease diagnoses. However, a few of the steps, such as adding the magnetic beads and lysis buffer with the blood into a tube as well as adding qPCR reagents into the purified DNA, still require user's handling. For future work, we are actively working toward integrating every step involved in qPCR based diagnostics. For mixing magnetic beads and lysis buffer, two options are possible: (1) a pre-loaded tube with beads and lysis buffer, and (2) additional dispensers in the device. Additionally, qPCR reagents have a short shelf life at room temperature and thus cannot reliably be stored in liquid form. Lyophilization can be used to aid in storage, and is proven to elongate the shelf life of chemicals and drugs [146].

### 6.5.1 Conflicts of interest

The authors declare no competing financial interests.

### 6.5.2 Acknowledgements

The authors thank the graduate research assistantship support from the Office of Research and Commercialization (ORC) at the University of Central Florida (UCF) for an ORC Doctoral Fellowship. We also acknowledge the partial support from the Office of Undergraduate Research (OUR) at UCF for an OUR Student Research Grant. Human whole blood was purchased from Zen-Bio Inc.

# CHAPTER 7: INTEGRATED MICROFLUIDICS FOR SYRINGE TO SIMPLIFY NUCLEIC ACID DETECTION

## 7.1 Chapter Notes

This chapter presents another sample preparation device to remove the requirement of a skilled lab technician to perform a medical diagnostic. The inspiration for this device is the multi-ganged rotary switch that is commonly found in vintage radios or other 20th century electronic devices. Here, the complicated sample preparation procedure is mapped out into a flattened schematic view where all reagent reservoirs, the needle, the sample collection tube, and the syringe vacuum source are presented. This schematic was optimized to minimize the number of valves required for a full sample preparation process. The scheme is then implemented in a 3D printed cylinder-shaped syringe complete with internal chambers, valves, and reservoirs to implement the sample preparation process. This device fully removes all the steps of the sample preparation process from the operator, requiring only that the operator can pull on the plunger of a syringe and rotate the valve for each step. No pipettes are required, and no chemical reagents are needed other than what is pre-loaded into the syringe to extract and purify nucleic acids from drawn blood. The resulting purified sample is ready to use in a downstream PCR reaction as demonstrated in this paper. This paper is co-authored by Fabrice Lamour and Brian N. Kim and is currently awaiting peer review.

## 7.2 Introduction

The prevalence of outbreaks of infectious diseases across the world such as Zika virus and SARS-CoV-2, emphasizes the need for diagnostic procedures that are rapid and accurate [147]–[150]. Quantitative polymerase chain reaction (qPCR) can be used to diagnose infectious diseases with a high degree of accuracy [22], [151]. qPCR utilizes specially designed primers to amplify specific target

nucleic acid sequences to a detectable level. This is helpful in acute-care diagnostic settings, as viral nucleic acid sequences are present in low levels in patient samples (such as blood).

However, qPCR is often not the first diagnostic technique used in an acute care setting due to its time-consuming, labor-intensive sample preparation process. The procedure must be carried out at a specialized laboratory, which may take days due to the transportation of the patient sample and the required skilled labor. This is contrasted with rapid methods such as antigen tests which only require minutes to complete, but usually have lower accuracy, sometimes requiring multiple tests to confirm the presence of a viral infection as well as the inability to quantify the stage of infection. A low-cost and simplified diagnosis via PCR would aid public health by bringing higher quality and higher accuracy diagnostics to more patients.

A significant challenge of developing a simple PCR-based diagnostic tool is the complex sample preparation step [130]. Sample preparation from whole blood involves a large amount of manual pipetting steps to isolate nucleic acids, which include the lysis of blood cells, isolation of DNA/RNA, washing, and final elution; additionally, specialized equipment such as spin columns and centrifuges must be utilized. This complex process is typically performed by a trained individual in a laboratory, thus rendering it unsuitable for rapid disease detection in a clinical setting [131]. Therefore, there is a demand to move in the direction of simplified sample preparation tools, requiring little to no skill to use. There have been recent numerous proposed approaches to simplified sample preparation [131], [133], [134], [136]–[140], [147], [152]. An integrated microchip module was developed to isolate blood cells and release their DNA for qPCR amplification [153]. This approach, however, requires complex manufacturing which is not ideal for accessibility and maintaining a low cost. Automated whole blood sample preparation systems are available; however, they have the

disadvantage of being relatively large and expensive, while also requiring large amounts of reagents and sample [154].

To solve the challenges of production and cost, an integrated microfluidic approach is more suitable. An integrated microfluidic system has the advantage of utilizing minimal amounts of reagents and samples, as well as reducing cross-contamination due to the entire process being performed in an enclosed system [153]. Additionally, microfluidic systems have the ability to be 3D-printed, thus lowering the cost of production and allowing for more rapid sample analysis. In the medical field, 3D printing has attracted much interest, especially in the area of microfluidics [23], [24], [155], [156]. The application of microfluidic systems in medicine includes the development of inertial cell sorting systems, multiplexed bio-assays, lab-on-a-chip diagnostic methods, and cytometry [153], [154], [157], [158]. 3D printing has emerged as a valuable production technique of these microfluidic systems as traditional fabrication techniques such as soft lithography, laminates, and injection molding are time-consuming, high-cost, complex, and low resolution [156], [159]–[161]. Stereolithography printing (SLA) is a process in which 3D structures are created layer by layer through the polymerization of a resin (through the utilization of ultraviolet light) and has the advantage of being rapid, high resolution, and relatively inexpensive compared to traditional fabrication methods. SLA is especially useful in its ability to produce parts with completely blind orifices and chambers that are non-machinable. High resolution is imperative when considering the use of 3D printing for microfluidic complexes, and SLA 3D printers provide a layer height of approximately 25 microns, compared to fused deposition modeling 3D printers (FDM) which have a maximum practical resolution of approximately 100 microns.

In this paper, we introduce a novel single-use, 3D-printed microfluidic syringe that performs integrated whole-blood sample preparation, with minimal training required to use and potential for

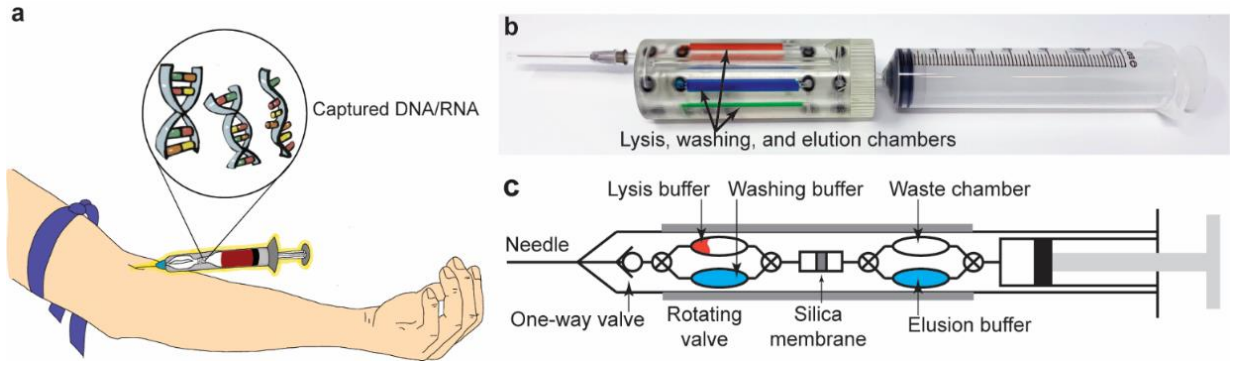


Figure 7.1. Integrated syringe for rapid nucleic acid extraction. (a) Conceptually, the integrated syringe can extract nucleic acid as blood is drawn. (b) The integrated syringe loaded with coloring to visualize the 3D microfluidics. (c) A simplified diagram of the integrated syringe.

rapid mass production. Because the sample preparation procedure is a complex protocol with several steps involved, a robust method to integrate complex fluidic channels and valves is investigated. A typical whole blood sample preparation procedure has five distinct steps. Step one is drawing blood from a potentially infected patient. The whole blood contains many PCR inhibitors which must be destroyed or disabled before a reaction can be performed. Step two is the lysis of the blood cells. This step decreases the viscosity of the blood, decreasing the likelihood of clogging the silica membrane. It also creates the correct chemistry in the sample for the following step, binding. In the binding step, the sample is passed through a silica-based membrane. The silica attracts the nucleic acids by electrostatic forces and binds them to the membrane while allowing other materials to pass through. Some undesired materials remain on the filter which are removed by the washing step. Washing removes most of the remaining contaminants from the silica membrane while maintaining the binding of the nucleic acids. Finally, the sample is eluted from the membrane, resulting in a purified sample.

## 7.3 Results and Discussion

To develop a low-cost solution that can process samples without complicated processes and manual labor, we have developed an integrated syringe that implements all the steps involved in a typical whole blood nucleic acid sample preparation by integrating fluidic channels and rotary valves.

The syringe relies on fluidic reservoirs and pathways that are interconnected via multi-way rotary valves to simplify the silica-based nucleic extraction method.

### 7.3.1 Fluidic schematic

The integrated syringe's fluidic system is composed of an outer barrel and inner valve (Figure 7.2a), which are both 3D microfluidic devices fabricated using a stereolithography (SLA) 3D printer. The inner valve body is designed so that it can rotate against the outer barrel into multiple positions. The rotation allows the switching of fluidic connections, effectively behaving as rotary valves. To aid in visualization and design, we have developed a 2D map for the 3D microfluidic arrangements (Figure 7.2b). The syringe is designed to replicate every step of the benchtop sample preparation protocol required for RNA and DNA. The outer barrel design has 5 possible positions for the inner valve ($\theta$ = 0°, 72°, 144°, 216°, and 288°). Each position serves a specific function in nucleic acid purification steps.

For the draw and lysis of the blood sample, the inner valve is positioned at $\theta$ = 0° (Figure 7.2c). In this position, the sample flows in through the needle and enters the lysis reservoir. The lysis reservoir is prefilled with lysis buffer, which mixes with the blood sample. For binding, the inner valve is positioned at $\theta$ = 72° (Figure 7.2d). In this position, the silica filter in the inner valve is aligned to the lysis reservoir. The vacuum from the plunger pulls the fluid through the silica filter into the waste reservoir. During this step, nucleic acids present in the lysed sample bind to the silica filter. After binding, the inner valve rotates to $\theta$ = 144° (Figure 7.2e) to align the silica filter with the washing reservoir. The syringe's vacuum pulls the washing buffer through the silica filter and deposits it along with the lysed blood remnants in the waste reservoir. This step ensures that any contaminants from the blood and lysis buffer present in the silica filter are removed and the sample is clean. For elution,

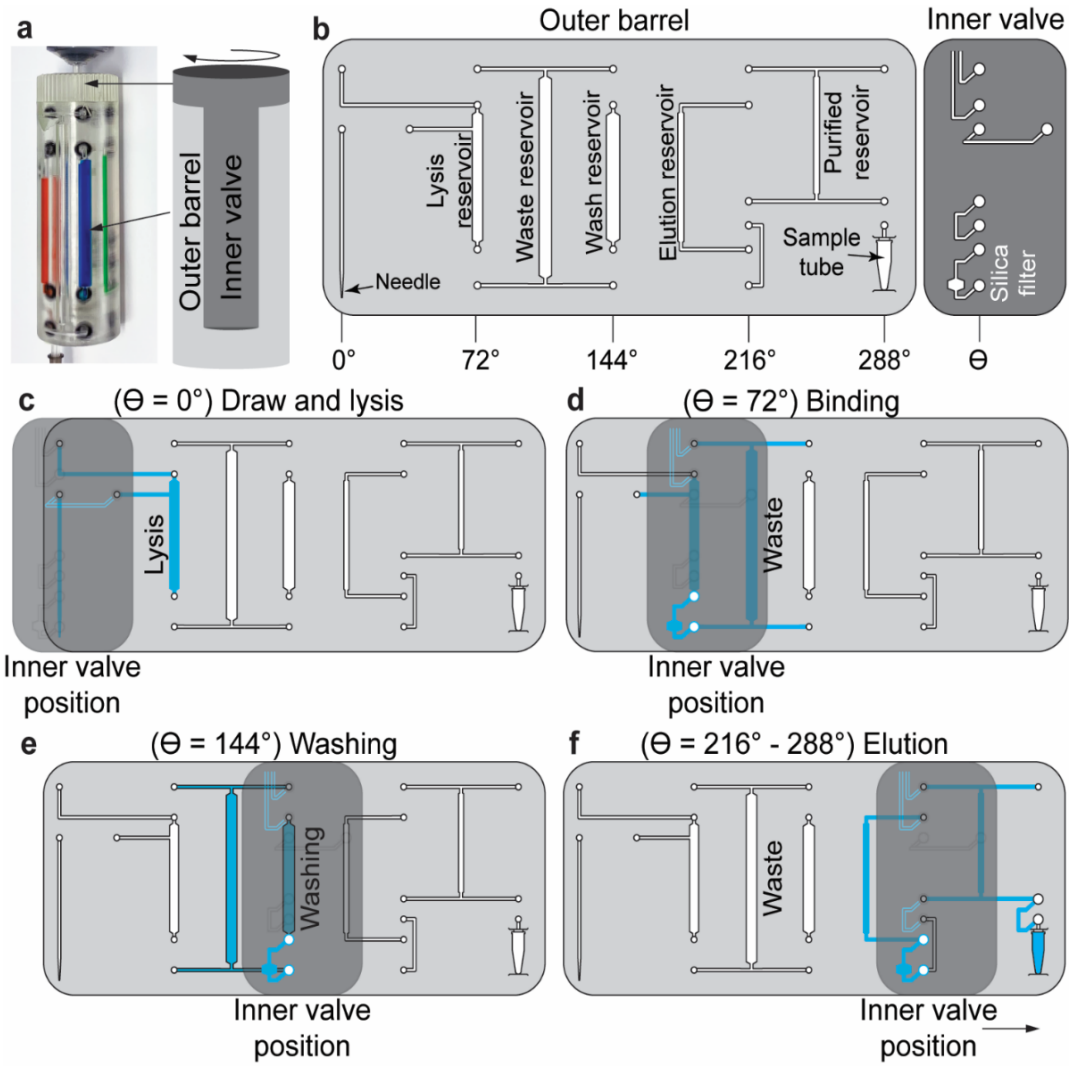


Figure 7.2. The integrated collect-purify syringe fluidic map. (a) The integrated syringe is made of two parts, an outer barrel and inner valve. The inner valve can rotate against the outer barrel, serving as a rotary valve for integrated microfluidics. (b) 2D fluidic map for the integrated syringe. The light gray section shows the chambers in the outer barrel, while the dark gray shows the inner valve which contains the silica filter. (c-f) The rotation of the inner valve changes the relative angular position of the inner valve against the outer barrel, allowing the operation of each step of the nucleic acid extraction process.

the inner valve rotates to $\theta = 216°$ (Figure 7.2f) which connects the elution reservoir to the silica filter. First, the elution buffer runs through the silica filter, eluting nucleic acids and pulling them through to the purified reservoir. The inner valve rotates to $\theta = 288°$, and the eluted nucleic acids contents

within the purified reservoir are ejected from the integrated syringe into a sample tube/cartridge. The entire process of nucleic acid purification is complete.

### 7.3.2 Multi-way rotary valve design and fabrication

The multi-way rotary valves are the main mechanism by which the integrated syringe's functionality is achieved. They serve to provide a means to connect the different reservoirs of reagents, the syringe, and the sample tube to the silica membrane for the sample preparation step where each component is required. Because of this, their design and function are critical for the operation of the integrated syringe to be successful. Figure 7.3 shows how the valves operate. The cross-section of the valve in Figure 7.3a shows the relationship between the inner valve body and the several channels around the outer barrel. Nitrile O-rings are used to seal the gaps between the inner valve body and the outer barrel, while also allowing for rotation. The shape of the O-ring groove is of critical importance in holding the O-ring in place when the inner valve body is removed, allowing enough compression of the O-ring to provide sealing against leaks, while also maintaining a low enough grip on the inner valve body so it can rotate to select the different positions on the valve. Notice that O-rings are held in position even with the inner valve body removed and being unsupported against gravity. The O-ring groove is shaped so the O-rings can be held in place for ease of assembly of the integrated syringe. SLA 3D printing enables the complicated O-ring groove to be manufactured in place with no issues. Figure 7.3b shows a close-up of an O-ring sitting slightly proud of its groove. The O-ring is lubricated with a silicone-based grease which decreases friction so the inner valve body can freely slide across the O-ring while maintaining a watertight seal. Figure 7.3c-d shows a 3D CAD drawing of how the rotary valve mechanism functions. In Figure 7.3c, the blue path highlights the channel that is created from one channel in the outer barrel, through the upper-left O-ring seal, and into the inner valve body. The other four O-rings are pressed against the inner valve body as well, but

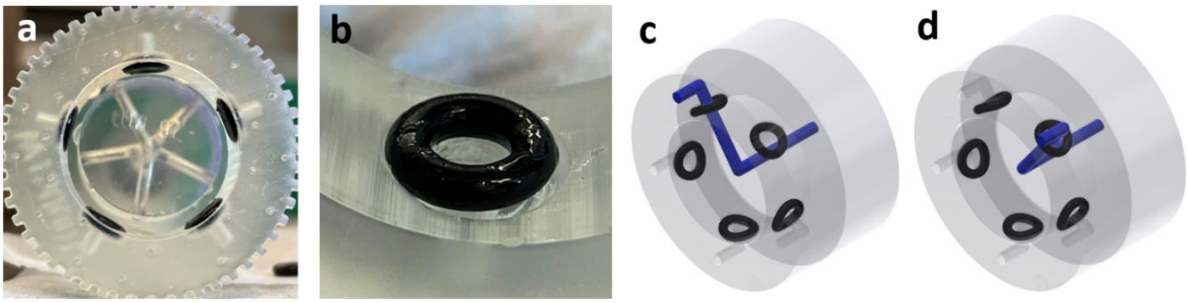


Figure 7.3. Rotary valve details. (a) End-on view of a 3D-printed rotary valve (the inner portion is removed) showing the fluidic channels and the sealing O-rings. (b) Detail view of a sealing O-ring sitting in its groove, fluid can pass through to the outer barrel when the inner portion is aligned to this O-ring. (c-d) 3D models of the fluidic pathways. In (c) the blue fluidic pathway is connected through the O-ring and to the outlet on the top of the valve, while in (d) the inner body is rotated 72° clockwise, so the pathway now connects through to the upper right outlet. All 5 outlets can be accessed through rotation of the inner valve body.

since there is only the single channel in the inner valve body, there is no path for liquid to flow from any of the other seals to the inner valve body. In Figure 7.3d, the inner valve body has been rotated 72° clockwise so that the upper-right path is selected by the valve. The inner valve body can be rotated to any of the O-rings to select which path is free to flow and which others are blocked. By combining several of these multi-way rotary valves with reservoirs, the silica membrane, the sample tube, and the syringe as shown in Figure 7.2, the full sample preparation procedure is achieved.

### 7.3.3 Fluidic actuations within the integrated syringe

The operation of the fluidic reservoirs and valves is visualized using a practical demonstration shown in Figure 7.4. Here an actual 3D-printed syringe is shown using colored dyes to represent the various reagents involved in the sample preparation process. Red for blood, blue for lysis buffer, yellow for washing buffer, and green for elution buffer. The device operates exactly as conceptualized in Figure 7.2 but with the colored dyes used instead of typical reagents so the transferring and mixing of the reagents can be visualized. First, the blood (red) is drawn from the sample tube (Figure 7.4a). As the blood continues to be drawn, it reaches the lysis chamber, which is preloaded with blue lysis

buffer, a drop of blood is shown falling into the lysis chamber (Figure 7.4b). The blood draw is completed when the blood reaches the level of the blood inlet and the red and blue blood and lysis buffer begin mixing to form a purple solution (Figure 7.4c). The integrated syringe is then shaken so the lysis buffer can fully mix with the blood. The blood is now completely lysed, and the resulting mixture is colored purple in Figure 7.4d. Next, the lysed mixture is pulled through the silica membrane, binding the RNA to the membrane. This process is in progress in Figure 7.4e and completed in Figure 7.4f, where the entire contents of the lysis chamber have been transferred to the waste reservoir. Now that the RNA is captured by the silica membrane, it must be washed using the yellow washing buffer. In Figure 7.4g the washing buffer begins to flow through the silica membrane and starts to enter the waste reservoir. Washing is completed in Figure 7.4h, notice that the integrated syringe has not been shaken so the resulting reagents are not mixed. This is not an issue since these are only waste products that are not important to the final sample. The final steps of the sample preparation process are the elution and ejection of the sample. First, the elution buffer (green) is pulled through the silica membrane to liberate the RNA from the membrane where it is stored in the purified reservoir. This is in progress in Figure 7.4i and completed in Figure 7.4j. Finally, the purified product is pushed out of the integrated syringe and injected into the sample tube. In Figure 7.4k the tube begins to fill, and in Figure 7.4l the process is complete. Figure 7.4m shows the resulting sample tube next to the original blood tube, where the color difference can be clearly discerned with little feedthrough of red blood present in the green purified sample.

### 7.3.4 Rapid viral detection from whole blood using the integrated syringe

To test the integrated syringe, four samples are prepared: a positive control (virus-spiked blood

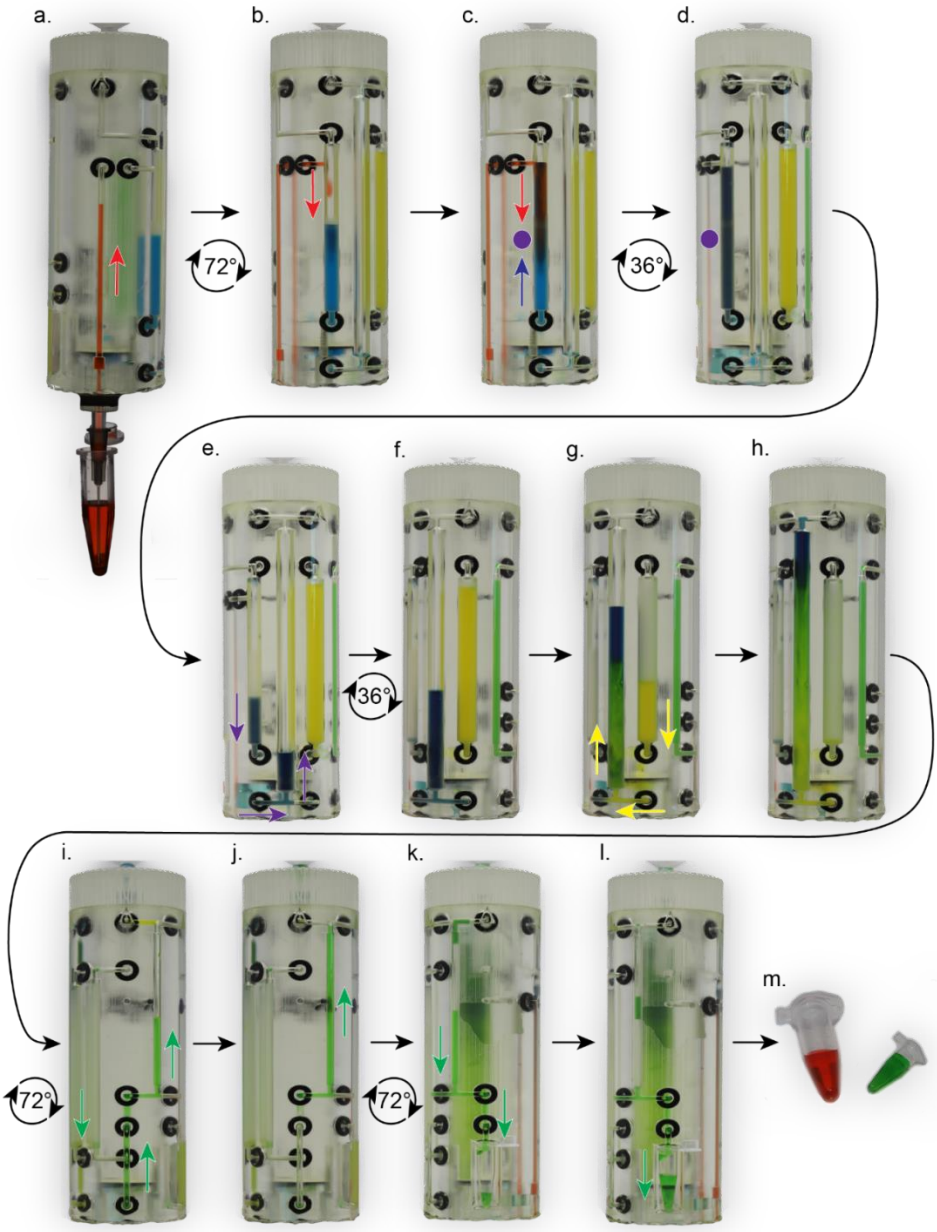


Figure 7.4. Operation of fabricated integrated syringe's fluidic system using food dye. (a) Red blood is drawn from the needle. (b) The blood begins to fall into the lysis chamber loaded with blue lysis buffer. (c) Blood begins mixing with lysis buffer to form a purple lysed product. (d) Blood is fully lysed. (e) Lysed product is pulled through the silica membrane for binding. (f) All of the lysed sample is pulled through to the waste chamber. (g) Yellow washing buffer begins flowing through the silica membrane into waste chamber. (h) All washing buffer has been used. (i) Green elution buffer begins elution of sample from the membrane. (j) Elution buffer is fully deposited into the purified reservoir. (k) Purified product begins ejection into sample tube. (l) Purified product is fully deposited into sample tube. (m) Sample tube next to blood source tube.

to be run through benchtop sample protocol), a negative control (blood to be run through benchtop protocol), a positive experimental sample (virus-spiked blood to be run through the integrated syringe for purification), and a negative experimental sample (blood to be run through the integrated syringe for purification). For each sample, after the respective extraction of nucleic acids, RT-qPCR reagents were mixed. After running RT-qPCR, amplification of the viral RNA source is observed (Figure 7.5). The positive experimental sample and the positive control (the dark green and dark red curves) show a clear amplification and cross above the threshold as expected. The qPCR curve from the integrated syringe sample is seen lagging behind the benchtop sample by approximately 2 cycles at the threshold level, this indicates that the RNA capture is not as efficient as the benchtop method, potentially due to increased fluidic surfaces the sample must encounter in the integrated syringe's design. It is however clear that the negative samples do not show any amplification as their qPCR curves stay below the threshold and do not exhibit the characteristic exponential growth seen in positive samples.

The PCR result shows that even with the slightly reduced capture efficiency of the integrated syringe, the difference between a positive and negative sample is large enough a post-purified sample can conclusively be used to determine the presence of viral RNA within a human blood sample. Therefore, the integrated syringe is effective at extracting viral RNA from a blood sample without any manual pipetting or extensive laboratory procedures and can yield a diagnostic level positive or negative test result.

## 7.4 Conclusions

The integrated syringe provides a new and simple methodology for the collection and purification of nucleic acids from blood. Collected samples provide sufficient quantity and purity to be used downstream in PCR reactions for diagnostic purposes. The ease of use of the integrated syringe enables lab-quality nucleic acid purification to be performed by a novice or less-skilled

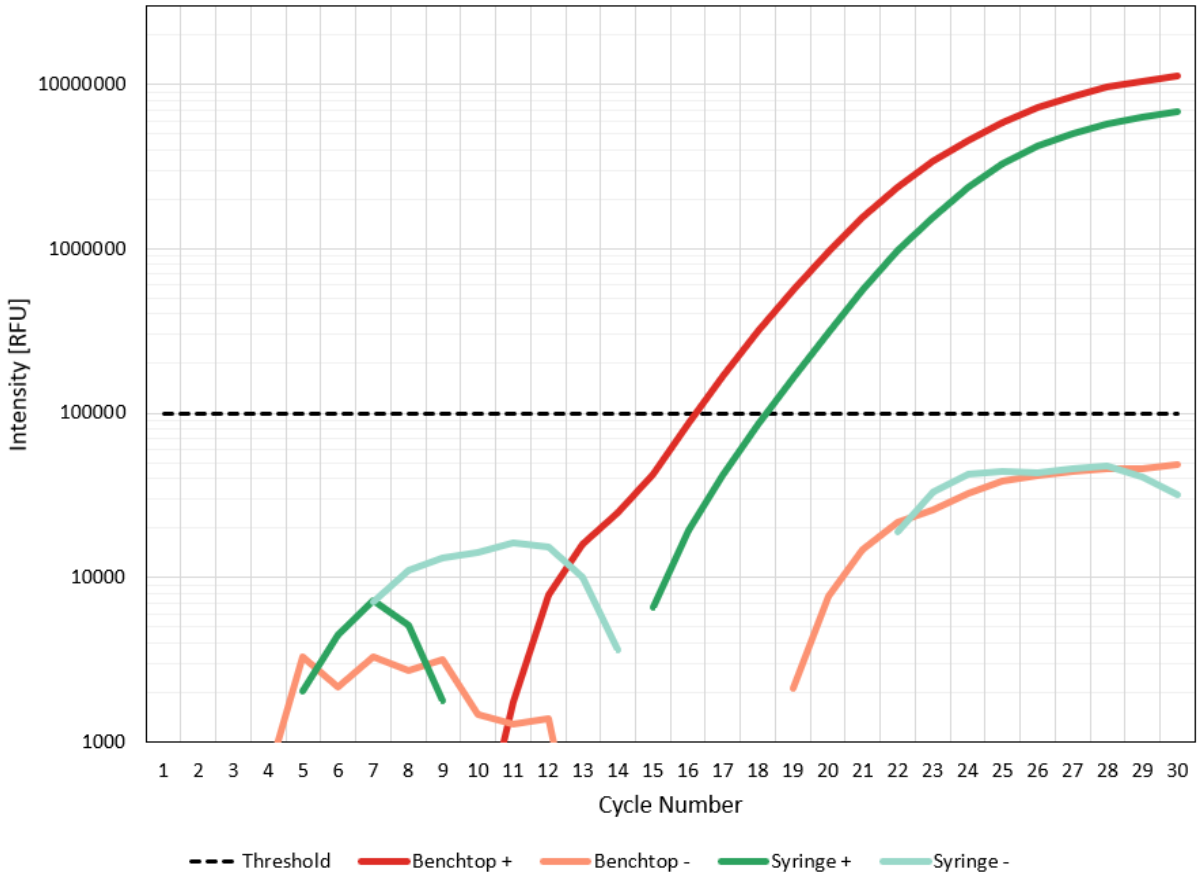


Figure 7.5. RT-qPCR data showing the capture of lentivirus from blood using the integrated syringe compared with benchtop method.

individuals. With the likelihood of future viral outbreaks, the integrated syringe provides the opportunity for a rapid deployment of high-quality PCR-based diagnostics to be administered on-site by eliminating some training and skill requirements of front-line workers.

## 7.5 Methods

### 7.5.1 Sample preparation protocol

Sample preparation of blood is performed by two methods to compare the effectiveness of the integrated syringe versus the traditional benchtop method. Both protocols are based on the recommended protocol from the PureLink Total RNA Blood Kit from Invitrogen (Waltham, MA)

with some modifications [162]. From the PureLink benchtop kit, only Lysis buffer 1, and washing buffer 2 are used for both the syringe and benchtop protocols. This is because to minimize complexity, the integrated syringe only uses a single lysis buffer and washing buffer. Volumes of reagents are not identical to the recommended protocol due to the removal of additional lysis and wash buffers and due to physical constraints based on the integrated syringe's physical dimensions. Positive samples consist of whole human blood (Innovative Research Inc., Novi, MI) which is spiked with target virus, while negative samples are unmodified whole human blood.

For the benchtop method, 200 µl of the sample is loaded into a tube preloaded with 400 µl of lysis buffer and gently mixed. The contents are transferred to a spin column and centrifuged. After centrifugation, the column is transferred to a clean collection tube, 700 µl of washing buffer is added, and the column is centrifuged again. This washing step is repeated once more (a total of 1400 µl of washing buffer is used per benchtop sample). After washing, the column is transferred to a fresh tube, 200 µl of RNase-free water is added and is centrifuged for the final time. The collection tube now contains the purified RNA captured from the sample by the silica filter contained in the spin column. The entire benchtop sample prep procedure takes approximately 5 to 7 minutes to complete by a skilled lab technician.

The sample prep process within the integrated syringe is much the same, but all centrifugation steps are replaced with suction created by the syringe plunger. To begin, the syringe is preloaded with 400 µl of lysis buffer, 1400 µl of washing buffer, and 200 µl of RNase-free water. The silica membrane is removed from a spin column and installed into the inner body of the integrated syringe during the assembly process. To begin an experiment, the syringe is rotated to the first position (binding and lysis), and the plunger is pulled to draw the 200 µl sample through the needle and into the lysis chamber. Once the entire sample is within the lysis chamber, the needle is removed for the safety of

the operator, and the syringe is gently shaken to mix the sample with the lysis buffer. Once complete, the syringe is rotated to the next position (binding) and the plunger is drawn, pulling the lysed sample through the silica membrane, and depositing the waste into the waste chamber. The syringe is then rotated to the third position (washing) where the plunger is drawn and pulls the washing buffer through the silica membrane and deposits it into the waste chamber. Once again, the syringe is rotated to the next position (elution) where the plunger pulls 200 µl of RNase-free water through the silica membrane to elute the captured RNA. Finally, a collection tube is placed into the syringe's outlet and the valve mechanism is rotated to the final position (ejection). The plunger is then pushed to eject the resuspended RNA sample into the collection tube. Since the reagents are preloaded, this process takes approximately one minute to complete.

### 7.5.2 Reverse-transcription quantitative polymerase chain reaction

Detection of a desired RNA target from blood requires RT-PCR to obtain a reliable, specific, and accurate result. The reverse transcription process produces cDNA from viral RNA which is then amplified and detected by qPCR. For this study, the target RNA is from a mouse lentivirus containing the mSox2 gene. The virus is sourced from abm Inc. (Richmond, BC, Canada). The mouse lentivirus was chosen for its similarity to HIV, while also posing a very low risk of infection to the human researchers. PCR primers are from a TaqMan assay (Applied Biosystems, Waltham, MA). Polymerase, reverse-transcriptase, and other PCR components are from VitaNavi Technology (Ballwin, MO). Reactions are run using an Applied Biosystems QuantStudio 7 Flex. Reactions begin with a 5-minute reverse transcription period at 60°C where the lentivirus RNA is converted to cDNA. This is followed by an initialization at 95°C for 20 seconds. Cycling is performed by denaturing at 95°C for 3 seconds and annealing/extending at 60°C for 30 seconds for a total of 30 cycles.

# CHAPTER 8: CONCLUSION

This research presented in this dissertation focused on the development of two distinct topics related to electronics and medical diagnostics. For each topic, tools were produced with the goals of reducing the cost, improving the accessibility, and enabling additional functionality. CMOS technology has been used to produce a dual-mode chip capable of simultaneously measuring action potentials and neurotransmitter release from a single on-chip electrode array. In the future, this technology can be used to study the breakdown of neurotransmission that is commonly seen in typical neurodegenerative diseases such as Alzheimer's and Parkinson's. Further research effort in this area will produce a more complete understanding of the dynamic decay that occurs in the brain through the course of these diseases and may give neuroscientists the ability to develop treatments to stop or reverse the decay process. Additionally, a compact and portable device for performing qPCR diagnostics has been developed that can be manufactured cheaply by a competent DIY maker. This device functions down to clinically relevant concentrations of viral load. Combined with the magnetic and syringe-based sample preparation devices, a complete diagnostic system for the detection of viral nucleic acids from infected blood is presented. Technologies like this will enable a faster and more effective response against future infectious disease outbreaks by providing easier access to powerful diagnostic tools.

# APPENDIX: COPYRIGHT AND REPRINT INFORMATION

**IEEE**

**(Chapters 2 and 3)**

**Thesis / Dissertation Reuse**

**The IEEE does not require individuals working on a thesis to obtain a formal reuse license, however, you may print out this statement to be used as a permission grant:**

*Requirements to be followed when using any portion (e.g., figure, graph, table, or textual material) of an IEEE copyrighted paper in a thesis:*

1) In the case of textual material (e.g., using short quotes or referring to the work within these papers) users must give full credit to the original source (author, paper, publication) followed by the IEEE copyright line © 2011 IEEE.

2) In the case of illustrations or tabular material, we require that the copyright line © [Year of original publication] IEEE appear prominently with each reprinted figure and/or table.

3) If a substantial portion of the original paper is to be used, and if you are not the senior author, also obtain the senior author's approval.

*Requirements to be followed when using an entire IEEE copyrighted paper in a thesis:*

1) The following IEEE copyright/ credit notice should be placed prominently in the references: © [year of original publication] IEEE. Reprinted, with permission, from [author names, paper title, IEEE publication title, and month/year of publication]

2) Only the accepted version of an IEEE copyrighted paper can be used when posting the paper or

your thesis on-line.

3) In placing the thesis on the author's university website, please display the following message in a prominent place on the website: In reference to IEEE copyrighted material which is used with permission in this thesis, the IEEE does not endorse any of [university/educational entity's name goes here]'s products or services. Internal or personal use of this material is permitted. If interested in reprinting/republishing IEEE copyrighted material for advertising or promotional purposes or for creating new collective works for resale or redistribution, please go to http://www.ieee.org/publications_standards/publications/rights/rights_link.html to learn how to obtain a License from RightsLink.

If applicable, University Microfilms and/or ProQuest Library, or the Archives of Canada may supply single copies of the dissertation.

**PLoS ONE**

**(Chapter 5)**



[*] https://creativecommons.org/licenses/by/4.0/

**ANALYTICAL METHODS**

**(Chapter 6)**

G. Mulberry, A. Vuillier, M. Vaidya, K. Sugaya and Brian N. Kim, *Anal. Methods*, 2018, **10**, 4671 **DOI:** 10.1039/C8AY00998H

# LIST OF REFERENCES


[1] J. D. WATSON and F. H. C. CRICK, "Molecular Structure of Nucleic Acids: A Structure for Deoxyribose Nucleic Acid," *Nature*, vol. 171, no. 4356, pp. 737–738, Apr. 1953, doi: 10.1038/171737a0.

[2] Nobel Prize Outreach AB, "The Nobel Prize in Physiology or Medicine 1962," 1962. https://www.nobelprize.org/prizes/medicine/1962/summary/ (accessed May 18, 2022).

[3] K. Mullis, F. Faloona, S. Scharf, R. Saiki, G. Horn, and H. Erlich, "Specific Enzymatic Amplification of DNA In Vitro: The Polymerase Chain Reaction," *Cold Spring Harbor Symposia on Quantitative Biology*, vol. 51, pp. 263–273, Jan. 1986, doi: 10.1101/SQB.1986.051.01.032.

[4] Nobel Prize Outreach AB, "Press release: The Nobel Prize in Chemistry 1993," 1993. https://www.nobelprize.org/prizes/chemistry/1993/press-release/ (accessed May 17, 2022).

[5] L. M. Smith *et al.*, "Fluorescence detection in automated DNA sequence analysis," *Nature*, vol. 321, no. 6071, pp. 674–679, Jun. 1986, doi: 10.1038/321674a0.

[6] J. M. Prober *et al.*, "A System for Rapid DNA Sequencing with Fluorescent Chain-Terminating Dideoxynucleotides," *Science (1979)*, vol. 238, no. 4825, pp. 336–341, Oct. 1987, doi: 10.1126/science.2443975.

[7] M. Crichton, *Jurassic Park*. New York: Knopf Doubleday Publishing Group, 1990.

[8] E. S. Lander *et al.*, "Initial sequencing and analysis of the human genome," *Nature*, vol. 409, no. 6822, pp. 860–921, Feb. 2001, doi: 10.1038/35057062.

[9] S. G. Gregory *et al.*, "The DNA sequence and biological annotation of human chromosome 1," *Nature*, vol. 441, no. 7091, pp. 315–321, May 2006, doi: 10.1038/nature04727.

[10] M. Jinek, K. Chylinski, I. Fonfara, M. Hauer, J. A. Doudna, and E. Charpentier, "A Programmable Dual-RNA–Guided DNA Endonuclease in Adaptive Bacterial Immunity," *Science (1979)*, vol. 337, no. 6096, pp. 816–821, Aug. 2012, doi: 10.1126/science.1225829.

[11] L. Cong *et al.*, "Multiplex Genome Engineering Using CRISPR/Cas Systems," *Science (1979)*, vol. 339, no. 6121, pp. 819–823, Feb. 2013, doi: 10.1126/science.1231143.

[12] Nobel Prize Outreach AB, "Press release: The Nobel Prize in Chemistry 2020," 2020. https://www.nobelprize.org/prizes/chemistry/2020/press-release/ (accessed May 17, 2022).

[13] V. L. Feigin *et al.*, "Global, regional, and national burden of neurological disorders, 1990–2016: a systematic analysis for the Global Burden of Disease Study 2016," *The Lancet Neurology*, vol. 18, no. 5, pp. 459–480, May 2019, doi: 10.1016/S1474-4422(18)30499-X.

[14] The Lancet Respiratory Medicine, "Future pandemics: failing to prepare means preparing to fail," *The Lancet Respiratory Medicine*, vol. 10, no. 3, pp. 221–222, Mar. 2022, doi: 10.1016/S2213-2600(22)00056-X.

[15] A. Sandberg and N. Bostrom, "Whole Brain Emulation: A Roadmap," Oxford, 2008. [Online]. Available: www.fhi.ox.ac.uk/reports/2008-3.pdf

[16] Argonne National Laboratory, "Aurora." https://www.alcf.anl.gov/aurora

[17] J. P. Cleary *et al.*, "Natural oligomers of the amyloid-β protein specifically disrupt cognitive function," *Nature Neuroscience*, vol. 8, no. 1, pp. 79–84, Jan. 2005, doi: 10.1038/nn1372.

[18] D. J. Selkoe, "Alzheimer's Disease: Genes, Proteins, and Therapy," *Physiological Reviews*, vol. 81, no. 2, pp. 741–766, Apr. 2001, doi: 10.1152/physrev.2001.81.2.741.

[19] R. D. Terry *et al.*, "Physical basis of cognitive alterations in alzheimer's disease: Synapse loss is the major correlate of cognitive impairment," *Annals of Neurology*, vol. 30, no. 4, pp. 572–580, Oct. 1991, doi: 10.1002/ana.410300410.

[20] E. Taoufik, G. Kouroupi, O. Zygogianni, and R. Matsas, "Synaptic dysfunction in neurodegenerative and neurodevelopmental diseases: an overview of induced pluripotent stem-cell-based disease models," *Open Biology*, vol. 8, no. 9, p. 180138, Sep. 2018, doi: 10.1098/rsob.180138.

[21] R. G. W. Staal, S. Rayport, and D. Sulzer, *Amperometric Detection of Dopamine Exocytosis from Synaptic Terminals*. 2007.

[22] S. Yang and R. E. Rothman, "PCR-based diagnostics for infectious diseases: uses, limitations, and future applications in acute-care settings," *The Lancet Infectious Diseases*, vol. 4, no. 6, pp. 337–348, Jun. 2004, doi: 10.1016/S1473-3099(04)01044-8.

[23] C. Ruiz, K. Kadimisetty, K. Yin, M. G. Mauk, H. Zhao, and C. Liu, "Fabrication of Hard–Soft Microfluidic Devices Using Hybrid 3D Printing," *Micromachines (Basel)*, vol. 11, no. 6, p. 567, Jun. 2020, doi: 10.3390/mi11060567.

[24] G. Mulberry, K. A. White, M. Vaidya, K. Sugaya, and B. N. Kim, "3D printing and milling a real-time PCR device for infectious disease diagnostics," *PLOS ONE*, vol. 12, no. 6, p. e0179133, Jun. 2017, doi: 10.1371/journal.pone.0179133.

[25] A. Chien, D. B. Edgar, and J. M. Trela, "Deoxyribonucleic acid polymerase from the extreme thermophile Thermus aquaticus," *Journal of Bacteriology*, vol. 127, no. 3, pp. 1550–1557, Sep. 1976, doi: 10.1128/jb.127.3.1550-1557.1976.

[26] C. Schrader, A. Schielke, L. Ellerbroek, and R. Johne, "PCR inhibitors - occurrence, properties and removal," *Journal of Applied Microbiology*, vol. 113, no. 5, pp. 1014–1026, Nov. 2012, doi: 10.1111/j.1365-2672.2012.05384.x.

[27] A. Castellanos-Gonzalez *et al.*, "Direct RT-PCR amplification of SARS-CoV-2 from clinical samples using a concentrated viral lysis-amplification buffer prepared with IGEPAL-630," *Scientific Reports*, vol. 11, no. 1, p. 14204, Dec. 2021, doi: 10.1038/s41598-021-93333-2.

[28] Michael L. A. V. Heien, and Michael A. Johnson, R. M. Wightman*, M. L. A. v. Heien, M. A. Johnson, and R. M. Wightman, "Resolving Neurotransmitters Detected by Fast-Scan Cyclic Voltammetry," *Analytical Chemistry*, vol. 76, no. 19, pp. 5697–5704, Oct. 2004, doi: 10.1021/ac0491509.

[29] D. L. Robinson, B. J. Venton, M. L. A. v Heien, and R. M. Wightman, "Detecting Subsecond Dopamine Release with Fast-Scan Cyclic Voltammetry in Vivo," *Clinical Chemistry*, vol. 49, no. 10, pp. 1763–1773, Oct. 2003, doi: 10.1373/49.10.1763.

[30] K. T. Kawagoe, J. B. Zimmerman, and R. M. Wightman, "Principles of voltammetry and microelectrode surface states," *Journal of Neuroscience Methods*, vol. 48, no. 3, pp. 225–240, Jul. 1993, doi: 10.1016/0165-0270(93)90094-8.

[31] S. Ayers, K. D. Gillis, M. Lindau, and B. A. Minch, "Design of a CMOS potentiostat circuit for electrochemical detector arrays," *IEEE Transactions on Circuits and Systems I: Regular Papers*, vol. 54, no. 4, pp. 736–744, Apr. 2007, doi: 10.1109/TCSI.2006.888777.

[32] J. Kim, K. Pedrotti, and W. B. Dunbar, "An area-efficient low-noise CMOS DNA detection sensor for multichannel nanopore applications," *Sensors and Actuators, B: Chemical*, vol. 176, pp. 1051–1055, Jan. 2013, doi: 10.1016/j.snb.2012.08.075.

[33] J. Dragas *et al.*, "<italic>In Vitro</italic> Multi-Functional Microelectrode Array Featuring 59 760 Electrodes, 2048 Electrophysiology Channels, Stimulation, Impedance Measurement, and Neurotransmitter Detection Channels," *IEEE Journal of Solid-State Circuits*, vol. 52, no. 6, pp. 1576–1590, Jun. 2017, doi: 10.1109/JSSC.2017.2686580.

[34] K. A. White, G. Mulberry, and B. N. Kim, "Rapid 1024-Pixel Electrochemical Imaging at 10,000 Frames Per Second Using Monolithic CMOS Sensor and Multifunctional Data Acquisition System," *IEEE Sensors Journal*, vol. 18, no. 13, pp. 5507–5514, Jul. 2018, doi: 10.1109/JSEN.2018.2835829.

[35] K. A. White *et al.*, "Single-Cell Recording of Vesicle Release From Human Neuroblastoma Cells Using 1024-ch Monolithic CMOS Bioelectronics," *IEEE Transactions on Biomedical Circuits and Systems*, vol. 12, no. 6, pp. 1345–1355, Dec. 2018, doi: 10.1109/TBCAS.2018.2861220.

[36] J. Allen, "Photoplethysmography and its application in clinical physiological measurement," *Physiological Measurement*, vol. 28, no. 3, pp. R1–R39, Mar. 2007, doi: 10.1088/0967-3334/28/3/R01.

[37] A. K. Y. Wong, K.-P. Pun, Y.-T. Zhang, and K. N. Leung, "A Low-Power CMOS Front-End for Photoplethysmographic Signal Acquisition With Robust DC Photocurrent Rejection," *IEEE Transactions on Biomedical Circuits and Systems*, vol. 2, no. 4, pp. 280–288, Dec. 2008, doi: 10.1109/TBCAS.2008.2003429.

[38] V. Rybynok, J. M. May, K. Budidha, and P. A. Kyriacou, "Design and development of a novel multi-channel photoplethysmographic research system," in *2013 IEEE Point-of-Care Healthcare Technologies (PHT)*, Jan. 2013, pp. 267–270. doi: 10.1109/PHT.2013.6461336.

[39] M. Tavakoli, L. Turicchia, and R. Sarpeshkar, "An Ultra-Low-Power Pulse Oximeter Implemented With an Energy-Efficient Transimpedance Amplifier," *IEEE Transactions on Biomedical Circuits and Systems*, vol. 4, no. 1, pp. 27–38, Feb. 2010, doi: 10.1109/TBCAS.2009.2033035.

[40] J. K. Rosenstein, M. Wanunu, C. A. Merchant, M. Drndic, and K. L. Shepard, "Integrated nanopore sensing platform with sub-microsecond temporal resolution," *Nature Methods*, vol. 9, no. 5, pp. 487–492, May 2012, doi: 10.1038/nmeth.1932.

[41] J. K. Rosenstein, S. Ramakrishnan, J. Roseman, and K. L. Shepard, "Single Ion Channel Recordings with CMOS-Anchored Lipid Membranes," *Nano Letters*, vol. 13, no. 6, pp. 2682–2686, Jun. 2013, doi: 10.1021/nl400822r.

[42] H. Li, S. Parsnejad, E. Ashoori, C. Thompson, E. K. Purcell, and A. J. Mason, "Ultracompact Microwatt CMOS Current Readout with Picoampere Noise and Kilohertz Bandwidth for Biosensor Arrays," *IEEE Transactions on Biomedical Circuits and Systems*, vol. 12, no. 1, pp. 35–46, Feb. 2018, doi: 10.1109/TBCAS.2017.2752742.

[43] B. N. Kim, A. D. Herbst, S. J. Kim, B. A. Minch, and M. Lindau, "Parallel recording of neurotransmitters release from chromaffin cells using a 10×10 CMOS IC potentiostat array with on-chip working electrodes," *Biosensors and Bioelectronics*, vol. 41, pp. 736–744, Mar. 2013, doi: 10.1016/j.bios.2012.09.058.

[44] E. Ashoori *et al.*, "Compact and Low Power Analog Front End with in-situ Data Decimator for High-Channel-Count ECoG Recording," in *2018 IEEE International Symposium on Circuits and Systems (ISCAS)*, May 2018, vol. 2, pp. 6–10. doi: 10.1109/ISCAS.2018.8351245.

[45] C. I. Dorta-Quinones *et al.*, "A Bidirectional-Current CMOS Potentiostat for Fast-Scan Cyclic Voltammetry Detector Arrays," *IEEE Transactions on Biomedical Circuits and Systems*, vol. 12, no. 4, pp. 894–903, Aug. 2018, doi: 10.1109/TBCAS.2018.2828828.

[46] C.-Y. Wu, C.-C. Hsieh, F.-W. Jih, T. P. Sun, and S.-J. Yang, *A new share-buffered direct-injection readout structure for infrared detector*, vol. 2020, no. Infrared Technology XIX. 1993. doi: 10.1117/12.160581.

[47] J. S. Park *et al.*, "1024-Pixel CMOS Multimodality Joint Cellular Sensor/Stimulator Array for Real-Time Holistic Cellular Characterization and Cell-Based Drug Screening," *IEEE Transactions on Biomedical Circuits and Systems*, vol. 12, no. 1, pp. 80–94, Feb. 2018, doi: 10.1109/TBCAS.2017.2759220.

[48] J. Guo, W. Ng, J. Yuan, S. Li, and M. Chan, "A 200-Channel Area-Power-Efficient Chemical and Electrical Dual-Mode Acquisition IC for the Study of Neurodegenerative Diseases," *IEEE Transactions on Biomedical Circuits and Systems*, vol. 10, no. 3, pp. 567–578, Jun. 2016, doi: 10.1109/TBCAS.2015.2468052.

[49] N. Kasai, A. Shimada, T. Nyberg, and K. Torimitsu, "An electrochemical sensor array and its application to real-time brain slice imaging," *Electronics and Communications in Japan*, vol. 92, no. 9, pp. 1–6, Sep. 2009, doi: 10.1002/ecj.10140.

[50] M. K. Zachek, P. Takmakov, J. Park, R. M. Wightman, and G. S. McCarty, "Simultaneous monitoring of dopamine concentration at spatially different brain locations in vivo," *Biosensors and Bioelectronics*, vol. 25, no. 5, pp. 1179–1185, Jan. 2010, doi: 10.1016/j.bios.2009.10.008.

[51] D. L. Bellin, H. Sakhtah, Y. Zhang, A. Price-Whelan, L. E. P. Dietrich, and K. L. Shepard, "Electrochemical camera chip for simultaneous imaging of multiple metabolites in biofilms," *Nature Communications*, vol. 7, no. 1, p. 10535, Apr. 2016, doi: 10.1038/ncomms10535.

[52] T. Tokuda, K. Tanaka, M. Matsuo, K. Kagawa, M. Nunoshita, and J. Ohta, "Optical and electrochemical dual-image CMOS sensor for on-chip biomolecular sensing applications," *Sensors and Actuators A: Physical*, vol. 135, no. 2, pp. 315–322, Apr. 2007, doi: 10.1016/j.sna.2006.08.027.

[53] M. M. Rahman, A. Umar, and K. Sawada, "Development of amperometric glucose biosensor based on glucose oxidase co-immobilized with multi-walled carbon nanotubes at low

potential," *Sensors and Actuators B: Chemical*, vol. 137, no. 1, pp. 327–333, Mar. 2009, doi: 10.1016/j.snb.2008.10.060.

[54] S. Takenaga, Y. Tamai, K. Okumura, M. Ishida, and K. Sawada, "Label-Free Acetylcholine Image Sensor Based on Charge Transfer Technology for Biological Phenomenon Tracking," *Japanese Journal of Applied Physics*, vol. 51, p. 27001, 2012, doi: 10.1143/jjap.51.027001.

[55] A. Hassibi and T. H. Lee, "A Programmable 0.18-$\mu\hbox{m}$ CMOS Electrochemical Sensor Microarray for Biomolecular Detection," *IEEE Sensors Journal*, vol. 6, no. 6, pp. 1380–1388, Dec. 2006, doi: 10.1109/JSEN.2006.883904.

[56] V. Viswam *et al.*, "22.8 Multi-functional microelectrode array system featuring 59,760 electrodes, 2048 electrophysiology channels, impedance and neurotransmitter measurement units," in *2016 IEEE International Solid-State Circuits Conference (ISSCC)*, Jan. 2016, pp. 394–396. doi: 10.1109/ISSCC.2016.7418073.

[57] J. Dragas *et al.*, "*In Vitro* Multi-Functional Microelectrode Array Featuring 59 760 Electrodes, 2048 Electrophysiology Channels, Stimulation, Impedance Measurement, and Neurotransmitter Detection Channels," *IEEE Journal of Solid-State Circuits*, vol. 52, no. 6, pp. 1576–1590, Jun. 2017, doi: 10.1109/JSSC.2017.2686580.

[58] P. Shields, B. Nemeth, R. B. Green, M. O. Riehle, and D. R. S. Cumming, "High-Speed Imaging of 2-D Ionic Diffusion Using a 16$\,\times\,$16 Pixel CMOS ISFET Array on the Microfluidic Scale," *IEEE Sensors Journal*, vol. 12, no. 9, pp. 2744–2749, Sep. 2012, doi: 10.1109/JSEN.2012.2200249.

[59] J. Rothe, O. Frey, A. Stettler, Y. Chen, and A. Hierlemann, "Fully Integrated CMOS Microsystem for Electrochemical Measurements on 32 × 32 Working Electrodes at 90 Frames

Per Second," *Analytical Chemistry*, vol. 86, no. 13, pp. 6425–6432, Jul. 2014, doi: 10.1021/ac500862v.

[60] J. P. Grinias, J. T. Whitfield, E. D. Guetschow, and R. T. Kennedy, "An Inexpensive, Open-Source USB Arduino Data Acquisition Device for Chemical Instrumentation," *Journal of Chemical Education*, vol. 93, no. 7, pp. 1316–1319, Jul. 2016, doi: 10.1021/acs.jchemed.6b00262.

[61] D. Hercog and B. Gergič, "A Flexible Microcontroller-Based Data Acquisition Device," *Sensors*, vol. 14, no. 6, pp. 9755–9775, Jun. 2014, doi: 10.3390/s140609755.

[62] F. J. Ferrero Martín, M. Valledor Llopis, J. C. Campo Rodríguez, J. R. Blanco González, and J. Menéndez Blanco, "Low-cost open-source multifunction data acquisition system for accurate measurements," *Measurement*, vol. 55, pp. 265–271, Sep. 2014, doi: 10.1016/j.measurement.2014.05.010.

[63] J. P. Kinney *et al.*, "A direct-to-drive neural data acquisition system," *Frontiers in Neural Circuits*, vol. 9, Sep. 2015, doi: 10.3389/fncir.2015.00046.

[64] R. Rajpal *et al.*, "Embedded multi-channel data acquisition system on FPGA for Aditya Tokamak," *Fusion Engineering and Design*, vol. 112, pp. 964–968, Nov. 2016, doi: 10.1016/j.fusengdes.2016.03.068.

[65] D. A. Borton *et al.*, "An Implantable Wireless Neural Interface for Recording Cortical Circuit Dynamics in Moving Primates," *J Neural Eng.*, vol. 10, no. 2, pp. 1–25, 2013, doi: 10.1088/1741-2560/10/2/026010.An.

[66] J. Dunlop, M. Bowlby, R. Peri, D. Vasilyev, and R. Arias, "High-throughput electrophysiology: an emerging paradigm for ion-channel screening and physiology," *Nature Reviews Drug Discovery*, vol. 7, no. 4, pp. 358–368, Apr. 2008, doi: 10.1038/nrd2552.

[67] J. S. Park *et al.*, "1024-Pixel CMOS Multimodality Joint Cellular Sensor/Stimulator Array for Real-Time Holistic Cellular Characterization and Cell-Based Drug Screening," *IEEE Transactions on Biomedical Circuits and Systems*, vol. 12, no. 1, pp. 80–94, Feb. 2018, doi: 10.1109/TBCAS.2017.2759220.

[68] J. K. Rosenstein, M. Wanunu, C. A. Merchant, M. Drndic, and K. L. Shepard, "Integrated nanopore sensing platform with sub-microsecond temporal resolution," *Nature Methods*, vol. 9, no. 5, pp. 487–492, May 2012, doi: 10.1038/nmeth.1932.

[69] K. Kisler *et al.*, "Transparent Electrode Materials for Simultaneous Amperometric Detection of Exocytosis and Fluorescence Microscopy," *Journal of Biomaterials and Nanobiotechnology*, vol. 03, no. 02, pp. 243–253, 2012, doi: 10.4236/jbnb.2012.322030.

[70] H. Braak, E. Braak, and J. Bohl, "Staging of Alzheimer-Related Cortical Destruction," *European Neurology*, vol. 33, no. 6, pp. 403–408, 1993, doi: 10.1159/000116984.

[71] D. J. Selkoe, "The molecular pathology of Alzheimer's disease," *Neuron*, vol. 6, no. 4, pp. 487–498, Apr. 1991, doi: 10.1016/0896-6273(91)90052-2.

[72] L. Stefanis, "α-Synuclein in Parkinson's disease.," *Cold Spring Harb Perspect Med*, vol. 2, no. 2, p. a009399, Feb. 2012, doi: 10.1101/cshperspect.a009399.

[73] X. Zhang *et al.*, "Tau Pathology in Parkinson's Disease," *Frontiers in Neurology*, vol. 9, Oct. 2018, doi: 10.3389/fneur.2018.00809.

[74] T. Duka, V. Duka, J. N. Joyce, and A. Sidhu, "α-Synuclein contributes to GSK-3β-catalyzed Tau phosphorylation in Parkinson's disease models," *The FASEB Journal*, vol. 23, no. 9, pp. 2820–2830, Sep. 2009, doi: 10.1096/fj.08-120410.

[75] S. W. Scheff, D. A. Price, F. A. Schmitt, S. T. DeKosky, and E. J. Mufson, "Synaptic alterations in CA1 in mild Alzheimer disease and mild cognitive impairment," *Neurology*, vol. 68, no. 18, pp. 1501–1508, May 2007, doi: 10.1212/01.wnl.0000260698.46517.8f.

[76] F. Maestú *et al.*, "A multicenter study of the early detection of synaptic dysfunction in Mild Cognitive Impairment using Magnetoencephalography-derived functional connectivity," *NeuroImage: Clinical*, vol. 9, pp. 103–109, 2015, doi: 10.1016/j.nicl.2015.07.011.

[77] K. A. White *et al.*, "Single-Cell Recording of Vesicle Release From Human Neuroblastoma Cells Using 1024-ch Monolithic CMOS Bioelectronics," *IEEE Transactions on Biomedical Circuits and Systems*, vol. 12, no. 6, pp. 1345–1355, Dec. 2018, doi: 10.1109/TBCAS.2018.2861220.

[78] K. E. Larsen *et al.*, "alpha-Synuclein Overexpression in PC12 and Chromaffin Cells Impairs Catecholamine Release by Interfering with a Late Step in Exocytosis," *Journal of Neuroscience*, vol. 26, no. 46, pp. 11915–11922, 2006, doi: 10.1523/JNEUROSCI.3821-06.2006.

[79] L. Stefanis, K. E. Larsen, H. J. Rideout, D. Sulzer, and L. A. Greene, "Expression of A53T mutant but not wild-type alpha-synuclein in PC12 cells induces alterations of the ubiquitin-dependent degradation system, loss of dopamine release, and autophagic cell death.," *Journal of Neuroscience*, vol. 21, no. 24, pp. 9549–60, 2001, doi: 21/24/9549 [pii].

[80] G. Nagy *et al.*, "Regulation of Releasable Vesicle Pool Sizes by Protein Kinase A-Dependent Phosphorylation of SNAP-25," *Neuron*, vol. 41, no. 3, pp. 417–429, 2004, doi: 10.1016/S0896-6273(04)00038-8.

[81] V. A. Klenchin and T. F. J. Martin, "Priming in exocytosis: Attaining fusion-competence after vesicle docking," *Biochimie*, vol. 82, no. 5, pp. 399–407, 2000, doi: 10.1016/S0300-9084(00)00208-X.

[82] R. S. Snider, "Neurophysiology: A Primer," *Neurology*, vol. 17, no. 8, 1967, doi: 10.1212/wnl.17.8.824.

[83] K. Schmidt-Nielsen, *Animal physiology : adaptation and environment*, 5th ed. Cambridge: Cambridge University Press, 1997.

[84] T. H. Bullock, R. Orkand, and A. Grinnell, *Introduction to nervous systems*. San Francisco: W. H. Freeman, 1977.

[85] V. Vijay *et al.*, "High-density CMOS microelectrode array system for impedance spectroscopy and imaging of biological cells," in *2016 IEEE SENSORS*, Oct. 2016, pp. 1–3. doi: 10.1109/ICSENS.2016.7808761.

[86] H. Amin, T. Nieus, D. Lonardoni, A. Maccione, and L. Berdondini, "High-resolution bioelectrical imaging of Aβ-induced network dysfunction on CMOS-MEAs for neurotoxicity and rescue studies," *Scientific Reports*, vol. 7, no. 1, p. 2460, Dec. 2017, doi: 10.1038/s41598-017-02635-x.

[87] J. Guo, W. Ng, J. Yuan, S. Li, and M. Chan, "A 200-Channel Area-Power-Efficient Chemical and Electrical Dual-Mode Acquisition IC for the Study of Neurodegenerative Diseases," *IEEE Transactions on Biomedical Circuits and Systems*, vol. 10, no. 3, pp. 567–578, Jun. 2016, doi: 10.1109/TBCAS.2015.2468052.

[88] J. S. Park *et al.*, "1024-Pixel CMOS Multimodality Joint Cellular Sensor/Stimulator Array for Real-Time Holistic Cellular Characterization and Cell-Based Drug Screening," *IEEE Transactions on Biomedical Circuits and Systems*, vol. 12, no. 1, pp. 80–94, Feb. 2018, doi: 10.1109/TBCAS.2017.2759220.

[89] K. A. White and B. N. Kim, "Quantifying neurotransmitter secretion at single-vesicle resolution using high-density complementary metal–oxide–semiconductor electrode array," *Nature Communications*, vol. 12, no. 1, p. 431, Dec. 2021, doi: 10.1038/s41467-020-20267-0.

[90] G. Mulberry, K. A. White, and B. N. Kim, "Analysis of Simple Half-Shared Transimpedance Amplifier for Picoampere Biosensor Measurements," *IEEE Transactions on Biomedical Circuits and Systems*, vol. 13, no. 2, pp. 387–395, Apr. 2019, doi: 10.1109/TBCAS.2019.2897287.

[91] R. R. Harrison and C. Charles, "A Low-Power Low-Noise CMOS Amplifier for Neural Recording Applications," *IEEE Journal of Solid-State Circuits*, vol. 38, no. 6, pp. 958–965, Jun. 2003, doi: 10.1109/JSSC.2003.811979.

[92] K. A. White, G. Mulberry, and B. N. Kim, "Parallel 1024-ch Cyclic Voltammetry on Monolithic CMOS Electrochemical Detector Array," *IEEE Sensors Journal*, vol. 20, no. 8, pp. 4395–4402, Apr. 2020, doi: 10.1109/JSEN.2019.2961809.

[93] Michael L. A. V. Heien, and Michael A. Johnson, R. M. Wightman*, M. L. A. v. Heien, M. A. Johnson, and R. M. Wightman, "Resolving Neurotransmitters Detected by Fast-Scan Cyclic Voltammetry," *Analytical Chemistry*, vol. 76, no. 19, pp. 5697–5704, Oct. 2004.

[94] N. Elgrishi, K. J. Rountree, B. D. McCarthy, E. S. Rountree, T. T. Eisenhart, and J. L. Dempsey, "A Practical Beginner's Guide to Cyclic Voltammetry," *Journal of Chemical Education*, vol. 95, no. 2, pp. 197–206, Feb. 2018, doi: 10.1021/acs.jchemed.7b00361.

[95] S. Ayers, K. D. Gillis, M. Lindau, and B. A. Minch, "Design of a CMOS potentiostat circuit for electrochemical detector arrays," *IEEE Transactions on Circuits and Systems I: Regular Papers*, vol. 54, no. 4, pp. 736–744, Apr. 2007, doi: 10.1109/TCSI.2006.888777.

[96] H. Li, S. Parsnejad, E. Ashoori, C. Thompson, E. K. Purcell, and A. J. Mason, "Ultracompact Microwatt CMOS Current Readout with Picoampere Noise and Kilohertz Bandwidth for

Biosensor Arrays," *IEEE Transactions on Biomedical Circuits and Systems*, vol. 12, no. 1, pp. 35–46, Feb. 2018, doi: 10.1109/TBCAS.2017.2752742.

[97] C. C. Enz, F. Krummenacher, and E. A. Vittoz, "An analytical MOS transistor model valid in all regions of operation and dedicated to low-voltage and low-current applications," *Analog Integrated Circuits and Signal Processing*, vol. 8, no. 1, pp. 83–114, Jul. 1995, doi: 10.1007/BF01239381.

[98] K. Najafi and K. D. Wise, "An implantable multielectrode array with on-chip signal processing," *IEEE Journal of Solid-State Circuits*, vol. 21, no. 6, pp. 1035–1044, Dec. 1986, doi: 10.1109/JSSC.1986.1052646.

[99] A. C. Metting van Rijn, A. Peper, and C. A. Grimbergen, "High-quality recording of bioelectric events," *Medical & Biological Engineering & Computing*, vol. 28, no. 5, pp. 389–397, Sep. 1990, doi: 10.1007/BF02441961.

[100] E. M. Izhikevich, "Simple model of spiking neurons," *IEEE Transactions on Neural Networks*, vol. 14, no. 6, pp. 1569–1572, Nov. 2003, doi: 10.1109/TNN.2003.820440.

[101] G. N. Angotzi *et al.*, "A high temporal resolution multiscale recording system for in vivo neural studies," in *2017 IEEE International Symposium on Circuits and Systems (ISCAS)*, May 2017, pp. 1–4. doi: 10.1109/ISCAS.2017.8050617.

[102] C. Mora Lopez *et al.*, "A Neural Probe With Up to 966 Electrodes and Up to 384 Configurable Channels in 0.13 $\mu$m SOI CMOS," *IEEE Transactions on Biomedical Circuits and Systems*, vol. 11, no. 3, pp. 510–522, Jun. 2017, doi: 10.1109/TBCAS.2016.2646901.

[103] X. Yuan, V. Emmenegger, M. E. J. Obien, A. Hierlemann, and U. Frey, "Dual-mode Microelectrode Array Featuring 20k Electrodes and High SNR for Extracellular Recording of

Neural Networks," in *2018 IEEE Biomedical Circuits and Systems Conference (BioCAS)*, Oct. 2018, pp. 1–4. doi: 10.1109/BIOCAS.2018.8584735.

[104] A. Moody, "Rapid Diagnostic Tests for Malaria Parasites," *Clinical Microbiology Reviews*, vol. 15, no. 1, pp. 66–78, Jan. 2002, doi: 10.1128/CMR.15.1.66-78.2002.

[105] WHO, "Recommended selection criteria for procurement of malaria rapid diagnostic tests," 2016. https://apps.who.int/iris/handle/10665/259870

[106] N. E. Rosenberg *et al.*, "Detection of Acute HIV Infection: A Field Evaluation of the Determine® HIV-1/2 Ag/Ab Combo Test," *The Journal of Infectious Diseases*, vol. 205, no. 4, pp. 528–534, Feb. 2012, doi: 10.1093/infdis/jir789.

[107] B. M. Branson *et al.*, "Revised recommendations for HIV testing of adults, adolescents, and pregnant women in health-care settings.," *MMWR Recomm Rep*, vol. 55, no. RR-14, pp. 1–17; quiz CE1-4, Sep. 2006, [Online]. Available: http://www.ncbi.nlm.nih.gov/pubmed/16988643

[108] P. B. Bloland, W. H. Organization. A.-I. D. R. Surveillance, and C. Team, "Drug resistance in malaria / Peter B. Bloland." World Health Organization, p. A background document for the WHO global strategy, 2001.

[109] J. M. S. Bartlett and D. Stirling, "A Short History of the Polymerase Chain Reaction," in *PCR Protocols*, New Jersey: Humana Press, pp. 3–6. doi: 10.1385/1-59259-384-4:3.

[110] J. D. Watson, T. A. Baker, A. Gann, M. Levine, and R. Losick, *Molecular Biology of the Gene*, 7th ed. Pearson, 2013.

[111] T. Kojima, Y. Takei, M. Ohtsuka, Y. Kawarasaki, T. Yamane, and H. Nakano, "PCR amplification from single DNA molecules on magnetic beads in emulsion: application for high-throughput screening of transcription factor targets.," *Nucleic Acids Res*, vol. 33, no. 17, p. e150, Oct. 2005, doi: 10.1093/nar/gni143.

[112] K. R. Tan, K. A. Cullen, E. H. Koumans, and P. M. Arguin, "Inadequate Diagnosis and Treatment of Malaria Among Travelers Returning from Africa During the Ebola Epidemic — United States, 2014–2015," *MMWR. Morbidity and Mortality Weekly Report*, vol. 65, no. 2, pp. 27–29, Jan. 2016, doi: 10.15585/mmwr.mm6502a3.

[113] C. Zhang and D. Xing, "Miniaturized PCR chips for nucleic acid amplification and analysis: latest advances and future trends.," *Nucleic Acids Res*, vol. 35, no. 13, pp. 4223–37, 2007, doi: 10.1093/nar/gkm389.

[114] C. D. Ahrberg, B. R. Ilic, A. Manz, and P. Neužil, "Handheld real-time PCR device.," *Lab Chip*, vol. 16, no. 3, pp. 586–92, Feb. 2016, doi: 10.1039/c5lc01415h.

[115] D. R. Almassian, L. M. Cockrell, and W. M. Nelson, "Portable nucleic acid thermocyclers.," *Chem Soc Rev*, vol. 42, no. 22, pp. 8769–98, Nov. 2013, doi: 10.1039/c3cs60144g.

[116] N. Agrawal, Y. A. Hassan, and V. M. Ugaz, "A pocket-sized convective PCR thermocycler.," *Angew Chem Int Ed Engl*, vol. 46, no. 23, pp. 4316–9, 2007, doi: 10.1002/anie.200700306.

[117] C. Koo *et al.*, "Development of a real-time microchip PCR system for portable plant disease diagnosis.," *PLoS One*, vol. 8, no. 12, p. e82704, 2013, doi: 10.1371/journal.pone.0082704.

[118] P. Neuzil, C. Zhang, J. Pipper, S. Oh, and L. Zhuo, "Ultra fast miniaturized real-time PCR: 40 cycles in less than six minutes.," *Nucleic Acids Res*, vol. 34, no. 11, p. e77, Jun. 2006, doi: 10.1093/nar/gkl416.

[119] S. Waheed *et al.*, "3D printed microfluidic devices: enablers and barriers.," *Lab Chip*, vol. 16, no. 11, pp. 1993–2013, 2016, doi: 10.1039/c6lc00284f.

[120] C. M. B. Ho, S. H. Ng, K. H. H. Li, and Y.-J. Yoon, "3D printed microfluidics for biological applications.," *Lab Chip*, vol. 15, no. 18, pp. 3627–37, 2015, doi: 10.1039/c5lc00685f.

[121] D. Chudobova *et al.*, "3D-printed chip for detection of methicillin-resistant Staphylococcus aureus labeled with gold nanoparticles.," *Electrophoresis*, vol. 36, no. 3, pp. 457–66, Feb. 2015, doi: 10.1002/elps.201400321.

[122] A. A. Rowe *et al.*, "CheapStat: an open-source, 'do-it-yourself' potentiostat for analytical and educational applications.," *PLoS One*, vol. 6, no. 9, p. e23783, 2011, doi: 10.1371/journal.pone.0023783.

[123] M. D. M. Dryden and A. R. Wheeler, "DStat: A Versatile, Open-Source Potentiostat for Electroanalysis and Integration.," *PLoS One*, vol. 10, no. 10, p. e0140349, 2015, doi: 10.1371/journal.pone.0140349.

[124] B. T. Wittbrodt, D. A. Squires, J. Walbeck, E. Campbell, W. H. Campbell, and J. M. Pearce, "Open-Source Photometric System for Enzymatic Nitrate Quantification.," *PLoS One*, vol. 10, no. 8, p. e0134989, 2015, doi: 10.1371/journal.pone.0134989.

[125] D. G. Rosenegger, C. H. T. Tran, J. LeDue, N. Zhou, and G. R. Gordon, "A high performance, cost-effective, open-source microscope for scanning two-photon microscopy that is modular and readily adaptable.," *PLoS One*, vol. 9, no. 10, p. e110475, 2014, doi: 10.1371/journal.pone.0110475.

[126] M. F. Cole, S. E. Johnstone, J. J. Newman, M. H. Kagey, and R. A. Young, "Tcf3 is an integral component of the core regulatory circuitry of embryonic stem cells.," *Genes Dev*, vol. 22, no. 6, pp. 746–55, Mar. 2008, doi: 10.1101/gad.1642408.

[127] K. A. Sollis *et al.*, "Systematic review of the performance of HIV viral load technologies on plasma samples.," *PLoS One*, vol. 9, no. 2, p. e85869, 2014, doi: 10.1371/journal.pone.0085869.

[128] S. Troxler, A. Marek, I. Prokofieva, I. Bilic, and M. Hess, "TaqMan real-time reverse transcription-PCR assay for universal detection and quantification of avian hepatitis E virus

from clinical samples in the presence of a heterologous internal control RNA.," *J Clin Microbiol*, vol. 49, no. 4, pp. 1339–46, Apr. 2011, doi: 10.1128/JCM.01626-10.

[129] S. P. Johnston, N. J. Pieniazek, M. v Xayavong, S. B. Slemenda, P. P. Wilkins, and A. J. da Silva, "PCR as a confirmatory technique for laboratory diagnosis of malaria.," *J Clin Microbiol*, vol. 44, no. 3, pp. 1087–9, Mar. 2006, doi: 10.1128/JCM.44.3.1087-1089.2006.

[130] A. St John and C. P. Price, "Existing and Emerging Technologies for Point-of-Care Testing.," *Clin Biochem Rev*, vol. 35, no. 3, pp. 155–67, Aug. 2014.

[131] R. Boom, C. J. Sol, M. M. Salimans, C. L. Jansen, P. M. Wertheim-van Dillen, and J. van der Noordaa, "Rapid and simple method for purification of nucleic acids.," *J Clin Microbiol*, vol. 28, no. 3, pp. 495–503, Mar. 1990.

[132] R. Marshall *et al.*, "Characteristics of the m2000 automated sample preparation and multiplex real-time PCR system for detection of Chlamydia trachomatis and Neisseria gonorrhoeae.," *J Clin Microbiol*, vol. 45, no. 3, pp. 747–51, Mar. 2007, doi: 10.1128/JCM.01956-06.

[133] K. M. Koo, E. J. H. Wee, Y. Wang, and M. Trau, "Enabling miniaturised personalised diagnostics: from lab-on-a-chip to lab-in-a-drop," *Lab on a Chip*, vol. 17, no. 19, pp. 3200–3220, Sep. 2017, doi: 10.1039/C7LC00587C.

[134] J. A. DuVall *et al.*, "A rotationally-driven polyethylene terephthalate microdevice with integrated reagent mixing for multiplexed PCR amplification of DNA," *Analytical Methods*, vol. 8, no. 40, pp. 7331–7340, Oct. 2016, doi: 10.1039/C6AY01984F.

[135] W. Zhang, S. Guo, W. S. Pereira Carvalho, Y. Jiang, and M. J. Serpe, "Portable point-of-care diagnostic devices," *Analytical Methods*, vol. 8, no. 44, pp. 7847–7867, Nov. 2016, doi: 10.1039/C6AY02158A.

[136] S. Byrnes *et al.*, "A Portable, Pressure Driven, Room Temperature Nucleic Acid Extraction and Storage System for Point of Care Molecular Diagnostics.," *Anal Methods*, vol. 5, no. 13, pp. 3177–3184, Jul. 2013, doi: 10.1039/C3AY40162F.

[137] J. R. Buser *et al.*, "A disposable chemical heater and dry enzyme preparation for lysis and extraction of DNA and RNA from microorganisms," *Analytical Methods*, vol. 8, no. 14, pp. 2880–2886, Mar. 2016, doi: 10.1039/C6AY00107F.

[138] T. Baier *et al.*, "Hands-free sample preparation platform for nucleic acid analysis," *Lab on a Chip*, vol. 9, no. 23, p. 3399, Dec. 2009, doi: 10.1039/b910421f.

[139] J. Siegrist *et al.*, "Validation of a centrifugal microfluidic sample lysis and homogenization platform for nucleic acid extraction with clinical samples.," *Lab Chip*, vol. 10, no. 3, pp. 363–71, Feb. 2010, doi: 10.1039/b913219h.

[140] Q. Ramadan and M. A. M. Gijs, "Simultaneous sample washing and concentration using a 'trapping-and-releasing' mechanism of magnetic beads on a microfluidic chip," *Analyst*, vol. 136, no. 6, p. 1157, Feb. 2011, doi: 10.1039/c0an00654h.

[141] R. S. Sista, A. E. Eckhardt, V. Srinivasan, M. G. Pollack, S. Palanki, and V. K. Pamula, "Heterogeneous immunoassays using magnetic beads on a digital microfluidic platform," *Lab on a Chip*, vol. 8, no. 12, pp. 2188–2196, 2008, doi: 10.1039/b807855f.

[142] I. Glocke and M. Meyer, "Extending the spectrum of DNA sequences retrieved from ancient bones and teeth.," *Genome Res*, vol. 27, no. 7, pp. 1230–1237, Jul. 2017, doi: 10.1101/gr.219675.116.

[143] F. Santos *et al.*, "Purification, concentration and recovery of small fragments of DNA from Giardia lamblia and their use for other molecular techniques.," *MethodsX*, vol. 4, pp. 289–296, 2017, doi: 10.1016/j.mex.2017.08.005.

[144] R. Zhang, K. Nakahira, X. Guo, A. M. K. Choi, and Z. Gu, "Very Short Mitochondrial DNA Fragments and Heteroplasmy in Human Plasma," *Scientific Reports*, vol. 6, no. 1, p. 36097, Dec. 2016, doi: 10.1038/srep36097.

[145] N. Witt *et al.*, "An assessment of air as a source of DNA contamination encountered when performing PCR," *Journal of Biomolecular Techniques*, vol. 20, no. 5, pp. 236–240, 2009.

[146] P. Yadava, M. Gibbs, C. Castro, and J. A. Hughes, "Effect of lyophilization and freeze-thawing on the stability of siRNA-liposome complexes.," *AAPS PharmSciTech*, vol. 9, no. 2, pp. 335–41, 2008, doi: 10.1208/s12249-007-9000-1.

[147] B. Guan *et al.*, "Sensitive extraction-free SARS-CoV-2 RNA virus detection using a chelating resin," *iScience*, vol. 24, no. 9, p. 102960, Sep. 2021, doi: 10.1016/j.isci.2021.102960.

[148] Y. Mardian, H. Kosasih, M. Karyana, A. Neal, and C.-Y. Lau, "Review of Current COVID-19 Diagnostics and Opportunities for Further Development," *Frontiers in Medicine*, vol. 8, p. 615099, May 2021, doi: 10.3389/fmed.2021.615099.

[149] O. Vandenberg, D. Martiny, O. Rochas, A. van Belkum, and Z. Kozlakidis, "Considerations for diagnostic COVID-19 tests," *Nature Reviews Microbiology*, vol. 19, no. 3, pp. 171–183, Mar. 2021, doi: 10.1038/s41579-020-00461-z.

[150] R. Weissleder, H. Lee, J. Ko, and M. J. Pittet, "COVID-19 diagnostics in context," *SCIENCE TRANSLATIONAL MEDICINE*, vol. 12, no. 546, p. eabc1931, 2020, doi: doi:10.1126/scitranslmed.abc1931.

[151] F. Watzinger, K. Ebner, and T. Lion, "Detection and monitoring of virus infections by real-time PCR," *Molecular Aspects of Medicine*, vol. 27, no. 2–3, pp. 254–298, Apr. 2006, doi: 10.1016/j.mam.2005.12.001.

[152] G. Mulberry, A. Vuillier, M. Vaidya, K. Sugaya, and B. Kim, "Handheld battery-operated sample preparation device for qPCR nucleic acid detections using simple contactless pouring," *Analytical Methods*, vol. 10, no. 38, 2018, doi: 10.1039/c8ay00998h.

[153] J. Kim, M. Johnson, P. Hill, and B. K. Gale, "Microfluidic sample preparation: cell lysis and nucleic acid purification," *Integrative Biology*, vol. 1, no. 10, p. 574, 2009, doi: 10.1039/b905844c.

[154] K. W. Hukari, M. Shultz, N. Isely, R. Milson, and J. A. A. West, "A Completely Automated Sample Preparation Instrument and Consumable Device for Isolation and Purification of Nucleic Acids," *JALA: Journal of the Association for Laboratory Automation*, vol. 16, no. 5, pp. 355–365, Oct. 2011, doi: 10.1016/j.jala.2010.08.004.

[155] S. Razavi Bazaz *et al.*, "3D Printing of Inertial Microfluidic Devices," *Scientific Reports*, vol. 10, no. 1, p. 5929, Dec. 2020, doi: 10.1038/s41598-020-62569-9.

[156] B. Gale *et al.*, "A Review of Current Methods in Microfluidic Device Fabrication and Future Commercialization Prospects," *Inventions*, vol. 3, no. 3, p. 60, Aug. 2018, doi: 10.3390/inventions3030060.

[157] T. Kajiyama *et al.*, "Genotyping on a thermal gradient DNA chip," *Genome Res*, vol. 13, no. 3, pp. 467–475, 2003, doi: 10.1101/gr.790603.

[158] W. Lee *et al.*, "3D-Printed Microfluidic Device for the Detection of Pathogenic Bacteria Using Size-based Separation in Helical Channel with Trapezoid Cross-Section," *Scientific Reports*, vol. 5, no. 1, p. 7717, Jul. 2015, doi: 10.1038/srep07717.

[159] A. K. Au, W. Huynh, L. F. Horowitz, and A. Folch, "3D-Printed Microfluidics," *Angewandte Chemie International Edition*, vol. 55, no. 12, pp. 3862–3881, Mar. 2016, doi: 10.1002/anie.201504382.

[160] Y. S. Lee, N. Bhattacharjee, and A. Folch, "3D-printed Quake-style microvalves and micropumps," *Lab Chip*, vol. 18, no. 8, pp. 1207–1214, 2018, doi: 10.1039/C8LC00001H.

[161] A. K. Au, W. Lee, and A. Folch, "Mail-order microfluidics: evaluation of stereolithography for the production of microfluidic devices," *Lab Chip*, vol. 14, no. 7, pp. 1294–1301, 2014, doi: 10.1039/c3lc51360b.

[162] I. L. Technologies, *PureLink™ Total RNA Blood Purification Kit Instruction Manual*. 2005.